Satellite observations of the plasma – neutral coupling near Mars and the Earth

Stanislav Barabash

IRF Scientific Report 228
December 1995

ISSN 0284-1703
ISBN 91-7191-124-3

INSTITUTET FÖR RYMDFYSIK
Swedish Institute of Space Physics

KIRUNA, Sweden

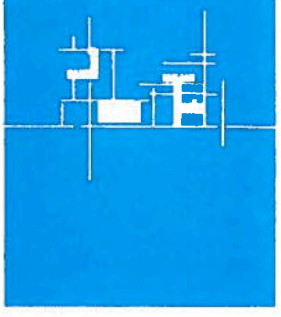

SATELLITE OBSERVATIONS OF THE PLASMA - NEUTRAL COUPLING NEAR MARS AND THE EARTH

Stanislav Barabash
Swedish Institute of Space Physics
P.O. Box 812, S-981 28 Kiruna, Sweden

Abstract

The dissertation deals with studies of the plasma - neutral interaction effects near Mars and the Earth and the development of instrumentation for energetic neutral atoms (ENAs) detection.

The ASPERA mass spectrometer, measuring electrons and ions in the energy range from several eV to tens keV, was launched to Mars on the Soviet / Russian Martian probe Phobos in 1988. The successful operation of the experiment in Martian orbits provided a unique data set characterizing the plasma around Mars. Analysis of these data revealed the important role of plasma - neutral coupling in the near planetary environment for the planet's interaction with the solar wind and evolution of the Martian atmosphere. The dissertation focuses on several related phenomena. These are: (1) exospheric pickup protons in the upstream solar wind, (2) back-streaming protons in the bow shock foreshock region, (3) nonthermal dissipation of helium from the Martian atmosphere, and (4) the solar wind / Martian plasma interactions with the Phobos gas / dust torus.

One of the most important manifestations of plasma - neutral coupling in space environments is the appearance of ENAs, a specific component generated in charge - exchange reactions. The ENAs can be used for remote observations of space plasmas and are of great importance for the state-of-art concept of global magnetospheric imaging. An entirely new type of instrumentation is needed to perform the ENA detection. The ENA instrument PIPPI (Prelude In Planetary Particle Imaging), covering the energy range 0.1 - 100 keV, has been designed, built and flown on the microsatellite Astrid in a 1000 km altitude polar orbit at the Earth in 1995. The following has been achieved in this first ever satellite-borne ENA experiment. (1) Unambiguous ENA images of ring current structures at low altitudes have been obtained. (2) The first observations of the ENA environment at low altitudes at mid-latitudes have been performed. (3) Several important components of ENA instrumentation have been developed and tested in flight. (4) A firm experience in the construction and calibration of ENA instruments has been gained. The PIPPI experiment marks the first step towards the much more sophisticated instrumentation needed to study ENAs, which are important not only in plasma imaging but in better understanding the dynamics of the plasma - neutral systems present in practically all space environments.

Keywords: planets, satellites, magnetosphere, atmosphere, exosphere, solar wind interaction, bow shock, ring current, dust, energetic atoms, remote sensing, instruments and techniques.

IRF Scientific Report 228
Swedish Institute of Space Physics
Kiruna 1995

ISSN 0284-1703
ISBN 91-7191-124-3
pp 77+ 8 papers

SATELLITE OBSERVATIONS OF THE PLASMA - NEUTRAL COUPLING NEAR MARS AND THE EARTH

Akademisk avhandling

som med tillstånd av rektorsämbetet vid Umeå universitet för avläggande av filosofie doktorsexamen framlägges till offentlig granskning vid Institutet för rymdfysik i Kiruna, konferensrummet Aniara, fredagen den 12 januari 1996, kl. 10.15

av

Stanislav Barabash
doktorand

The thesis includes an introductory part, description of the instrumentation development and the following papers:

I. Barabash, S., E. Dubinin, N. Pissarenko, R. Lundin, and C. Russell, Picked-up protons near Mars: PHOBOS observations, *Geophys. Res. Lett., 18,* 1805-1808, 1991.

II. Barabash, S., and R. Lundin, Reflected ions near Mars: PHOBOS-2 observations, *Geophys. Res. Lett., 20,* 787-790, 1993.

III. Barabash, S., R. Lundin, and O. Norberg, Upstream regions at Mars, in *Plasma environments of non-magnetized planets,* edited by T. I. Gombosi, pp. 285-290, Pergamon Press, Oxford, 1993.

IV. Barabash, S., and O. Norberg, Indirect detection of the Martian helium corona, *Geophys. Res. Lett., 21,* 1547-1550, 1994.

V. Barabash, S., E. Kallio, R. Lundin, and H. Koskinen, Measurements of nonthermal helium escape from Mars, *J. Geophys. Res., 100,* 21,307-21,316, 1995.

VI. Dubinin, E., R. Lundin, N. Pissarenko, S. Barabash, A. Zakharov, H. Koskinen, K. Schwingenschuh, and Ye. Yeroshenko, Indirect evidences for a gas/dust torus along the Phobos orbit, *Geophys. Res. Lett., 17,* 861 - 864, 1990.

VII. Barabash, S., and R. Lundin, On a possible dust-plasma interaction at Mars, *IEEE Trans. on plasma science, 22,* 173-178, 1994.

VIII. Barabash, S., R. Lundin, T. Zarnowiecki, and S. Gredzielski, Diagnostic of energetic neutral particles at Mars by the ASPERA-C instrument for the Mars 96 mission, *Adv. Space Res., 16,* (4)81-(4)86, 1995.

Kiruna 1996

Satellite observations of the plasma – neutral coupling near Mars and the Earth

by

Stanislav Barabash
Swedish Institute of Space Physics
P.O. Box 812, S-981 28 Kiruna, Sweden

IRF Scientific Report 228
December 1995

Printed in Sweden
Swedish Institute of Space Physics
Kiruna 1995
ISSN 0284-1703
ISBN 91-7191-124-3

Abstract

The dissertation deals with studies of the plasma - neutral interaction effects near Mars and the Earth and the development of instrumentation for energetic neutral atoms (ENAs) detection.

The ASPERA mass spectrometer, measuring electrons and ions in the energy range from several eV to tens keV, was launched to Mars on the Soviet / Russian Martian probe Phobos in 1988. The successful operation of the experiment in Martian orbits provided a unique data set characterizing the plasma around Mars. Analysis of these data revealed the important role of plasma - neutral coupling in the near planetary environment for the planet's interaction with the solar wind and evolution of the Martian atmosphere. The dissertation focuses on several related phenomena. These are: (1) exospheric pickup protons in the upstream solar wind, (2) back-streaming protons in the bow shock foreshock region, (3) nonthermal dissipation of helium from the Martian atmosphere, and (4) the solar wind / Martian plasma interactions with the Phobos gas / dust torus.

One of the most important manifestations of plasma - neutral coupling in space environments is the appearance of ENAs, a specific component generated in charge - exchange reactions. The ENAs can be used for remote observations of space plasmas and are of great importance for the state-of-art concept of global magnetospheric imaging. An entirely new type of instrumentation is needed to perform the ENA detection. The ENA instrument PIPPI (Prelude In Planetary Particle Imaging), covering the energy range 0.1 - 100 keV, has been designed, built and flown on the microsatellite Astrid in a 1000 km altitude polar orbit at the Earth in 1995. The following has been achieved in this first ever satellite-borne ENA experiment. (1) Unambiguous ENA images of ring current structures at low altitudes have been obtained. (2) The first observations of the ENA environment at low altitudes at mid-latitudes have been performed. (3) Several important components of ENA instrumentation have been developed and tested in flight. (4) A firm experience in the construction and calibration of ENA instruments has been gained. The PIPPI experiment marks the first step towards the much more sophisticated instrumentation needed to study ENAs, which are important not only in plasma imaging but in better understanding the dynamics of the plasma - neutral systems present in practically all space environments.

Keywords: planets, satellites, magnetosphere, atmosphere, exosphere, solar wind interaction, bow shock, ring current, dust, energetic atoms, remote sensing, instruments and techniques.

Contents

Introductory part

Development of the instrumentation

Included papers

I. Barabash, S., E. Dubinin, N. Pissarenko, R. Lundin, and C. Russell, Picked-up protons near Mars: PHOBOS observations, *Geophys. Res. Lett., 18*, 1805-1808, 1991.

II. Barabash, S., and R. Lundin, Reflected ions near Mars: PHOBOS-2 observations, *Geophys. Res. Lett., 20*, 787-790, 1993.

III. Barabash, S., R. Lundin, and O. Norberg, Upstream regions at Mars, in *Plasma environments of non-magnetized planets*, edited by T. I. Gombosi, pp. 285-290, Pergamon Press, Oxford, 1993.

IV. Barabash, S., and O. Norberg, Indirect detection of the Martian helium corona, *Geophys. Res. Lett., 21*, 1547-1550, 1994.

V. Barabash, S., E. Kallio, R. Lundin, and H. Koskinen, Measurements of nonthermal helium escape from Mars, *J. Geophys. Res., 100*, 21,307-21,316, 1995.

VI. Dubinin, E., R. Lundin, N. Pissarenko, S. Barabash, A. Zakharov, H. Koskinen, K. Schwingenschuh, and Ye. Yeroshenko, Indirect evidences for a gas/dust torus along the Phobos orbit, *Geophys. Res. Lett., 17*, 861 - 864, 1990.

VII. Barabash, S., and R. Lundin, On a possible dust-plasma interaction at Mars, *IEEE Trans. on plasma science, 22*, 173-178, 1994.

VIII. Barabash, S., R. Lundin, T. Zarnowiecki, and S. Gredzielski, Diagnostic of energetic neutral particles at Mars by the ASPERA-C instrument for the Mars 96 mission, *Adv. Space Res., 16*, (4)81-(4)86, 1995.

Science flourishes best when it uses freely all the tools at hand,
unconstrained by preconceived notions of what science
ought to be. Every time we introduce a new tool,
it always leads to new and unexpected discoveries,
because Nature's imagination is richer than ours.

Freeman Dyson, The scientist as rebel

But the manuscript is short and is intimately connected with the affair.

Sir Arthur Conan Doyle, The hound of Baskervilles

Plasma - Neutral coupling in Near Planetary Space

All the bodies within the Solar system, the planets, satellites, asteroids, comets and dust particles are immersed in a supersonic flow of very rare, mainly proton, plasma - the solar wind. These bodies constitute a disturbance of the plasma flow, i.e., they interact with the solar wind plasma. In some cases the disturbances can be quite significant and occupy tremendous volumes. If we restrict ourselves by considering bodies with typical interaction region sizes larger than the solar wind proton gyro-radius, we can identify three basic types of interaction: interaction with magnetized bodies, interaction with unmagnetized bodies having an atmosphere, and interaction with unmagnetized bodies with no atmosphere.

The magnetic field of a magnetized body provides an effective obstacle to the solar-wind plasma. The solar-wind dynamic pressure acts on the outer reaches of the magnetic field, confining it to a magnetospheric cavity which is not, of course, empty of matter, but is filled by a mixture of the solar-wind plasma and charged and neutral particles originating from the body itself. The pressure of the magnetic field and the plasma establishes an equilibrium with the solar wind. This type of interaction is found, for example, at Mercury, the Earth, Jupiter, Saturn, Uranus and Neptune.

A celestial object with an atmosphere also possesses an ionosphere. Because the ionosphere is a conductor, the convecting electric field generates currents whose magnetic field cancels the solar-wind field and prevents it from penetrating through the body. This basic picture is appropriate for the solar-wind interaction with the planets Venus and Mars, and perhaps for Saturn's satellite Titan when it is outside the Saturnian magnetosphere.

A body which possesses neither an intrinsic magnetic field nor an atmosphere simply absorbs the particles of the solar-wind plasma that are incident on the body. The most notable feature associated with this type of interaction is the plasma-absorption wake in the plasma behind the body. The Moon is an example where such an interaction takes place.

In this dissertation we deal, mainly, with bodies possessing an atmosphere and, hence, exosphere. An exosphere may be defined as a part of the upper atmosphere above the level (the exobase) at which the mean free path equals the scale height. Thus collisions do not play a role in the redistribution of energy between the particles within the exosphere. In the exosphere, particles (molecules and atoms) move on ballistic trajectories and can escape the central body. This is why the exosphere is sometimes defined as that part of the upper atmosphere where thermal escape prevails. The exospheres extend to very large distances. For example, for the Earth the hydrogen exospheric density is still 10 cm^{-3} even at 12 earth radii. For each type of solar-wind interaction, the huge volume surrounding the central body is never empty of plasma. If a magnetosphere is formed, it is filled by hot and energetic plasma trapped in the central body's magnetic field. If the Venus type of interaction takes place, this volume is occupied by solar wind plasma. In any case, one can see that there are two different types of matter, plasma and neutrals, coexisting. Apparently, an interaction between them must take place. For the altitudes in question, ion - neutral friction is negligible in the dynamics of both the plasma and the gas, and collisionless interaction is of interest.

There are two basic collisionless mechanisms which can couple the plasma and neutral components. The first is related to ionisation of the neutral component via photoionisation (and / or electron impact ionisation), which takes place almost always in space. The new-born ions usually have different characteristics (mass, distribution function) in comparison with the primary plasma and the interaction occurs between these two ion components. If, for instance, there is a frozen-in magnetic field in the primary plasma, it bounds two populations resulting in changes of the dynamic characteristics of both. Such a type of coupling is of great importance for the solar-wind interaction with nonmagnetized planets and comets.

The second mechanism is related to the fundamental interaction between neutrals (atoms or molecules) and ions, the charge - exchange (CE) process. In this process an ion takes an

electron from a neutral and is turned into a neutral particle while the neutral becomes a charged particle. In this process the primary velocities of the ion and neutral are conserved. If the exchange occurs between the neutral, M, and the ion, M^+, the process is termed resonant CE and has a very large cross section because the electron exchange can take place over large distances between particles. New-born neutrals have the energy of the plasma particles but they are not affected by electromagnetic fields and are decoupled from the primary plasma. They can, thus, leave the interaction region and carry away momentum. Figure 1 gives the CE cross sections for the most important ion and neutral species.

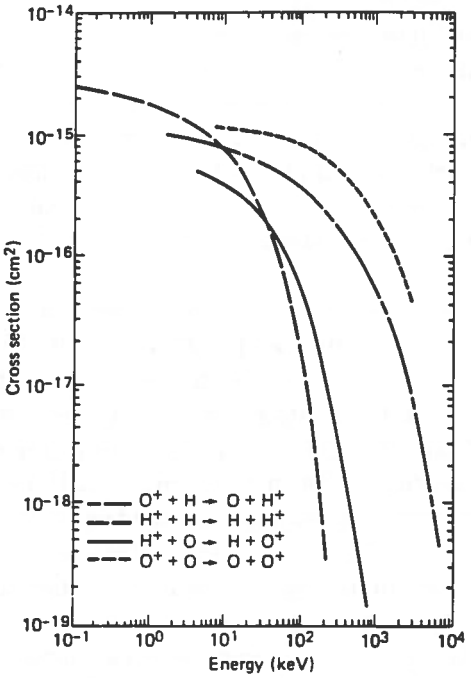

Figure 1. *Charge - exchange cross section as a function of total ion energy for electron exchange by singly-charged energetic ions (H^+ and O^+) with cold hydrogen or oxygen (from McEntire and Mitchell, 1989).*

The significance of the CE process in space physics has been appreciated for a long time, back to the work by *Dessler and Parker* [1959]. They considered the lifetime of trapped particles in the Earth's magnetosphere against the CE loss in the reaction with the terrestrial exosphere. Recently, this type of plasma - neutral coupling has drawn attention to the aspect of the fast neutrals born in this process, because the latter can be used to investigate remotely both components (plasma and neutrals) involved in the interaction.

There are several other processes of plasma - neutral coupling which do not play a significant role for the conditions of interest here. If a plasma moves through a sufficient dense neutral gas with a velocity corresponding to a kinetic energy greater than the neutral gas ionisation energy, the interaction becomes very strong and leads to a quick ionization of the neutral gas. This is the well known critical ionisation velocity effect which will not be considered in this dissertation. Neither will we discuss inelastic ion - neutral collisional excitation and ionisation.

The dissertation is organised by the following way. In the section *The Plasma - Neutral Particles Interaction Effects at Mars* a short description of the Martian neutral environment is followed by a review of processes taking place in plasma flowing through the exosphere and manifested in the solar-wind interaction with this planet. The detailed studies of certain

aspects, namely, pickup protons from the hydrogen exosphere, back-streaming protons in the upstream region and their role in the solar wind deceleration, are presented in Papers I, II, III. Not only the plasma flow is affected in the interaction process, but the neutral component is modified as well. Taking again Mars as an example, we consider the erosion of its neutral environment due to the solar-wind interaction. The extended discussion and measurements of the escape rate for one particular component, helium, are given in Papers IV and V. Finally, we review a possible interaction between the solar wind and a torus of gas / dust debris along the Phobos orbits. More detailed consideration is given in Papers VI and VII.

Having reviewed the dynamic processes caused by the plasma - neutral coupling in the Martian environment, we then consider one particular type of coupling, charge - exchange, which results in the formation of energetic neutral atoms (ENAs). In the section *ENAs as a Specific Component* we consider ENAs from a more general point of view than is usually done. Having briefly examined the ENA generation in different plasmas within the Solar system, we discuss the properties of ENAs generated in the terrestrial magnetosphere and in the Martian plasma environment. Since Paper VIII deals with the latter in detail, we only emphasise the most important aspects.

Having introduced ENAs as a specific component, in the section *Measurement Techniques* we discuss how one can detect this component. Generally speaking, measurements of both ENAs and plasma are important and we illustrate concisely the plasma instrumentation describing the ASPERA mass spectrometer on the Phobos mission from which the data were used in the "Martian" section. Then we consider thoroughly the neutral particle experiment PIPPI (Prelude In Planetary Particle Imaging) designed for the Mars 96 mission to be launched in 1996 and flown on the microsatellite Astrid in 1995. A review of the results from the Astrid mission, the first spacecraft equipped with a dedicated instrument to measure ENAs, concludes the section.

The section *Summary and Future Prospects* provides a brief description of the principal results, states what has been achieved by this work, and discusses further related studies and experiments.

The Plasma - Neutral Interaction Effects at Mars

Because of the very weak or non-existent intrinsic planetary magnetic field, the solar wind interaction with Mars is characterized by direct streaming of the solar wind plasma flow through the Martian exosphere. Furthermore, as a result of the low gravity at Mars, the neutral density can reach 10^4 - 10^6 cm^{-3} in the interaction region where the main boundaries, the bow shock and the magnetopause, are located and the most interesting (for plasma physics) processes take place. This results in a number of unusual effects which seem to be unique in the Solar system. From this point of view Mars may be considered as a natural laboratory to study plasma - neutral interaction phenomena. In the regions under consideration the plasma and the neutrals are collisionless and interaction occurs between the solar wind plasma and exospheric ions resulting from ionisation of the neutral component through photoionization, CE process and electron impact ionization. Both light (protons) and heavy (He^+, O^+) new-born ions lead to a number of dynamic effects observed in the solar wind flow. On the other hand, the ions are being lost from the exosphere and the neutral environment itself undergoes modification in this interaction process.

We restrict our consideration to the regions outside the obstacle and will not discuss the nature of the latter, because, firstly, it is out of the area of this study and, secondly, there is still no established opinion concerning this matter. To identify a boundary separating the solar wind proton plasma and the planetary plasma (magnetic field) we use the term magnetopause, mainly because of historical reasons rather than due to its physical character. For the time being the terminology has not yet settled down and different experimental / theoretical groups use different terms such as chemical composition boundary [*Breus et al.*, 1991], planetopause [*Riedler et al.*, 1989] and protonopause [*Sauer et al.*, 1995] to identify a boundary where the solar wind proton density drops significantly. Above the magnetopause the solar wind plasma is mixed with ions of planetary origin resulting from ionization of the exospheric neutrals and differing significantly from the pure magnetosheath plasma. Within such a "mantle" the flow is still directed as in the magnetosheath, but the flow velocity is lower since the plasma has a higher mass density that the solar wind proton plasma [*Vaisberg et al.*, 1990]. One can say that the inner magnetosheath is "mass-loaded". To emphasise this change in the flow characteristics *Lundin et al.* [1990] introduced a mass-loading boundary. While in the tail region both these boundaries can be distinguished, near the subsolar point they seem to be merged. All the main Martian boundaries are presented schematically in Figure 2. Since it is the Phobos spacecraft which has provided us with the most comprehensive data on plasma at Mars, we have sketched its circular and elliptic orbits in Figure 2 as well.

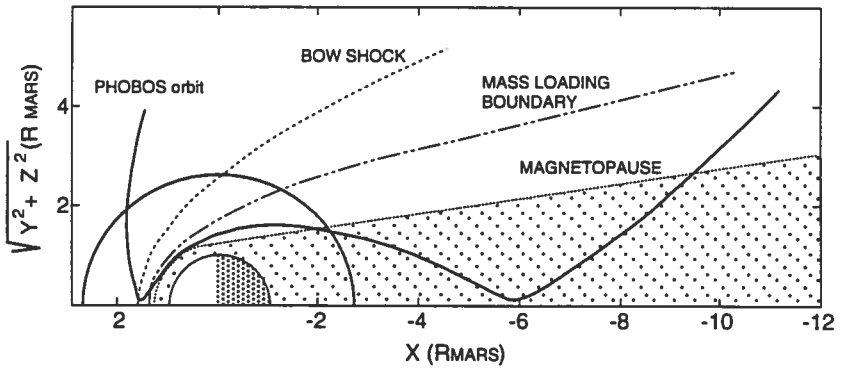

Figure 2. *The main boundaries of the Martian magnetosphere and the Phobos spacecraft orbits.*

The Martian Neutral Environment

Since Mars does not seem to have a significant magnetic field, the region of the interaction with the solar wind is rather compact in comparison with, for example, the terrestrial magnetosphere. Thus several gases with the largest scale heights such as hydrogen, molecular hydrogen, helium, and oxygen appear to play a role in the interaction. For all these gases the exobase is located at altitudes less than 300 km, i.e., within the magnetopause. The density profile above the exobase is given by the Chamberlain formula [*Chamberlain*, 1963]

$$N(h) = n_c \exp\left(H\cdot\left(\frac{1}{R_m + h} - \frac{1}{R_m + h_c}\right)\right)\cdot\zeta\left(\frac{H}{R_m + h}\right) \qquad (1)$$

where n_c is the neutral density at the exobase for a given gas, h_c the exobase altitude, R_m the Martian radius, h the altitude, ζ is the partition function for high altitudes and H is the characteristic scale height, $H = GmM_m/kT$ where G is the gravitational constant, m the atomic mass, M_m the mass of Mars, k the Boltzmann constant and T the temperature at the exobase. The exospheric density for hydrogen is given in Figure 3. The curves 1 and 2 correspond to the Lyman α measurements onboard Mariner 6, 7 [*Anderson*, 1974; *Anderson and Hord*, 1971] and Mars 2,3 [*Dostovalov and Chuvahin*, 1973]. Profile 3 was obtained from measurements of the pickup protons with the ASPERA mass spectrometer onboard the Phobos spacecraft [*Barabash et al.*, 1991].

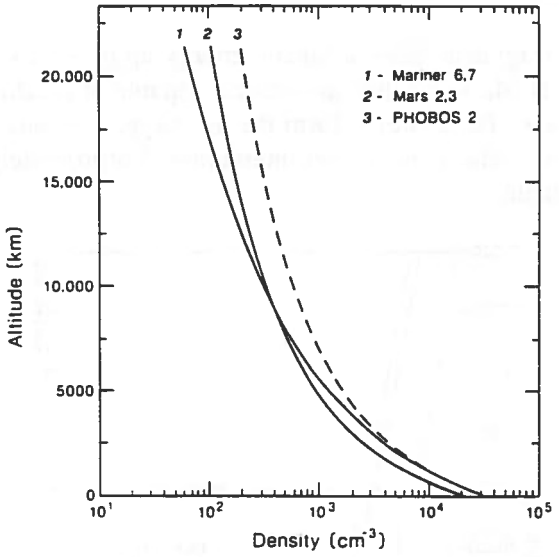

Figure 3. *The exospheric density for hydrogen at Mars. The curves 1 and 2 correspond to the Lyman α measurements onboard Mariner 6, 7 [Anderson, 1974; Anderson and Hord, 1971] and Mars 2,3 [Dostovalov and Chuvahin, 1973]. Profile 3 was obtained from measurements of the pickup protons with the ASPERA mass spectrometer onboard the Phobos spacecraft [Barabash et al., 1991].*

The densities of H, H_2, He and cold O for altitudes up to 1000 km are shown in Figure 4. Up to 450 km the profiles are given by the *Moroz et al.* [1991] atmospheric model and higher up are extrapolated according to Formula 1.

The existence of the hot oxygen corona is one of the most interesting and important features of the Martian neutral environment. The basic process of the corona formation is simple. The major ionospheric ion O_2^+ can undergo electron dissociative recombination

$$O_2^+ + e \rightarrow O^* + O^*$$

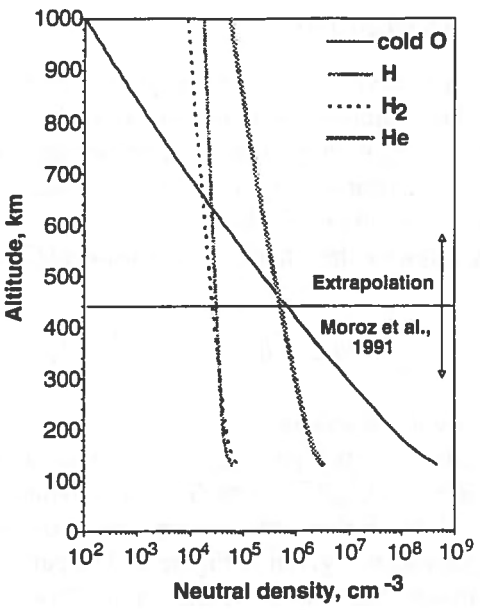

Figure 4. *The Martian neutral atmosphere during solar maximum according to the model by Moroz et al. [1991] for altitudes below 450 km and calculated on the basis of the Chamberlain formula profile for higher altitudes.*

The created atomic O^* fragments carry a kinetic energy up to 3.5 eV higher than the escape velocity for the oxygen at Mars and they are, hence, capable of reaching very large distances from the planetary surface. These atoms form the hot oxygen corona of Mars which plays a very important role in the solar-wind planet interaction. Unfortunately, no measurements of this component are available.

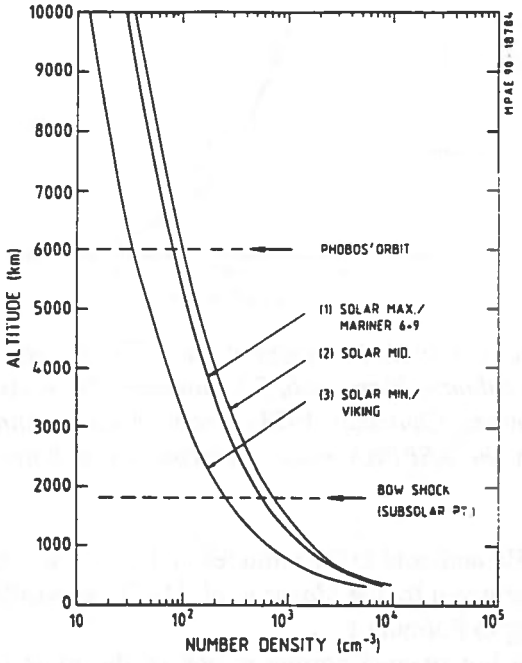

Figure 5. *The number density profiles of the hot oxygen for three different solar conditions (from Ip, 1990). The solar maximum corresponds to the time period of the Phobos measurements.*

Furthermore, modelling is very sensitive to the input parameters and different models predict significantly different hot oxygen densities. The profiles shown in Figure 5 are given by the model of *Ip* [1990] for the different solar conditions. The solar maximum corresponds to the time period of the Phobos measurements.

The Solar Wind - Exosphere Interactions

Hydrogen has the largest scale height and its corona extends well beyond the bow shock with a typical subsolar point of 1400 km (see Figures 3). Even at an altitude of 20,000 km the hydrogen density is 10^2 cm^{-3}. The atoms are ionized by the solar UV photons or via the CE process or electron impact ionisation, and picked up by the solar wind. In general, such ions experience an effective accelerating electric field equal to - $(\underline{V} \times \underline{B})/c$, where $\underline{V}$ is the ambient plasma velocity, $\underline{B}$ the magnetic field vector and c the speed of light. Another way of putting this is that once a neutral atom is ionized, it begins to gyrate around the magnetic field that is moving by with the solar plasma. This gyration, with translation at the plasma velocity on average, causes the ion velocity to cycle between zero and twice the plasma speed. The resulting cycloid trajectories are a consequence of this response to the moving magnetic field. The energy of the pickup protons in the rest frame of reference (a spacecraft) is $\leq 4\, E_{sw} \sin^2\alpha$, where E_{sw} is the solar wind proton energy and α is the angle between the plasma velocity and the magnetic field direction. Under the maximum condition $\alpha = 90°$, the pickup proton energy is 4 times higher than the solar wind proton energy. If the solar wind temperature is low enough, pickup protons appear themselves as a small secondary peak on the energy spectra. Such observations have been made for the Martian hydrogen corona [*Barabash et al.*, 1991; *Barabash et al.*, 1993] and the Halley comet hydrogen environment [*Neugebauer et al.*, 1989]. The injection of the new-born protons into the solar wind flow does not change significantly its velocity, because the mass added is negligible. For example, under the Martian conditions the pickup proton density is only 0.5% of the solar wind density. That causes a drop in the solar wind velocity of less than 2 km/s [*Barabash et al.*, 1993].

The new-born ions form a beam along the magnetic field in the solar wind frame of reference, simultaneously taking part in the cyclotron motion. Cyclotron instability of the beam generates Alfven waves with a frequency close to the proton gyro-frequency in the spacecraft frame of reference [*Wu and Davidson*, 1972]. Such waves have been, indeed, detected at distances of 7000 - 10,000 km above the Mars surface [*Russell et al.*, 1990]. These waves cause pitch-angle diffusion of the new-born protons but due to lack of space for development of the cyclotron instability (the hydrogen scale height is not large enough), the angular broadening of the beam does not exceed 20° - 30°. This value can be determined from the power spectrum of the fluctuating magnetic field [*Russell et al.*, 1990] and is in agreement with estimates of the distribution function shape [*Barabash et al.*, 1991]. For comets, in contrast, these waves have ample opportunity to grow to larger amplitude due to the huge scales height involved. The magnetic field fluctuations related to these waves have actually been detected in the upstream regions of the comets Halley and Giacobini-Zinner [*Scarf et al.*, 1986; *Tsurutani and Smith*, 1986].

The pickup protons cannot modify the solar wind flow strongly in a direct way because of the low mass added. However, by including into consideration the effects related to the interaction of these ions with the Martian bow shock, the situation may change drastically. As pointed out, due to the lack of space the new-born protons do not have time to become fully integrated in the solar wind flow. Even pitch-angle diffusion, which is comparatively fast, not to mention the energy diffusion, are quite weakly manifested. Hence the pickup protons born far upstream arrive at the bow shock with energy varying between 0 to ~$4E_{sw}$. A fraction of these ions cannot pass through the bow shock potential and is reflected back to the solar wind. If this occurs in the quasi-perpendicular region, the ions come back to the shock after a Larmour circle and are reflected again; meanwhile, they are moving towards the quasi-parallel

region where the reflection causes the ions to move away from the shock. Furthermore, due to higher exospheric density, the amount of protons born at lower altitudes just above the bow shock is much more than that of protons born in the far upstream region. The beams of these ions generated in the quasi-parallel part of the shock propagate well upstream, increasing the local pickup density there. Thus the pickup ions become redistributed in the space around Mars and occupy, mainly, the ion foreshock region where their density can be already significant enough to affect the solar wind flow. This idea was first proposed by *Ip* [1992] and an anomalously high density of the back-scattered protons has been, indeed, observed in the Martian foreshock region with the ASPERA instrument on the Phobos spacecraft [*Barabash and Lundin,* 1993; *Barabash et al.,* 1993]. The measured density was 30% of that of the solar wind and this population should result in an already notable deceleration of the solar wind (~60 km/s). *Dubinin et al.* [1994] have performed a test particle simulation of this effect and came to a reasonable agreement between the predicted and measured increase in the local proton density along the Phobos orbit. We should, however, note that the Martian bow shock is a complicated structure, not well understood yet, and unusually high densities of the back-streaming particles may, in principle, be related to some kinetic effects rather than pickup process. For instance, the size of the Martian magnetosheath is comparable with the proton gyro-radius and the particles do not have enough room to get thermalized there. Thus they can be reflected not at the bow shock but at the magnetic barrier at the obstacle boundary and still reach the space outside the bow shock [*Brecht and Ferrante,* 1991]. Effects induced by the finite shock surface curvature may also result in increase of the ion density in the ion foreshock region [*Moses et al.,* 1988].

The hot oxygen corona does not play a significant role in the global solar wind deceleration in the upstream region. The basic reason for this is the large gyro-radius of the O^+ ions. This is 5000 km, i.e., about twice the size of the planet, and pickup oxygen all the more does not have room to be assimilated into the solar wind. But even in the case of the integration occurring immediately after the ion creation, the deceleration of the solar wind has been estimated to be less than 5 - 10 km/s [*Ip,* 1988a]. However, the observed decrement of the solar wind velocity in the upstream region was 100 km/s [*Verigin et al.,* 1991a]. To explain the entire drop with only an oxygen corona would require increasing its density by a factor of 10 even for the "maximum" theoretical prediction by *Ip* [1990] (Figure 5).

Besides the kinetic effects discussed above, the Martian bow shock has another unusual feature. Due to extended neutral coronae, the densities of hydrogen, helium, and oxygen are quite high at the bow shock region at an altitude of about 1400 - 1600 km, and range up to 10^4 cm^{-3}, 5×10^3 cm^{-3}, 6×10^2 cm^{-3} respectively [*Moroz et al.,* 1991; *Barabash et al.,* 1995b; *Ip,* 1990]. Hot electrons, which are always present within the bow shock front, may cause ionization of the neutral components, resulting in the creation of a low energy (< 10 eV) ion component near the bow shock. Such a mechanism has been invoked by *Dubinin et al.* [1993] to explain the ASPERA observations of cold protons within the bow shock front. Even some speculations have been made to support the idea that the ionisation has a self-sustained character. Keeping in mind the very complicated structure of the Martian bow shock, this suggestion looks rather controversial but it raises a very interesting and not yet addressed problem of collisionless shocks in plasma with a gas background.

In the magnetosheath region the neutral density is high and generation of the new ions so intense, that the solar wind flow becomes strongly affected. Both of the two basic processes of the plasma - neutral coupling take place: mass loading of the solar wind and the CE process. The thermal oxygen atoms play a major role for both processes, because of the highest neutral density.

Near the subsolar magnetopause the stream tubes of the solar wind move at the lowest altitudes of 350 - 400 km, just where the CE loss is very effective due to high neutral density and in a boundary layer overlying the obstacle the solar wind protons become highly depleted.

Since the neutral density drops exponentially, the CE process at Mars is an extremely localized phenomenon [*Ip*, 1992]. Numerical calculations show that the solar wind proton density decreases to zero over the altitudes from 800 km to 700 km at the zenith angle 40° [*Ip et al.*, 1993]. In other words, the CE process "eats" out the entire solar wind flux over a distance of only 100 km! The similar effect at Halley's comet takes 10^4 km because the cometary neutrals are freely extended rather than being gravitationally bound, as in the Martian exosphere. The depletion layer is a very intense source of fast neutrals and is of major interest for the ENA imaging which will be discussed in the "ENA" part of dissertation. We should note, however, that the purely hydrodynamic (magneto hydrodynamic) description as used above is, perhaps, too simplified, because typical Larmour radii are of the order of the magnetosheath size. Either hybrid [*Brecht and Ferrante,* 1991] or test particle simulations [*Luhmann and Schwingenschuh,* 1990] are needed for better understanding and interpretation of available data.

Summing up, the collisionless interaction between the solar wind plasma and new-born (in the Martian exosphere) ions results in the following effects. Ionisation of hydrogen from the extended exosphere causes injection of the new-born protons into the solar wind. The pickup protons cause the generation of Alfven waves in the upstream region. Being reflected from the Martian bow shock, they may result in a significant increase of the density of back-streaming ions in the foreshock region leading to the effective solar wind deceleration. However, the kinetic effects related to the complicated structure of the Martian bow shock should contribute to the generation of the back-streaming fluxes of particles as well. Ionisation of the exospheric gases within the bow shock front might take place too. The solar wind flowing through the Martian exosphere gets mass-loaded and significantly decelerated. At even lower altitudes the solar wind seems to be terminated due to the CE process.

Erosion of the Martian Neutral Environment

In the preceding section we considered effects caused by new-born ions from the Martian neutral environment in the flowing solar wind. However, the interaction process affects not only the plasma but modifies the neutral environment as well. Unlike the Earth, Mars does not seem to have a significant intrinsic magnetic field to shield the neutral environment from the direct incidence of the solar wind and plasma comes into direct contact with the upper atmosphere / exosphere. Apparently it leads to a modification of the latter. One of the most notable manifestations of the solar wind interaction is the loss of the planetary ions / neutrals; we call this modification an erosion. Basically, four processes are of interest; (1) the ionospheric plasma escape which represents a significant path of ionospheric loss, (2) the pickup process of the exospheric ions by the solar wind, which drastically exceeds the Jeans dissipation, (3) the precipitation of the pickup heavy planetary ions like O^+ which can re-enter the upper atmosphere and deposit significant energy there, (4) delivery of matter from the solar wind to the Martian atmosphere.

According to a morphological classification based on direct measurements with the Phobos spacecraft plasma package, three general populations of planetary outflowing ions are identified [*Lundin et al,* 1993]. One is connected with intense keV ion beams observed in the central tail / plasma sheet region, another is associated with more slowly drifting cold (< 100 eV) plasma dominating in the flanks near the Martian magnetopause, and the third population consists of pickup ions that can be found outside the magnetosphere. Figure 6 depicts the general view of ion acceleration at Mars. The first and second populations seem to be related to the process (1) above, and the third one with (2). However, in terms of the integral loss rate, it is not important to distinguish between the different populations (or processes) and the term total outflow covering all escape mechanisms is appropriate. The importance of the plasma outflow for the entire ionosphere / atmosphere / exosphere system is characterized by the total amount of matter leaving the planet per second.

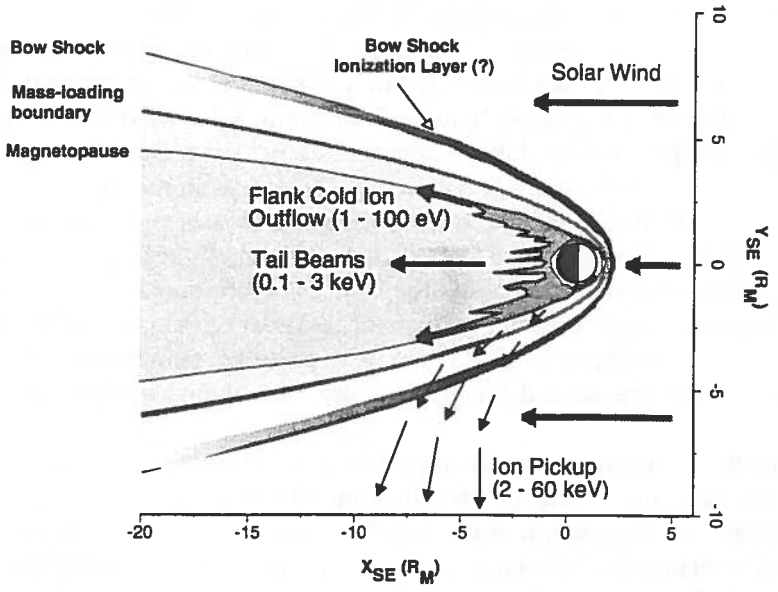

Figure 6. *General view of ion acceleration at Mars (from Lundin et al, 1993).*

Accurate measurements of the total outflow are not straightforward because they are strongly affected by the geometrical coverage of the magnetosphere and by the energy coverage of the plasma distribution function. To date, the total outflow has been directly measured only for the two Martian ions O^+ and He^+ [*Lundin et al.*, 1989a; *Barabash et al.*, 1995b]. There have also been some indirect measurements with instruments with no mass separation on the Mars 5 and Phobos missions [*Vaisberg et al.*, 1976, *Rosenbauer et al.*, 1989; *Verigin et al.*, 1991b].

Lundin et al. [1989a], using the ASPERA mass spectrometer data, estimated that the total outflow of less than 10-keV oxygen ions (process (1)) is 2×10^{25} ions/s, i.e., 0.5 kg/s. *Rosenbauer et al.* [1989], with the use of the TAUS energy spectrometer data, came to a similar number. However, *Verigin et al.* [1991b], using a more extended data set from the same instrument, obtained 5×10^{24} ions/s, i.e., 0.15 kg/s. The difference between the ASPERA and TAUS results could be related to different energy coverage. *Lundin et al.* [1989a] also pointed out that the observed molecular-ion escape such as O_2^+ and CO_2^+ increases the total oxygen escape up to 1 kg/s. At this loss rate all of the present oxygen content of the Martian atmosphere (chemically bound in CO_2) would be gone within the next 10^8 years. According to *Lundin et al.* [1989a], if this rate has prevailed over the 4.5×10^9 year age of the solar system, the amount of oxygen which has escaped could have supplied that needed for ~1 m of surface water. More detailed studies [*Perez-de-Tejada*, 1992], taking into account the variability of the ionosphere through the planetary history, gives a much higher (~30 m) equivalent depth for water which has escaped due to the solar wind interaction process.

The current atmospheric conditions on Mars indicate that water does not exist on the surface in any significant amount (an equivalent water layer is 15 μm deep [*Farmer et al.*, 1977]). On the other hand, water associated with active volcanism existed in the past on the Martian surface. The total volume of volcanic material that has been identified on the surface corresponds to the amount of water released with this material being equivalent to a 50 - 80 m surface layer. Thus we come to a problem of the Mars dehydration. Where is the Martian water? Is it gone or frozen and buried? If the former, what could produce such an effective escape mechanism? If the latter, where is this tremendous amount of water stored? As indicated above, the processes associated with the solar-wind interaction could account for the escape of at least half the amount of water delivered to the Martian atmosphere through early volcanic activity.

Experimental estimations of oxygen outflow through process (2) have not been performed yet, because it is very difficult to distinguish between ions newly-born in the exosphere and picked up by the solar wind, and ions extracted from the ionosphere and then accelerated by some mechanism which is not yet known. However, numerical estimations give 6×10^{24} ions/s for the pickup ions escape flux [*Zhang et al.*, 1993]. Though the process of Martian oxygen outflow due to the solar wind interaction is important for the evolution of the planetary atmosphere, it is not a major sink. The dissociative recombination of the principal ionospheric ion O_2^+ in the vicinity of the exobase (200 - 300 km altitude) leads to the formation of the hot oxygen corona and provides a total outflow of $(5 - 8)\times10^{25}$ ions/s [*Verigin et al.*, 1991b; *Zhang et al.*, 1993].

Besides oxygen, He^+ ions have been detected near Mars [*Barabash and Norberg*, 1994]. A significant difference between the measured particle velocity and the solar wind velocity suggests that these ions are of planetary origin. The particles have typical energies of either more than 10 keV or about 500 eV. The former correspond to the ions picked up in the solar wind (process 2) and the latter might be ions extracted from the ionosphere (process 1). The total outflow of helium was estimated to be 1.2×10^{24} ions/s [*Barabash et al.*, 1995b]. Measurements of the helium outflow are important for providing very valuable planetological information about geological processes in the interior of Mars and, in general, for all terrestrial planets, because the only source of He in the atmospheres of the planets is the radioactive decay of isotopes of uranium and thorium. These reactions, together with the production of argon from ^{40}K, are the main contributors to the radioactive heating of the planetary interior. If we assume that under the present conditions the helium escape is balanced by its outgassing from the planet surface to the atmosphere, and take a reasonable guess for the outgassing coefficients, we can estimate the absolute abundance of uranium and thorium. The total helium outflow is thus an important input parameter for all models dealing with the global planetary heat balance. Helium escapes from the atmospheres predominantly via a nonthermal process, mainly as He^+ ions, because the Jeans dissipation is negligible. A most puzzling aspect is that the measured total outflow [*Barabash et al.*, 1995] exceeds the predicted one [*Krasnopolsky et al.*, 1994] by a factor of 19! Should either the modern abundance of U and Th or the models of atmospheric evolution be reconsidered? Or it is only a temporal effect due to the observations being during different solar conditions? More advanced studies and measurements are needed to solve this problem.

The pickup process of the ions newly-born in the exosphere and scavenging of the ionospheric ions are not the only processes of the planetary atmosphere loss related to the solar-wind interaction. *Luhmann and Kozyra* [1991] pointed out that due to a large gyro-radius comparable with the Martian magnetosphere size, the pickup ions can re-enter the upper atmosphere and deposit a significant energy there. This causes back-scattering or sputtering of the primary neutral population, providing a contribution to the oxygen exosphere and oxygen escape. This neutral "wind" represents a possibly significant loss of the atmospheric constituents over the age of the solar system [*Luhmann et al.*, 1992]. It is interesting to note that a similar effect is expected at mid-latitudes and low (< 800 km) altitudes in the terrestrial magnetosphere, but the precipitating ions are auroral particles. It is called there ENA albedo and will be discussed in the ENA section of the dissertation.

The solar wind can cause not only erosion of the neutral environment but it also deposits matter in the Martian atmosphere as well. To explain the significant difference between the observed escape and predicted production rate of helium, *Barabash et al.* [1995b] suggested that the helium may be delivered to the Martian atmosphere as the solar wind α particles. Indeed, the hybrid simulation of the solar wind - Mars interaction has recently revealed that the solar wind ions can reach the Martian ionosphere due to their large gyro-radius in comparison with the interaction region (S. Brecht, private communication, 1994). Depending on the interplanetary magnetic field conditions, the fraction of ions impinging on the ionosphere

varies from 10% to 90 %. Taking the 50% deposition we obtain the He delivery 3 times higher than the estimated internal production. For comparison, we note that the estimated supply of helium into the Mercury atmosphere from the solar wind is 5 - 30 times higher than the radiogenic production rate [*Goldstein et al.*, 1981]. This illustrates how important the solar wind may be for the evolution of certain atmospheric components.

Plasma Effects of the Phobos Gas / Dust Torus

Not only are the largest bodies of the Solar system, the planets, as well as comets, characterized by the presence of a neutral environment, but many planetary satellites have well-developed atmospheres and, hence, exospheres as well. Obvious examples are the large Jovian and Saturnian satellites. Moreover, even some of the smallest and the most "lifeless" bodies of the Solar system, the asteroids, demonstrate signatures of outgassing (see review by *Herbert* [1993]). A coupling between the solar wind and neutrals escaping these bodies may result in weak, but still detectable, plasma effects.

Two Martian satellites are believed to be captured asteroids, although the hypothesis of local accretion is not yet ruled out. In any case, Phobos and Deimos belong to the smallest among planetary satellites. Their shapes can be approximated roughly by ellipsoids 27×22×19km and 15×12×11km, respectively. Phobos moves around Mars at $2.7R_m$, and Deimos at $6.9R_m$. Both moons orbit in the planet's equatorial plane. Phobos is so close to Mars that its orbital period (7 hours and 39 minutes) is less than one-third of a Martian day. The Phobos orbit is shrinking and it is spiralling towards destruction due to strong tidal force. According to some estimates, Phobos will fall onto Mars within 30 - 70 million years. In fact, Phobos is located within its Roche limit, i.e., the tidal forces are stronger than the moon gravitation, and thus the satellite undergoes constant disruption. The very low albedos of Phobos and Deimos, 0.06 and 0.07 respectively, indicate that the moons differ considerably from Mars and are similar in composition to carbonaceous chondrites. The Phobos density is only 1.9 g/cm^3 and lower than that of the materials suggested to be a spectral analogy for the moon. That suggests either a very strong porosity (10-30%) or significant water-ice in the interior. The Deimos density is 0.2 to 1.7 g/cm^3.

Before the Phobos mission almost no experimental data on the Phobos neutral environment were available. The only result related to the subject was a drop in ion density and distortions of the ion energy spectra observed by the Russian Martian probe Mars 5 when it was 20,000 km downstream of Deimos, indicating strong outgassing from this satellite [*Bogdanov*, 1981]. Some theoretical considerations predicted that Phobos may have enough ice in its interior to cause water outgassing at a rate of 10^{22} - 10^{23} s^{-1} [*Fanale and Salvail*, 1989]. In fact, the low Phobos density confirms this suggestion. An interesting mechanism to maintain the neutral Phobos environment was suggested by *Ip and Banaszkiewicz* [1990]. It was found previously that the neutral number density of the hot oxygen planetary corona is of the order of 200 cm^{-3} along the Phobos orbit [*Ip*, 1988a]. The oxygen atoms are captured by the Phobos surface or dust particles, which may exist along the Phobos orbit as will be seen later, and then released with a velocity determined by the surface temperature. Since this velocity is lower than the Phobos orbit velocity, the atoms released are confined in planeto-centric orbits forming a gas torus which would increase the local neutral density by 20%.

In addition to a gas torus, there are several ideas supporting the possible existence of a dust torus / ring along the Phobos orbit. The key point here is that material ejected from Phobos due to meteoroid bombardment has a velocity of a few to a few tens m/s, i.e., much less than the Phobos orbit velocity. Thus the fragments could continue moving in near-circular orbits around the central planet forming a dust torus / ring [*Soter*, 1971; *Banaszkiewicz and Ip*, 1991]. It should also be noted that Phobos lies inside the Roche limit and disintegration of the satellite by tidal forces may occur as well.

The dynamics of dusty grains in the vicinity of Mars have been considered in detail by *Horanyi et al.* [1990]. They have also demonstrated the importance of electromagnetic forces for the grain dynamics at Mars. It was shown that big grains (> 1 μm) form a narrow 'dust belt' while smaller ones (< 0.1 μm) occupy a much wider halo affected by the solar wind. Making assumptions on the rate of meteoroid impacts and calculating a typical volume the grain trajectories could occupy, *Juhasz et al.* [1993] estimated the density of dust particles of different sizes. The most abundant grains turned out to come from Phobos and to be of sizes 0.5 μm and 10 - 50 μm with densities of 10^{-9} - 10^{-10} cm^{-3}. Later on, *Juhasz and Horanyi* [1995] improved the model and took into consideration the radiation pressure perturbation due to the eccentricity of the Martian orbit and the oblateness of the central body. They came to the conclusion that particles of ~15 μm from Deimos (rather than from Phobos!) dominate in the dust torus and have a density of 5×10^{-12} cm^{-3}. We intentionally listed the earlier and recent numbers to illustrate how sensitive the grain dynamics are to the model.

Summing up the pre-Phobos studies, one could roughly say that there were expectations to see "something" in the close vicinity of the moons or their orbits. The plasma instruments onboard the Phobos spacecraft have, indeed, observed plasma disturbances when the spacecraft crossed the Phobos orbit. Some peculiarities were observed even when the spacecraft was located downstream of both the Martian moons. The features listed in Table 1 have been reported for the spacecraft's closest approaches to the Phobos orbit in the solar wind. Note that we are pointing out the most pronounced effects, and that not all of them were observed simultaneously. Figure 7 gives a typical geometry of the observations.

Table 1. Plasma disturbances near the Phobos orbit

Observations	Characteristics	References
Electrons	1. Increase in the electron density up to 10 - 20 cm^{-3}	*Dubinin et al.*, 1990
	2. Suprathermal electrons with energy greater than 50 eV	*Kiraly et al.*, 1991
Ions	1. Solar wind deceleration and a weak deflection	*Dubinin et al.*, 1990
	2. Detection of cold H_2^+, traces of O_2^+ and other molecular ions	*Dubinin et al.*, 1991a *Norberg et al.*, 1993
Plasma density	Disturbances of the spacecraft potential (< 0.5 V)	*Grard et al.*, 1991
Magnetic field	Drop and fluctuations ($\delta B/B \sim 1$) in the magnetic field	*Riedler et al.*, 1989 *Dubinin et al.*, 1990
Waves	Low frequency (1 - 1000 Hz) oscillations	*Grard et al.*, 1991

Similar effects have been observed for the closest approaches to the Phobos orbit not only in the solar wind but in the Martian magnetosphere as well. In spite of the fact that the disturbances in the solar wind may be explained by the magnetic connection with the bow shock, and the observations inside the magnetosphere by the planetary magnetosphere plasma outflow, similar events on two occasions cannot be just coincidence. Moreover, during close approaches of Phobos itself in later phases of the mission, an increase in the density of cold H^+

and H_2^+ ions was observed (some traces of the cold H_2^+ ions have also been detected for the orbit crossings in the solar wind). This enhancement was observed when the spacecraft and Phobos were located in the Martian plasma sheet and the moon's surface was exposed to intensive fluxes of hot electrons. It was suggested that the cold ions result from electron impact ionisation of the Phobos outgassing materials (perhaps water) [*Norberg et al.*, 1993].

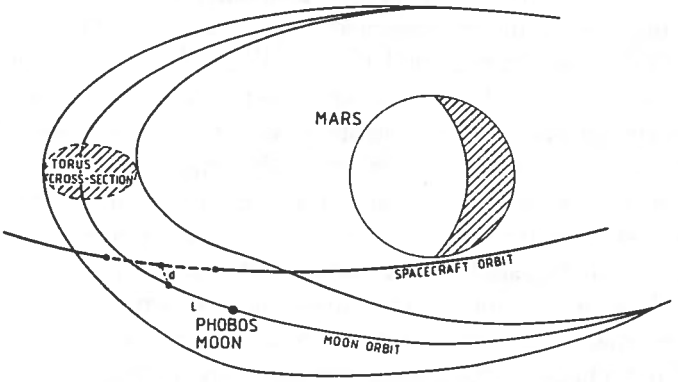

Figure 7. *A schematic representation of the traversal of the Phobos torus by the spacecraft (from Grard et al., 1991).*

Drops in the ion density observed when the spacecraft was downstream of Phobos and Deimos [*Dubinin et al.*, 1990; *Dubinin et al.*, 1991b] might be considered as indications of screening plasma flow in a similar manner as discussed by *Bogdanov* [1981]. Again, every event taken separately may be pure coincidence although together they represent rather convincing evidence for the hypothesis of strongly outgassing moons.

According to *Ip and Banaszkiewicz* [1990] an outgassing flux of 10^{23} s^{-1} results in a peak neutral density along the torus of 2×10^3 cm^{-3}. For rough estimations one can assume that creation of the new O^+ ions via photoionization and escape via picking-up by the solar wind are in balance. The ion number density observed in the event in the solar wind discussed by *Dubinin et al.* [1990] is 10 cm^{-3}, and we arrive at a neutral density of 3×10^5 cm^{-3} that is a factor of 100 higher than expected. Interestingly, analysis of the event during the close approach of Phobos has also revealed a similar "theoretical" deficit of the neutral gas [*Norberg et al.*, 1993].

The Phobos' neutral component in the solar wind plasma can result in effects similar to the Martian exosphere case. We disregard a simple collisional interaction because even for the increased (up to 10^{25} s^{-1}) outgassing it could occur only at about 30 km above the Phobos surface [*Krymskii et al.*, 1992]. Ionization of the neutral component leads to two basic collisionless interactions: solar wind mass-loading and plasma turbulence. For much stronger neutral sources like comets both effects have been clearly observed. The generation of plasma turbulence due to ionization of the hydrogen corona atoms has been observed at Mars (see discussion above). Theoretical estimations for a source as weak as Phobos conclude that for an outgassing of 10^{23} s^{-1} both effects should be negligible [*Ip and Banaszkiewicz*, 1990; *Krymskii et al.*, 1992]. However, a 100 times higher outgassing would result in detectable effects.

Since there have not so far been any planetological reasons to reconsider the composition of the Phobos interior and to increase the matter loss rate, a number of attempts have been undertaken to explain the observed plasma disturbances by the solar wind interaction with the dust ring rather than with the gas torus. The idea is very simple. A dust grain can accumulate up to 700 ϕ r electrons, where ϕ is the grain potential in V (usually up to +/- 10 V) and r the grain radius in μm (up to 100 μm). Thus the grain charge may be up to 7×10^5 and the charge density could be significant. The positively charged grains disturb the solar wind electron flux,

attracting electrons to balance locally the charge density. The resulting motion of electrons with respect to protons leads to current generation and low frequency MHD fluctuations [*Krymskii et al.*, 1992]. Such a scenario may, in principle, explain the observed events. However, in order to cause detectable effects the charge density must be a few percent of that for the solar wind [*Motschmann et al.*, 1992], i.e., 10^{-2} cm^{-2}. This corresponds to a dust density > 10^{-8} cm^{-3} that is much higher than that following from the simulations. Again we come to a disagreement which has not been solved yet.

Electromagnetic forces play a very important role in the Phobos / Deimos dust torus dynamics, because the dust particles orbiting Mars move through different plasma domains of the Martian magnetosphere and collect different electrostatic charges. Perturbations in the submicron particle motion caused by the Lorenz force greatly exceed those due to solar radiation [*Horanyi et al.*, 1990]. Moreover, plasma around Mars may affect not only the dynamics of the dust grains but their mass spectrum as well. *Barabash and Lundin* [1994] suggested that submicron grains might undergo electrostatic disruption in the Martian magnetosheath and generate a population of very fine motes which have such a long charging time that their potential does not follow changes in the plasma conditions while the motes are travelling through the Martian magnetosphere. These particles may stay positively charged even in the eclipse in the Martian magnetotail where they could be attracted by the negatively charged spacecraft. Thus the plasma environment turned out to be important for the dynamics and evolution of the Martian dust torus. It may even play a destructive role through the mechanism invoked by *Barabash and Lundin* [1994].

Finally, the problem of the Phobos / Deimos torus is quite far from being solved. The combined data from imaging, plasma, and plasma wave experiments on upcoming missions are needed to understand better the complicated processes related to dust / neutral / plasma interactions which seem to take place within the Phobos / Deimos dust / gas tori.

ENAs as a Specific Component

ENAs in Space Plasmas

As pointed out already, the charged particles of a hot (energetic) plasma can undergo CE with the atoms of a cold background neutral gas. Two particles emerge from this reaction; a cold ion (sometimes much heavier than the principle plasma ion) and an energetic atom. Up to now, we have been mainly concerned with the dynamic processes resulting from the appearance of cold ions in an energetic plasma. In this section we consider the second product of the CE reaction, the energetic neutral atom (ENA). First of all, let us clarify "energetic". Since ENAs are very important for plasma imaging, i.e., remote determination of the local plasma parameters, it is desirable to have a trajectory of the new-born ENA as close as possible to a straight line. Thus the energy of ENA should be greater than the escape energy for a body where plasma and neutral gas coexist. The hydrogen escape velocity for the largest planet Jupiter is only 13 eV but for the Sun it is about 2 keV. Thus neutral atoms emerging from hot plasma can be considered as energetic for almost all objects within the Solar system. On the basis of the different experimental techniques used for the neutral detection, all ENAs can be divided into two groups; high energy neutral atoms (HENAs) with energy > 10 - 15 keV and low energy neutral atoms (LENAs) with energy 10 eV - 15 keV. In this section we consider ENAs in general and discuss properties which are common for both HENA and LENA.

The basic properties of ENAs generated in space plasmas are determined by the CE process, as follows.

(1) Due to its neutrality, an ENA is decoupled from the primary plasma.

(2) The moment of a primary ion is conserved for CE reaction and, hence, an immersed ENA carries information on the initial ion energy distribution.

(3) The ENA flux at a certain point is given by the integral along the line-of-sight.

(4) The ENA flux is very low because the CE cross section is small. Indeed, the ratio of the ENA differential flux to the local ion differential flux, η, can be estimated as $\sigma N L$, where σ is the CE cross section, N the density of the background neutral gas, and L the typical size of the plasma region. For the Earth's equatorial ring current at $4R_e$, η for 25 keV ENAs is only 0.03%.

(5) The vast majority of the Solar system plasmas are proton plasmas. Thus one would expect ENAs to be, mainly, hydrogen atoms. However, in the vicinity of the planetary bodies, oxygen and helium contribute to the net ENA flux. Near Jupiter and Saturn, energetic molecules are possible.

Besides the CE process, significant fluxes of ENA in space can be generated in a recombination process under conditions of high electron density and very long integration distances. These may be found in coronal mass ejections (CME) as suggested by *Hsieh et al.* [1992] (see also *Gruntman* [1994b]). In this case η is of the order of 10^{-6} - 10^{-5} for 2 - 5 keV ENAs but the absolute flux is above detection limits. It is interesting to note that these ENAs arrive at the Earth several hours earlier than the "mother" ejecta and, hence, may be used to forecast CME related geomagnetic storms.

ENAs can be found near almost all objects within the Solar system. Indeed, the plasma which is always present in the interplanetary medium can interact with the exospheres of planetary nonmagnetic bodies. Hot magnetospheric plasmas interact with upper atmospheres / exospheres and the neutral environments of satellites orbiting the planets. Even some of the asteroids appear to have some outgassing which might create a neutral environment [*Russell*, 1987]. Comets are obvious objects where plasma strongly couples with neutrals [*Ip*, 1988b].

Table 2. ENAs in Space Plasmas

ENA source	Energy, keV	Flux, $(cm^2\ s\ sr\ keV)^{-1}$	Angular size	Species
Interstellar medium [a, b]	0.013 [1] 0.050 [1]	$5\times10^5\ cm^{-2}s^{-1}$ $0.5\times10^5\ cm^{-2}s^{-1}$	15° × 15° @ 1-5 AU	H He
Heliospheric shock [c]	0.2 - 1	$200\ cm^{-2}\ s\ sr^{-1}$ @ 1 AU	Highly anisotropic	H
Interplanetary shocks [d]	10 100	50 0.04		H
CME [e]	2 - 7	10^4 @ 1 AU	5° × 5°	H
Mars' magnetosphere [f]	1 - 8 20 - 80	10^5 - 10^6 0.1 - 5 @ 1 R_m	2π	H, O
Terrestrial magnetosphere	10 - 20 [2, g] 20 - 30 [h]	10^3 - 10^4 10 - 10^2 @ 5 R_e	5° × 5° 20° × 20°	H, O, He
Artificial sources in the Earth's magnetosphere (explosions) [i]	10 - 100	10 - 100 @ 2000 km	45° × 45°	H
Jovian magnetosphere [j]	15 - 65	$0.04\ cm^{-2}s^{-1}keV^{-1}$ @ 100R_J	Point source	
Saturnian magnetosphere [k]	> 40	$0.12\ cm^{-2}s^{-1}keV^{-1}$ @ 45R_S	Point source	
Outgassing asteroids (Phobos) [f]	1 - 5	10^4 - 10^6 (?)	5° × 5°	H, O(?)

[1] 27 km/s from the spacecraft motion
[2] low altitude precipitation region
[a] *Holzer*, 1977
[b] *Witte et al.*, 1993
[c] *Gruntman*, 1992
[d] *Roelof*, 1992a
[e] *Hsieh et al.*, 1992
[f] *Barabash et al.*, 1995a
[g] *Chase et al.*, 1995b
[h] *Roelof et al.*, 1992b
[i] *McComas et al.*, 1993
[j] *Kirsch et al.*, 1981a
[k] *Kirsch et al.*, 1981b

Moreover, the entire heliosphere is immersed in a cold neutral background, the very local interstellar medium, that results in the ENA production from different plasma structures in the interplanetary medium. In fact, the heliosphere as a whole seems to be a LENA source in the interstellar medium. Table 2 gives a brief overview of the typical parameters which characterize the ENAs generated near or by different objects within the Solar system. Note, that due to the Sun's motion with respect to the galactic center the interstellar neutrals have a nonzero energy and can be considered as LENAs.

So, ENAs can be generated in almost any region of interest for space plasma physics. Generally speaking, one could consider ENAs as a specific component in space plasmas which are immersed in the background neutral gas. The main property of this component is its neutrality. This means that the dynamics of the ENAs are not affected by electromagnetic forces and they propagate like photons. Such straight-line paths suggest that the ENAs can be detected from different directions to form an image of the ENA emitting region in a manner similar to usual photography. Thus we obtain a way to make space plasmas "visible". This approach is particularly important for proton plasmas, which cannot be imaged remotely by any other means, because a nonrelativistic proton does not emit any radiation.

The ENAs make "visible" not only plasma but a neutral component as well, because they are a result of the CE process and an enhancement in neutral density gives rise to the ENA production increase. Thus dense neutral structures immersed in a plasma background can be observed remotely. Table 2 lists, for example, the ENAs generated by cold gas releases in the Earth magnetosphere. The releases usually result from explosions of man-made objects in space and, in fact, these ENAs can be used even for reconnaissance purposes. Another example (more peaceful) is the imaging of the Titan exosphere which interacts with the hot plasma of the Saturnian magnetosphere. Such studies are planned for the ENA instrument INCA of the Cassini mission [*Cheng et al.*, 1993].

Because of charge neutrality, ENAs are decoupled from the primary plasma. If the ENA flux becomes significant, it can absorb plasma momentum and modify the plasma distribution function as we saw in the Martian case. In addition, charged particles can be transported perpendicular to the magnetic field by means of ENAs. An ENA produced in one region can travel to another location unaffected by the Lorenz force and be re-ionized there, resulting in a new plasma population. The low altitude ring current and auroral ENAs are typical illustrations of such a process. Another example is ENAs generated in the outer cometary coma. These can reach the inner coma and be re-ionized via interaction with neutral gases. These new-born ions will appear as a hot (0.1 - few keV) ion population within the cold cometary coma plasma. This scenario has been invoked by *Goldstein et al.* [1987] to interpret the observations of a sudden increase of the 200 - 300 eV ions near the contact surface of the Halley comet. A similar idea of mass and energy transport via ENAs was discussed by *Barbosa and Eviatar* [1986], who considered planetary magnetospheres (Earth, Jupiter, Saturn) as sources of ENAs flowing out into interplanetary space. They used the term "fast neutral winds" and, in this sense, the magnetospheres resemble cometary comas. Being re-ionized in the solar wind, ENAs can cause effects similar to those observed in the solar wind plasma near comets, namely, a small mass-loading effect (< 10%), substantial ion heating (> 100%) and generation of ion cyclotron waves.

Despite many interesting properties of this unusual component, the most important reason why the ENAs are so attractive for space plasma physics is, of course, the possibility to use them for plasma imaging. For almost all aspects of ENA imaging, the plasmas in question may be considered as ENA thin, because the electron stripping cross section is smaller than the CE cross section and typical ion densities are much lower than the neutral densities. Thus assuming the ENA attenuation is negligible, we have for the ENA differential flux, $J_{ena}(\underline{r}, E, \underline{u})$, from the direction $\underline{u}$ in the vantage point $\underline{r}$ at the energy E

$$J_{ena}(\underline{r}, E, \underline{u}) = \sigma(E) \int_0^{\infty} ds\, N(\underline{r} - \underline{u}s)\, J_{ion}(\underline{r} - \underline{u}s, E, \underline{u}) \qquad (2)$$

where $\sigma(E)$ is the energy dependent cross section, $N(\underline{r} - \underline{u}s)$ and $J_{ion}(\underline{r} - \underline{u}s, E, \underline{u})$ the neutral density and the ion differential flux at the point of the ENA generation. The integration is performed along the line-of-sight s. The basic information to be obtained in ENA imaging is the ion distribution $J_{ion}(\underline{r} - \underline{u}s, E, \underline{u})$ for all $\underline{r}$ within a region of interest. It is, indeed, possible to unfold, because $N(\underline{r} - \underline{u}s)$ is usually known and we come to a common inversion problem. The simplest way to solve it is to describe the unknown function, $J_{ion}(\underline{r} - \underline{u}s, E, \underline{u})$, parametrically, then simulate the expected ENA images using an instrument function, define the difference between the simulated and measured images, and, finally, change the model parameters to minimize this difference. The inferred ion distribution is given by an optimal set of parameters. This method is known as forward modelling and was used by *Roelof* [1987] to reconstruct a global ion distribution for the storm-time ring current in the Earth's magnetosphere using a HENA image obtained by the ISEE 1 spacecraft. This technique is the basis for ENA imaging. Using this approach one may obtain global spatial distributions of the hot plasma and then deduce several important quantitative characteristics, for example, the global current system [*Roelof*, 1989].

The importance of a global perspective in magnetospheric physics has been understood for some time [*Williams*, 1990]; however, only now has it become possible. In order to obtain a comprehensive view on the most explored plasma system, the Earth's magnetosphere, ENA imaging is not sufficient. The cold plasma of the plasmasphere, one of the most important parts of the inner magnetosphere, does not produce ENAs. Thus complementary techniques are needed. The best candidate is imaging the plasmaspheric He^+ via the solar 30.4 nm scattered line. He^+ tracks the H^+ quite well, exhibiting essentially the same structures. The global structure revealed by He^+ images can be taken as a picture of the plasmasphere which evolves as a manifestation of global electrodynamics. A view of the dynamic plasmasphere with "ripples", "tails", "detached plasma regions" etc. obtained from years of localized plasmaspheric observations could be immediately established by such extreme UV images. In order to see the visible result of global electrodynamics we have to complete the global view of the entire magnetospheric system, the ring current - plasmasphere - atmosphere, by auroral imaging. The latter will also put observations made by the two novel techniques of ENA and He^+ imaging in context with those already made. Altogether, the three techniques form the basis for global magnetospheric imaging as proposed by *Williams et al.* [1992].

The global imaging has another aspect [*Williams et al.*, 1992]. The availability of both global and *in situ* observations of the magnetosphere places us in a unique position in the study of cosmological plasma environments. For example, astrophysics and solar physics have had to rely exclusively on remote observations and from these have been inferred the local processes thought to be responsible for the global behaviour. In contrast, magnetospheric physics has obtained detailed *in situ* measurements within a number of planetary magnetospheres, and from these has synthesized a picture of the global system. The capability of imaging magnetospheric plasmas marks the opportunity where an astrophysical plasma system (the Earth's magnetosphere) that has been well characterized by *in situ* measurements can also be characterised globally by remote sensing. Thus qualitatively new understanding of the behaviour of complex astrophysical plasma systems can be achieved.

ENA in the Terrestrial Magnetosphere

In the preceding section we reviewed briefly a specific component, ENAs, and described the general possibility of imaging plasmas by measuring ENAs produced in the CE process with a background neutral gas. With this section we focus on the terrestrial magnetosphere and

discuss particular features of the ENAs and ENA imaging in the Earth plasma - neutral environment.

For all regions of the Earth's magnetosphere except low altitudes (< 2000 km) the only neutral species present in significant numbers is hydrogen. However, below 2000 km the relative importance of neutral atmospheric densities of H and O is a strong function of solar activity, as shown in Figure 8. Thus production of low-altitude ENAs is inherently time dependent.

There are both models and data from which one can compute neutral hydrogen densities at high altitudes. The neutral hydrogen density as a function of height, h, conforms approximately to the Chamberlain model (Formula 1 with the Earth's parameters) with T = 1050 K which provides the best fit to the DE-1 geocoronal observations [*Rairden et al.*, 1986]. The density profile is shown in Figure 9. As expected, it falls off quickly with radial distance, but with an increasing scale height with radius such that even at 10 - 12 R_e, $N \approx 10$ cm^{-3}. The high geocoronal density at low altitudes results in relatively enhanced ENA emission from these regions, but a large source region length can result in significant ENA emission for most magnetospheric regions. The neutral density distribution is approximately spherically symmetric throughout the inner magnetosphere, but there is an excess on the nightside in the outer magnetosphere. The DE-1 results indicated that this excess is about a factor of 2 enhancement.

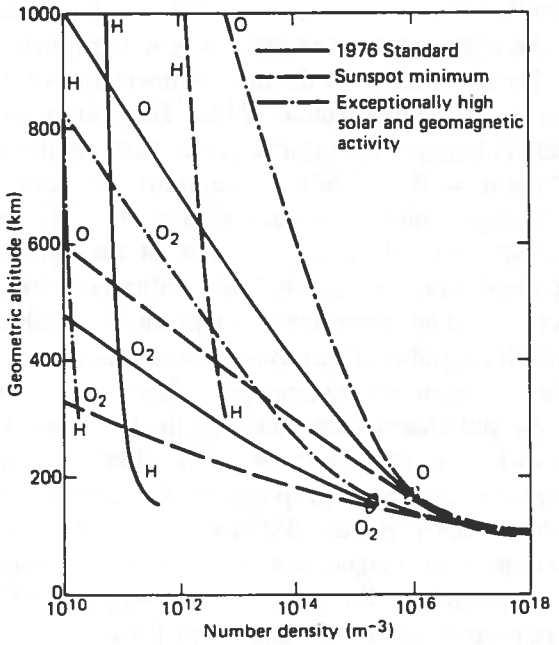

Figure 8. *Atmospheric density versus altitude for H, O, and O_2 for sunspot minimum, maximum, and average activity [U.S. Standard Atmosphere, 1976].*

The most attractive part of the Earth's magnetosphere for ENA imaging is the ring current because, on the one hand, its dynamics are of great importance for the global magnetospheric dynamics and, on the other hand, the neutral density in this region is still high enough to perform ENA imaging with reasonable temporal resolution. The ion flux of the ring current is strongly attenuated inside $2R_e$ by CE losses with the exosphere, tending to peak roughly around L = 3 - 4 and then decaying approximately exponentially with increasing L. Here L is defined as the equatorial radius in R_e of a given magnetic field line. The outer limits of the ring current are set by the combined effects of electric-field convection and the injection of fresh

energetic ions from the nightside plasma sheet. The ENA flux coming from the inner parts of the ring current is the highest.

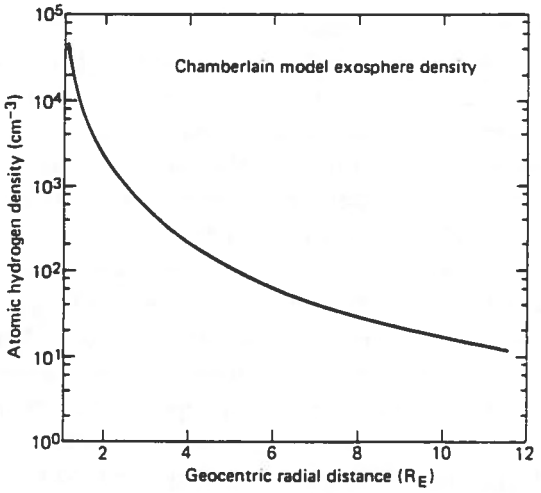

Figure 9. *Chamberlain exospheric hydrogen density verses radial distance (from Rairden et al., 1986).*

The first observations of ENAs generated in the ring current were made by charged particle solid state detectors (SSDs). A persistent anti-earthward flux of 0.3 - 0.5 MeV particles detected in interplanetary space on the IMP 7 satellite during quiet solar conditions and reported by *Krimigis et al.* [1975] was interpreted by *Hovestadt and Scholer* [1976] as ENA emissions. *Roelof et al.* [1985] observed a similar anti-earthward flux at much lower energies (~50 keV) with SSDs on the IMP 7/8 and ISEE 1 satellites at distances 33R_e and 20 R_e. The count rate was rather low but the very narrow angular distribution of the fluxes, always coming from the direction of the radiation belts, lead to conclusions that these emissions must have been ENAs produced in the ring current during storm recovery phase. The estimated unidirectional ENA differential flux was 30 $cm^{-2}s^{-1}sr^{-1}keV^{-1}$ at 20 R_e for 100 keV particles. These were identified as oxygen by comparison between the measured decay rates in two energy channels and calculated decay rates for the different ring current constituents H^+, O^+, and He^+. Having proved that the anti-earthward flux detected on the ~50 keV energy channel by the SSD on ISEE 1 was indeed ENAs, *Roelof* [1987] obtained an ENA image of the storm-time (D_{st} = -241 nT) ring current from 2.6 R_e. Using the forward modelling technique, he calculated a ring current ion distribution which implied a strong (> 20:1) midnight/noon ion intensity asymmetry. The ENA fluxes (whether H or O) exceeded 10^3 $cm^{-2}s^{-1}sr^{-1}keV^{-1}$ at maximum. This work was proof-of-concept of the ENA imaging technique discussed above. Unfortunately, since ISEE 1 no new measurements have been available for further analyses and a great deal of effort was directed to improvement of unfolding techniques [*Roelof et al.*, 1993] and numerical simulations using different initial ion distributions [*Roelof et al.*, 1992b; *Orsini et al.*, 1994].

Energetic charged particles trapped at low altitudes (< 1000 km) near the geomagnetic equator are indirect evidence of the ENA generation within the ring current. Indeed, after generation in the ring current region the ENAs propagating towards the Earth reach low altitudes, where they get re-ionized by ionisation collisions. New-born ions become only temporarily trapped because the lifetime at these altitudes is much shorter than the drift period. The ions have typically 90° pitch-angle and an altitude profile that increases rapidly in intensity between 180 and 260 km, becoming nearly independent of altitude thereafter. These ions have been observed in a number of satellite and rocket experiments [*Hovestadt et al.*,

1972; *Moritz* 1972; *Mizera and Blake*, 1973; *Butenko et al.*, 1975; *Scholer et al.*, 1975; *Voss et al.*, 1984; *Miah et al.*, 1992; *Voss et al.*, 1993]. *Voss et al.* [1993] have also measured directly the ENA flux over the 400- to 900-km altitude region near the equatorial plane with the IMS-HI energetic particle detector on the CRRES mission. The integral ENA flux above 40 keV at 600 km was found to be 500 $cm^{-2}s^{-1}$ during a substorm with D_{st} =-325 nT at maximum. Besides the direct detection and indirect particle measurements of the low altitude trapped ions, the ENA at low altitudes (sometimes called precipitating neutral atoms) can be indirectly observed by optical measurements either through their own EUV emissions [*Meier and Weller*, 1975] or through emissions of the upper atmospheric atoms excited by collisions with the precipitating ENAs [*Tinsley*, 1979; *Tinsley et al.*, 1984; *Tinsley et al.*, 1986]. These emissions from N_2^+ and O I were, for example, observed even for quiet magnetospheric conditions by the Energetic Neutral Atom Precipitation experiment on ATLAS 1 [*Tinsley et al.*, 1994]. Their latitude profile and average energy deposition rates of (3 - 12)$\times 10^{-4}$ erg $cm^{-2}s^{-1}$ estimated on the basis of these observations were consistent with models. We should note, however, that the upper atmospheric emissions resulting from the precipitating atoms and emissions from the precipitating ions of the same energy and mass are indistinguishable. This is because fluxes of either primary neutrals or primary ions go through repeated cycles of charge exchange and stripping, producing mixed beams after the first collision in the upper thermosphere [*Tinsley et al.*, 1994].

Energetic ions (H^+, O^+, He^+) from the ring current that are incident on the upper atmosphere at low altitudes (< 800 km) and mid-latitudes are rapidly converted to energetic atoms through the CE process. These ENAs propagating downward result in significant effects in the thermosphere. The most important ones are heating and ionisation [*Ishimoto et al.*, 1986; *Ishimoto and Torr*, 1987; *Ishimoto et al.*, 1992a, 1992b]. For example, during a geomagnetic storm the heating rate due to energetic neutral oxygen (< 17 keV) at 180 km altitude is twice that from noon solar EUV energy deposition [*Ishimoto et al.*, 1986] and the total heating is of the order 2 erg $cm^{-2}s^{-1}$. If the modelled results are correct, then the ENAs play an important role not only in particle transfer across the magnetic field but in the energy transfer as well. In this sense the precipitating ENAs constitute a link between the upper atmosphere at middle and low altitudes and the radiation belt / ring current [*Orsini et al.*, 1992].

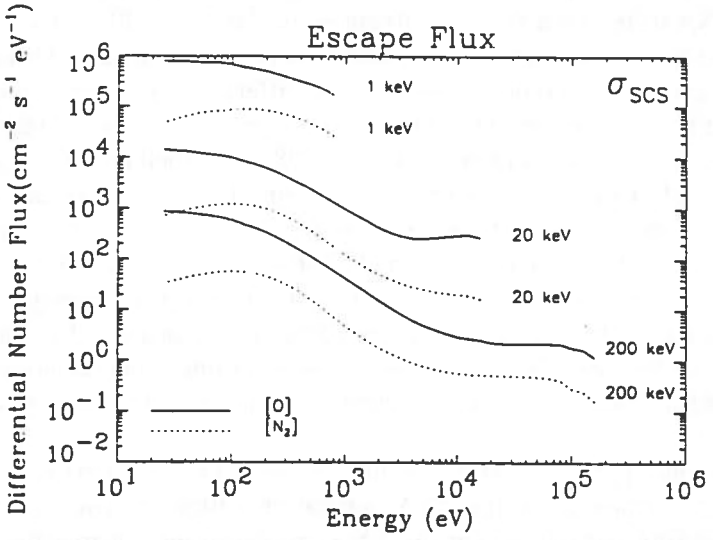

Figure 10. *Energy spectra of the escaping O and N_2 for three different monoenergetic particle inputs of 1 erg $cm^{-2}s^{-1}$ [Ishimoto et al., 1992a]. The spectra were obtained in numerical simulations using an O^+ transport model [Ishimoto et al., 1986] revised to estimate the thermospheric interaction of precipitating O^+ up to 200 keV. 1 erg $cm^{-2}s^{-1}$ corresponds to 1.6×10^6 $cm^{-2}s^{-1}eV^{-1}$ for 1 keV, 8×10^4 $cm^{-2}s^{-1}eV^{-1}$ for 20 keV, and 8×10^3 $cm^{-2}s^{-1}eV^{-1}$ for 200 keV*

Besides thermospheric heating, the ions / ENAs precipitating on the upper atmosphere in mid-latitudes cause another interesting effect. Due to momentum transfer in elastic and non-elastic collisions and a cascade of CE and electron stripping processes, a fraction of the ion incident flux can be scattered back and escape the atmosphere in the form of ENAs. For example, the total escape flux of O varies from 50% for 1 keV to approximately 20% for 200 keV precipitating O^+ ions [*Ishimoto et al.*, 1992a]. Figure 10 gives illustrative energy spectra of the escaping O and N_2 for three different monoenergetic particle inputs of 1 erg $cm^{-2}s^{-1}$ [*Ishimoto et al.*, 1992a]. The spectra were obtained in numerical simulations using an O^+ transport model [*Ishimoto et al.*, 1986] revised to estimate the thermospheric interaction of the precipitating O^+ up to 200 keV. Using measured spectra of the precipitating ions (< 17 keV) at 800 km altitude, *Ishimoto et al.* [1992b] estimated energy spectra and absolute fluxes of the escaping ENA. The latter were found to be 10^5 - 10^7 $cm^{-2}s^{-1}sr^{-1}keV^{-1}$ for the energies 1 - 10 keV, i.e., very significant.

The back-scattered atoms (O and, perhaps, H) form a kind of albedo of the Earth in ENAs. Since the ENA albedo intensity is proportional to the precipitating ion flux, it maps the *L-MLT* pattern of the ion distribution to the latitude-longitude picture and may be used to examine the O^+ and H^+ precipitation under disturbed geomagnetic conditions [*Chase et al.*, 1995a].

ENAs resulting from the particle precipitation on the upper atmosphere can be detected via Doppler-shifted H_α and H_β lines. Such measurements have been carried out with ground based instruments [*Meinel*, 1951] and photometers on sounding rockets [*Søraas et al.*, 1994]. However, only recently, *Søraas and Aarsnes* [1995] reported on direct ENA detection in the auroral region. In their experiment a rocket equipped with SSDs sensitive to ions / ENA with energy > 20 keV reached an altitude of 454 km during a substorm. A strong azimuthal asymmetry was observed at 90° pitch-angle at the higher altitudes while at the lower altitudes the azimuthal distribution was isotropic. This was interpreted as ENAs coming from the most intense region of proton precipitation. The highest asymmetry was observed in the lowest (20 - 30 keV) energy channel as would be expected from the CE cross section dependence. The ENA pitch-angle distribution was found to be 20° - 50° wide.

Above, we were mainly discussing HENAs generated in the ring current. However, the high energy ion component occupies only the inner part of the ring current and is not the only constituent of the complicated terrestrial magnetospheric plasma environment. The majority of the magnetospheric plasma is less energetic; for example, the plasma sheet and the magnetosheath ion populations. Moreover, the CE cross section for neutral atom creation decreases rapidly at energies above 20 - 30 keV and, hence, LENAs are an important component in the magnetospheric plasmas as well. In fact, most of the magnetosphere radiates appreciably higher fluxes of LENAs than HENAs.

The LENAs cannot be detected by common techniques applicable for energetic charged particles, because their energy is too low. On the other hand, the direct use of low energy particle detectors such as channel electron multipliers (CEMs) and microchannel plates (MCPs) is not possible either, due to the high UV photon background. An effective separation of the LENAs from the UV photons must be made in a LENA instrument. Because of this problem, the LENAs have not been unambiguously observed in space so far. The only attempt to measure LENAs in the terrestrial magnetosphere with a specifically designed instrument launched to 840 km altitude as a part of the Solar eclipse Rocket Program gave unrealistically high LENA fluxes of 10^9 - 10^{10} $cm^{-2}s^{-1}sr^{-1}keV^{-1}$ at energy 1 - 2 keV [*Wax et al.*, 1970]. However, a private communication from the authors indicates that their results were spurious [*Moore and Opal*, 1975]. At present, the intensive simulation work on the global LENA distribution within the magnetosphere is conducted to prove the feasibility of the LENA imaging [*Moore et al.*, 1992; *Moore et al.*, 1993 (empirical model of the magnetosphere); *Moore et al.*, 1994 (Rice University Magnetospheric Specification Model)]. Its basic principles are the same as those for HENAs. However, the modelling results reveal a new exciting

possibility of imaging the plasma sheet that cannot be done with high energy (> 30 keV) atoms. The modelled images give LENA fluxes of 100 - 300 $cm^{-2}s^{-1}sr^{-1}keV^{-1}$ at 5 keV for quiet and storm conditions from the plasma sheet as seen from $9R_e$ on the dusk side of the Earth at the geomagnetic equator. These LENA images also show such features of the plasma sheet morphology like thinning and plasmoid formation developed during substorms [*Moore et al.*, 1992]. The main conclusion from the numerical simulations is that the LENA imaging is, indeed, possible, but instruments with large geometrical factors (> 1.0 cm^2 sr) are required [*Moore et al.*, 1994].

LENAs can be produced by even less energetic plasma than discussed above. For instance, *Hesse et al.*, [1993] considered the LENA generation in the cleft fountain, a region of intense O^+ transverse ion energization at altitudes from 2000 to 10000 km on the dayside of the magnetosphere. A global view of the base of the cleft ion fountain and the transverse energization region is needed for correct interpretation of previous local measurements. Typical energies of these LENAs are 10 - 30 eV, which is close to the instrument detection limits. Thus a very sophisticated instrumentation is required for such kind of imaging. A typical flux given by the simulation is $(2 - 10)\times10^3$ $cm^{-2}s^{-1}sr^{-1}$ with a typical angular dimension of 10° at $2R_e$ [*Hesse et al.*, 1993].

To sum up our brief overview of ENAs in the terrestrial magnetosphere we list their representative fluxes and energies for the different magnetospheric regions (Table 3).

Table 3. ENAs in the Earth's Magnetosphere

ENA source or region	Energy, keV	Flux, $(cm^2\ s\ sr\ keV)^{-1}$	Distance	Species
Low-altitude precipitation region [a]	> 20	10^3	500 km - $2R_e$	H, O
ENA albedo [b]	1 - 10	10^5 - 10^7	600 km altitude	H, O, N_2
Equatorial ENA precipitation [c]	10 - 100	10^3 - 10^4	≈ 300 km altitude	H, O, He
Equatorial storm-time ring current	> 30 [a] 1 - 10 [d]	15 30 - 200	2 - 10R_e 9R_e	H, O, He (?)
Equatorial quiet-time ring current	> 30 [a] 1 - 10 [d]	0.1 - 1 10 - 30	2 - 10R_e 9R_e	H, O, He (?)
Plasma sheet [e]	5	100 - 300	9R_e	H
Cleft ion fountain [f]	0.01 - 0.03	10^3 - 10^4	2R_e	O

[a] *McEntire and Mitchell*, 1989
[b] *Ishimoto et al* 1992b
[c] *Tinsley*, 1994
[d] *Moore et al.*, 1993
[e] *Moore et al.*, 1992
[f] *Hesse et al.*, 1993

ENA in the Martian Plasma Environment

To date, very little is known about ENA generation near planets other than the Earth. Measurements made by instruments not specifically designed for the purpose gave some indications which could be interpreted as ENAs generated at Jupiter [*Kirsch et al.*, 1981a; *Witte et al.*, 1993] and Saturn [*Kirsch et al.*, 1981b]. Using these very limited observations *Cheng* [1986] suggested the following sources of the ENAs near the giant planets: the Jupiter Io torus and outer parts of the magnetosphere where sufficient neutral density is created by the electron capture of corotating ions. Near Saturn, ENAs seem to be generated in the H_2O clouds within the inner magnetosphere. *Hsieh and Curtis* [1988b], using the same observations, tried to produce an image of the Saturn / Titan system seen in ENA. Recently, in a frame of the feasibility study for the ENA instrument for the Cassini mission, extensive simulation of the ENA imaging in the Saturn / Titan system has been carried out [*Cheng et al.*, 1993; *Amsif et al.*, 1995].

Although more Martian missions have been carried out and more are planned than those to Saturn or Jupiter, ENAs and their generation have never been studied near Mars. Only some calculations have been performed to estimate the efficiency of the charge exchange process and its dynamic manifestations, like a shift of the bow shock position, the solar wind depletion, etc. (see the review in the "Martian" part of this dissertation). Figure 11 gives a general impression of the efficiency of the CE process at Mars and Venus [*Russell et al.*, 1983]. According to these calculations some 4% of the solar wind particles can be converted to ENAs. However, the results using the Phobos measurements give a higher absorption of 8% [*Barabash and Kallio*, 1995c]. In any case one can see that a typical efficiency (η) can be much higher at Mars than, say, for Earth conditions. Note that Venus looks even more promising for the ENA imaging because of the higher ENA fluxes expected.

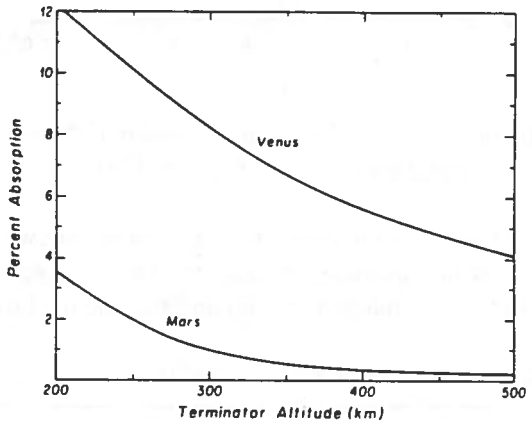

Figure 11. *Percent absorption of solar wind protons through CE at Venus and Mars for streamlines which at infinity are within one planetary radius of the sun-planet line. Absorption is plotted versus altitude at the terminator of the lowest stream line (from Russell et al., 1983).*

The Martian neutral environment has been described in the preceding sections but possible ENA generation regions by *Barabash et al.* [1995a]. To date, the latter is the only work dealing with the subject. Since it is included in the dissertation as Paper VIII, we only emphasise the most important features of the ENA imaging near Mars and give a more extended discussion of the ENA generation for the energy range > 10 keV because several important details were omitted in the publication by *Barabash et al.* [1995a].

Imaging of the ENAs (in fact, LENAs, because a typical energy is 150 - 400 eV) originating from the shocked solar wind within the Martian magnetosheath opens a possibility to define the shape of the boundary separating the solar wind and the Martian magnetosphere.

The most intense LENA flux comes from a line tangential to the obstacle, because there the plasma stream lines pass the highest neutral density. Making imaging from different spacecraft positions, i.e., different α in Figure 1 in *Barabash et al.* [1995a], one can determine the shape of the obstacle. Note that we do not need *a priori* any knowledge of the ion distribution to get the size of the obstacle which is the fundamental parameter characterizing the solar wind - Mars interaction. Only the observation geometry is required.

Besides, the LENAs can be generated in the Martian upper atmosphere in a manner similar to the terrestrial ENA albedo, but the precipitating ions are pickup ions resulting from ionisation of the exospheric components. The most energetic ions are O^+. They have a large gyro-radius and can re-enter the Martian upper atmosphere and cause sputtering neutral atoms there [*Luhmann and Kozyra,* 1991]. This process occurs, mainly, on the day side. The energy spectrum of the sputtered oxygen is shown in Figure 12.

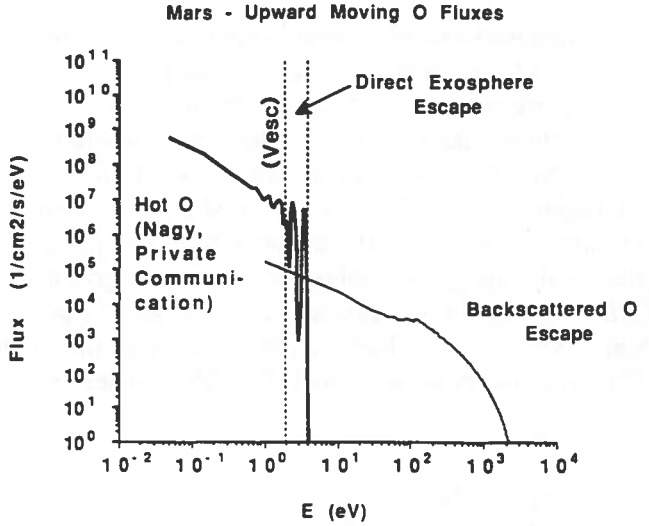

Figure 12. *Calculated LENA flux from the pickup O^+ ion precipitation (from Luhmann and Kozyra, 1991).*

HENAs (E > ~10 keV) may result from the CE process between the Martian neutral environment and the nonthermal protons present in the shocked solar wind as well as accelerated planetary ions in the tail, magnetosheath and outside the bow shock.

Table 4. Energetic plasma environment of Mars [a]. The fluxes are in $cm^{-2}s^{-1}sr^{-1}keV^{-1}$.

Energy channel, keV	Subsolar magnetosphere	Upstream and downstream of the bow shock at terminator	Magnetosheath at the terminator	Magnetotail, near midnight
34 - 51 (p) 55 -72 (O^+)	50	100 - 200	60	50
51 - 202 (p) 72 - 223 (O^+)	0.2 - 2		12	

[a] *Afonin et al.*, 1989; *Afonin et al.*, 1991; *McKenna-Lawlor et al.*, 1993

The monitoring of the energetic plasma environment of Mars in the range of 34 keV - 3. 2 MeV has been performed by the SLED instrument aboard the Phobos spacecraft and four regions of energetic ion enhancements have been identified [*Afonin et al.*, 1989; *Afonin et al.*, 1991; *McKenna-Lawlor et al.*, 1993]. A compilation of these results is shown in Table 4 for the two lowest energy channels. Since the SLED instrument did not resolve masses, the accurate identification of ions is not possible. Thus we will compute neutral fluxes for both protons (p) and oxygen (O^+) because the cross section of the charge exchange process is different for these ions (Figure 1).

The above measurements have been carried out along a circular orbit at altitude 6000 km except for the enhancement in the subsolar magnetosphere where the altitude was 900 km. We will estimate the HENA flux, J_{hena} (E), according to the expression J_{hena} (E) $\approx \sigma$(E) J_{ion} $N L$, where J_{ion} is the ion flux from Table 4 and L the effective path over which the transcharging takes place. We assume the CE process with the hydrogen exosphere and N(900 km) $\approx 2 \cdot 10^4$ cm^{-3} [*Barabash and Norberg*, 1994] and N(6000 km) $\approx 10^3$ cm^{-3} [*Barabash et al.*, 1991]. It is reasonable to suggest that L is of the order of the typical altitude, i. e., $L \approx 1000$ km for the subsolar magnetosphere enhancement and $L \approx 10000$ km for the other regions. By doing so we overestimate the possible HENA flux, but our intention is to obtain upper limits for these very low fluxes. Combining them all and taking the energy dependant cross section (see Figure 1) we get the HENA fluxes shown in Table 5.

Table 5. HENA(E > 34 keV) environment of Mars. The fluxes are in $cm^{-2}s^{-1}sr^{-1}keV^{-1}$.

Energy channels, keV	Subsolar magnetosphere	Upstream and downstream of the bow shock at terminator	Magnetosheath at the terminator	Magnetotail, near midnight
34 - 51 (p)	$2 \cdot 10^{-2}$	$< 4 \cdot 10^{-2}$	$1.2 \cdot 10^{-2}$	10^{-2}
55 -72 (O^+)	$5 \cdot 10^{-2}$	$< 10^{-1}$	$3 \cdot 10^{-3}$	$2.5 \cdot 10^{-2}$
51 - 202 (p)	$< 6 \cdot 10^{-5}$		$2 \cdot 10^{-4}$	
72 - 223 (O^+)	$< 10^{-4}$		$4 \cdot 10^{-3}$	

As one can see the fluxes are extremely low and do not exceed 1 - 2 $cm^{-2}s^{-1}sr^{-1}$ for tens of keV particles. The most promising region in terms of HENA detection is the bow shock.

Somewhat better can be done with accelerated planetary ions in the range 10 - 30 keV not covered by the SLED instrument. These ions, primarily O^+, result from photoionisation of the Martian oxygen corona and move on cycloid orbits in the crossed electric and magnetic fields of the solar wind, gaining energy up to 32 times the solar wind energy. Detailed modelling of the distribution of such ions has been performed by J. Luhmann [*Luhmann and Schwingenschuh*, 1990; *Luhmann*, 1990]. Figure 13 taken from *Luhmann* [1990] shows the omnidirectional flux of the pickup O^+ ions at several positions (x) downstream.

The HENA flux generated by these ions can be estimated in a similar way as was done for the ENA inside the Martian magnetosphere (the source (3) by *Barabash et al.* [1995a]). For the CE process between 20 keV O^+ ions of flux $3 \times 10^4 / 2\pi$ / 10 keV $cm^{-2}s^{-1}sr^{-1}keV^{-1}$ with hydrogen σ equals 7×10^{-16} cm^2 and J_{ena} becomes 0.3 - 0.4 $cm^{-2}s^{-1}sr^{-1}keV^{-1}$. This is higher than the numbers deduced on the basis of the SLED measurements due to lower energy. According to *Luhmann and Schwingenschuh* [1990] the flux of the pickup ions can increase up to 13 times in a more energetic solar wind with a Mach number 6 and a magnetic field of 1 nT. That gives $J_{ena} \approx 5$ $cm^{-2}s^{-1}sr^{-1}keV^{-1}$. Moreover, the angular distribution of these ions can be narrower than the assumed one and the differential flux, correspondingly, higher.

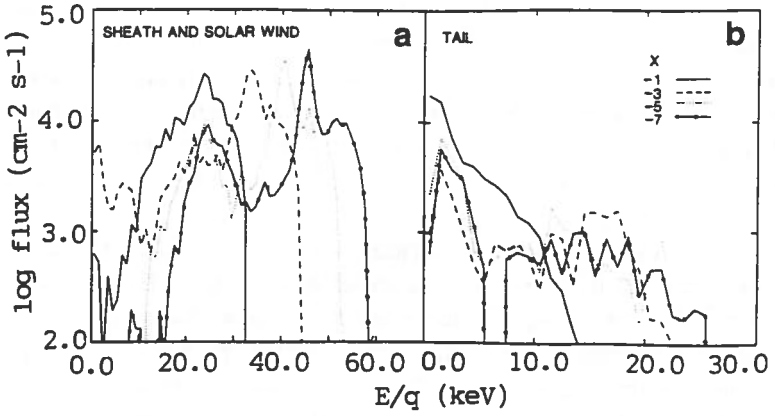

Figure 13. *Omnidirectional flux of the O^+ pickup ions at several positions (x in Martian radii) downstream for two ion populations (a) and (b) (from Luhmann, 1990).*

Table 6 summarizes our estimations of the ENA fluxes in the Martian environment.

Table 6. ENAs in the Martian plasma environment [*Barabash et al.*, 1995a]

Region	Ion population	Energy, keV	Flux, $(cm^2\ s\ sr\ keV)^{-1}$
Outside the bow shock	Solar wind	1 - 5	10^6 - 10^7
Magnetosheath	Shocked solar wind	0.2 - 0.4	10^5 - 10^6
Inside the magnetosphere	Energized planetary ions	0.001 - 0.1 1 - 10	10^5 10^3
	Energetic (> 10 keV) ions	10 - 30 30 - 50	< 5 < 0.01 - 0.1
Day side LENA albedo [a]		0.01 - 1	10^2 - 10^4 cm^2 s eV
Phobos torus	Solar wind	1 - 5	10^4 - 10^6 (?)

[a] *Luhmann and Kozyra*, 1991

A New Component in Space Environments

We have reviewed briefly the generation mechanisms and basic properties of the energetic neutrals resulting from the interaction between a hot plasma and a cold background gas via the CE process. The expected ENA fluxes are low, but they can be found almost everywhere within our Solar system because almost everywhere the plasma is immersed in a neutral background of various extent of density. As discussed above the ENAs possess a number of specific properties which differ them significantly from energetic ions and electrons. From this point of view one could say that the ENAs represent a specific component within the space environments. Yet, totally unexplored! The most important motivation to study this component is, of course, the possibility to image remote plasmas, in particularly those consisting of

protons. In this way, the ENAs provide a new window on plasmas around us which has not yet been opened. Discoveries awaiting may become as dramatic as the first results of γ - ray astronomy, or the first images of the sky in extreme UV light.

ENAs can be used not only to image plasma but also dense neutral structures immersed in hot plasmas, for example the Titan exosphere, artificial gas releases in the Earth's magnetosphere, and comets .

High ENA fluxes can be generated in the interaction region between the solar wind and nonmagnetic planets or in the region of particle precipitation in the planetary magnetospheres. Thus studying ENAs is important in understanding these processes.

ENAs are of importance in some aspects of general plasma dynamics because every ENA carries away a certain momentum from the plasma. In some regions, the CE process and, consequently, ENAs are entirely responsible for an effective destruction of plasma structures. An example is the ring current decay in the Earth's magnetosphere.

The ENAs are not a stable component and can be rather easily re-ionized. The ionisation usually occurs away from the generation region; in such a way the ENAs effectively transport charged particles perpendicular to the magnetic field, which would otherwise be impossible. Typical examples are the low altitude temporal radiation belts and ENAs in auroras.

So, there are many reasons to study ENAs and there will come a time when it is accepted by the broad scientific community. To the question "How long?" raised by Hsieh and Curtis in 1988 (Figure 14), we would like to answer "Now is the right time!"

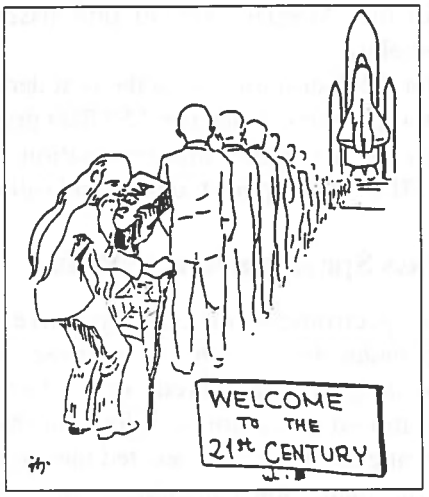

Figure 14. *How long? (from Hsieh and Curtis, 1988a)*

Measurement Techniques

Introduction

Studying the two main plasma components, ions and electrons, by traditional instruments is important for understanding local plasma processes, while studying the ENAs is essential for understanding global plasma configurations and plasma - neutral interactions. In other words, traditional particle measurements provide information about the behaviour of plasma as a part of a system, while ENA measurements shed light on the behaviour of the system as a whole. Apparently, measurements of both charged particles and neutrals are needed for a comprehensive knowledge. Understanding this fact and the great potential of ENA imaging brought the idea of measuring ion and ENA components simultaneously with one instrument package. In particular, it is interesting for nonmagnetized planets such as Mars and Venus. This idea was proposed first in 1989 by R. Lundin for the instrument ASPERA-C on the Mars 96 mission. Later on, this instrument has evolved into the PIPPI ENA imager for the Astrid mission. A prototype for ASPERA-C was the ion mass spectrometer ASPERA flown on the PHOBOS spacecraft to Mars. Successful realisation of this experiment provided a unique data set on the near Mars plasma, its composition and general morphology. These measurements have revealed the importance of the neutral component for the Mars - solar wind interaction process and are the basis for the "Martian" part of this dissertation. A description of the ASPERA instrument is given below.

The ENA imager PIPPI for the Astrid mission is the first dedicated satellite-borne imaging instrument for energetic neutral particles. Since the ASTRID project proceeded extremely fast and no detailed publications on the PIPPI instrumentation were made, we give here a comprehensive report on the PIPPI development, design and calibration.

Plasma Experiment. Mass Spectrometer ASPERA

The ASPERA ion mass spectrometer measures positive ions in the energy range 1 eV/charge - 23 keV /charge [*Lundin et al.*, 1989b]. It comprises a stacked toroidal electrostatic analyzer (Figure 15), placed in front of a curved cross - field mass analyzer (CFA). The emerging CFA beam is split in two parts, going to low and high mass resolution detectors respectively. The former, utilizing single CEMs, denoted the moment sensors, have a sufficient mass resolution to resolve the major ion constituents (H^+, He^{++}, He^+, O^+). The latter, consisting of a Z-type MCP assembly, the mass sensor, have a mass resolution that enables separation of minor constituents (e. g. molecular ions species). Each of the 10 moment sensors has a field-of-view about 5° × 36°, altogether covering the 360° in the plane perpendicular to the scanning plane. The entire sensor head is mounted on a scanning platform which makes one 180° scan in about 2 min, providing a full 4π coverage. However, due to the spacecraft shadow some part (8%) of the unit sphere is obstructed, but that is taken into account in the on-board data processing. Two mass sensors have 5° × 72° fields-of-view in the sunward and anti-sunward directions.

In the ASPERA instrument both ions and electrons are measured. The electron spectrometer covers the energy range 1 eV - 50 keV. It consists of a toroidal electrostatic analyzer and a Z-type MCP assembly with 6 sector anodes as a sensor. Every anode sector provides an angle of acceptance 5° × 90°, i.e., there is an overlapping of about 30° between sensors.

The sensor unit is contained in vacuum during the ground storage and launch phase to protect the detectors, in particular, the MCPs from contamination before launch. Once

evacuated, the sensor cover can only be opened in vacuum, after passing over a release mechanism during the first motor scan.

The -12 V pre-acceleration voltage is used to measure very low energy ionospheric ions. Cold plasma measurements are important near Mars and Phobos at the closest approach for studying the ionospheric plasma. In the cold plasma mode the increased energy resolution (total energy range 0.5 - 500 eV) is utilized to enable the separation between atomic and molecular species.

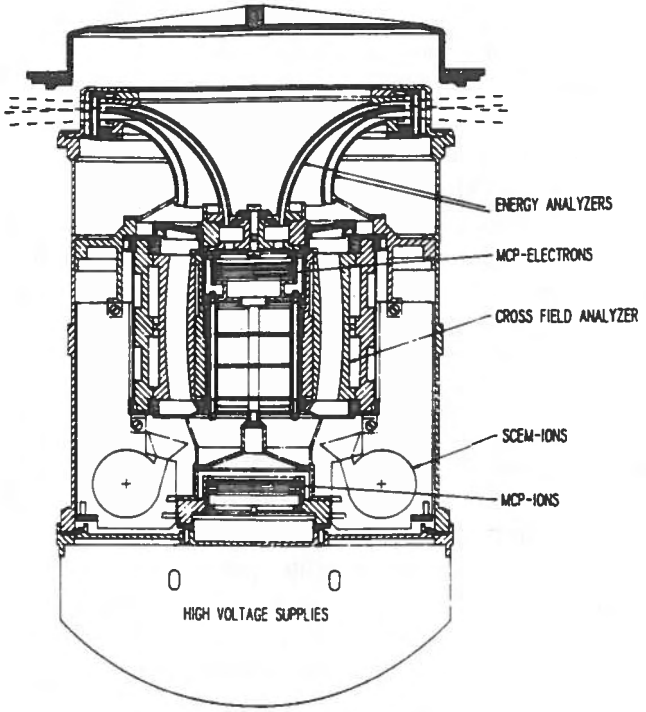

Figure 15. *Cross section of the ASPERA spectrometer unit.*

The magnetic deflection system in the CFA represents a novel approach in closing the intrinsic field by the magnets. Since no yoke is used, only magnetic shielding by high-μ metal is required. The system gives a very low stray field of about 1 nT at 1 m distance.

The instrument has its own solar panel which provides 30% of the required power at Mars. A summary of the ASPERA spectrometer characteristics is given in Table 7.

Table 7. The ASPERA Spectrometer Characteristics

Ions	
Energy range	1 eV/Q - 23 keV/Q
Energy resolution	10%
Field-of-view per sensor	5° × 36°
Geometrical factor. Moment sensor	3.15×10^{-5} cm^2sr
Electrons	
Energy range	1 eV - 50 keV
Energy resolution	8 %
Field-of-view per sensor	5° × 90°
Geometrical factor (@ 10 keV)	5.03×10^{-5} cm^2sr

The ASPERA data processing unit (DPU) is built around a Texas 9989 16 bit CPU and 16 kB RAM memory. For reliability reasons the DPU has two redundant CPUs and RAM memories. With one CPU and one RAM memory operating, the redundant CPU and RAM memory is powered off. Bootstrap loading and switching of the CPU and the RAM are controlled by " watch-dog" logic. The "flight program" is loaded from a 4kB PROM. Settings updated by commands are stored in the RAM which is powered by a battery when the main power is off. To reduce the data rate, onboard compression is performed by calculations of the first three moments of the distribution function for every specific mass species. The density, bulk velocity and the pressure tensor are calculated with high temporal resolution (of the order of tens of seconds). Spectral information for electrons and ions is also obtained for up to six directions, but at a lower rate (of the order of minutes).

The Phobos spacecraft was launched on July 12, 1988 and was injected into a highly elliptical equatorial orbit around Mars on January 29, 1989 (initial pericentre 870 km). It was subsequently transferred, on February 18, 1989, to a nearly circular orbit, close to that of the Phobos moon, orbiting at an average radius of 9600 km. The spacecraft remained on this orbit until the end of the mission on March 27, 1989. A more detailed description of the Phobos mission can be found in *Sagdeev and Zakharov* [1989]. All the important plasma domains of the Martian magnetosphere, the bow shock, magnetosheath, magnetosphere and plasma sheet were being crossed during the mission (see Figure 2). The ASPERA instrument operated satisfactorily near Mars. However, two malfunctions occurred. The scanner did not operate in a stable manner and the instrument was, for most of the time, set to the nonscanning mode. The full 4π coverage was provided by the spacecraft spin. Later, as a result of a high-voltage bias supply control malfunctioning, the detectors with even numbers were turned off, and the full coverage was provided by a complete satellite spin rather then half a spin. Thus due to an intrinsic redundancy and a suitable spacecraft attitude both errors were corrected and an exciting data set was obtained. To date, some 37 publications based on the ASPERA data have been made. Taking into account the very limited amount of data (about 15 MB) the experiment must be considered as a great success.

Neutral Particle Experiment. ENA Imager PIPPI

ENA Instrumentation. Heritage

Since the PIPPI ENA imager was the first dedicated neutral particle imager ever flown on a satellite in the Earth magnetosphere, before discussing it in detail we review the heritage of the HENA / LENA experiments to put PIPPI in the context of existing and previous instruments.

All earlier HENA measurements were made by SSDs for energetic charged particle detection because SSDs are sensitive to both ions and HENA [*Hovestadt and Scholer,* 1976; *Krimigis et al.,* 1975; *Roelof et al.,* 1985; *Kirsch et al.,* 1981a, 1981b]. However, angular resolution was rather limited. Only the Medium Energy Particle Instrument (MEPI) on ISEE 1 [*Williams et al.,* 1978], mounted on a scanning platform, was able to provide a complete scan of the sky by the spacecraft spin. These measurements were utilized to get the first HENA image of the Earth's ring current [*Roelof,* 1987]. The aforementioned experiments did not have any charged particle rejection system and HENA identification was based on directional information only when measurements were performed in the absence of significant charged particle fluxes, for example in interplanetary space during quiet solar conditions. Nowadays, advanced instruments for energetic charged particle measurements usually have a HENA channel, for example the IMS-HI experiment on CRESS and HEP on GEOTAIL [*Voss et al.,* 1993; *Doke et al.,* 1994].

The basic problem in LENA measurements is an ever-present high flux of UV photons (> 10^8 $cm^{-2}s^{-1}sr^{-1}$). The photons affect the sensors and result in a high detector background, which is unacceptable for low flux LENA measurements. So far only three experiments have been performed to measure LENA in space. *Bernstein et al.* [1969] used a 2 $\mu g/cm^2$ carbon foil to convert incoming LENAs into ions which were then analysed by a conventional electrostatic analyzer. This experiment was carried out on a sounding rocket as mentioned above [*Wax et al.*, 1970]. *Witte et al.* [1992] utilized a converting surface to perform imaging of interstellar neutrals onboard the Ulysses spacecraft. The principle of this experiment is elegant and simple. After traversing the electrostatic deflector / collimator, LENAs with an energy of 10 - 50 eV hit a surface covered by a material (LiF) with high secondary ion yield and high UV absorption properties. The secondary ions generated are detected by a negatively biased CEM, which is thus not sensitive to the secondary electrons produced by the LENAs and UV photons. Since the secondary ion yield for UV photons is much less than that for particles, an effective suppression of the UV background is achieved. The LiF coating is not stable and degrades in space. In order to restore the coating in flight a tiny furnace, filled with LiF, is used. An excellent performance (to our knowledge) led to the first direct measurements of interstellar neutrals. Note that the instrument was even able to detect ENAs originated in the Jovian magnetosphere [*Witte at al.*, 1993]. To complete our brief review of the LENA experiments we mention a rather unusual instrument using rotating slotted disks to detect fast atoms with velocities up to 500 km/s (1.3 keV protons) [*Moore and Opal*, 1975]. Surprisingly, the instrument prototype, flown at an altitude of 300 km in the daytime on an unguided Superchief rocket, functioned well and even survived recovery impact, despite a considerable amount of mechanical parts (some parts rotate at 44 000 rpm). The observed count rate was less than 1 per sec, "slightly more than the dark count rate on the ground" [*Moore and Opal*, 1975]. Table 8 gives a summary of HENA/LENA experiments flown up to now.

At present, two ENA instruments are under development, the Ion Neutral Camera INCA for the Cassini mission [*Cheng et al.*, 1993] and the Imaging Spectrometer for ENA ISENA on the Argentinean satellite SAC-B [*Orsini et al.*, 1992]. The energetic particle spectrometer SEPS to be flown on the despun platform of the ISTP POLAR spacecraft will be able to image ENA only over the polar caps where the charged particle background is very low. The instrument does not have a deflection system [*Voss et al.*, 1993].

SAC-B is a three-axis stabilized satellite to be launched into a 500-km 38° inclination orbit in 1996. ISENA will view in a fixed antisunward direction and is supposed to perform ring current imaging from beneath in the energy range 5 - 200 keV within 60° × 8°. It utilizes TOF analyses to determine the velocity of the incoming particles. The TOF section follows behind an electrostatic deflection system which also acts as a collimator. The start foil of the TOF section is used to reduce the UV photon flux and, in fact, define the energy threshold. The stop signal is produced by a SSD. The angular resolution is provided by a coded aperture followed by a MCP with a positive-sensitive anode [*Orsini et al.*, 1992].

The INCA instrument is designed to measure HENAs in the energy range 20 - 500 keV generated in the Saturnian magnetosphere. The electrostatic deflector determining the 90° × 120° field of view is followed by a TOF section, similar to the ISENA instrument, but the stop signal is produced by another foil. The direction is determined by a large MCP with a positive-sensitive anode. The ENA mass evaluation is made by pulse height distribution (PHD) analysis of the secondary electrons emitted by the foil in front of the MCP [*Mitchell et al.*, 1993].

No LENA instruments have so far been approved for new missions. However, very intensive development work is going on. D. McComas and colleagues at Los Alamos are working on the next generation of instruments making use of the LENA conversion into charged particles in very thin (tens Å) carbon foils and the subsequent analysis of the emerging ions with an electrostatic analyzer [*McComas et al.*, 1994; *Funsten et al.*, 1992].

Table 8. HENA / LENA flown experiments

Mission / Experiment	Deflection system	Measurement technique (Typical energies)	Comment
Sounding rocket [a]	Electrostatic	Conversion of LENA into ions in a thin carbon foil (1 - 25 keV)	Too high detected flux Spurious result
Sounding rocket / SDVS [b]	Electrostatic	Slotted disk velocity selector (< 1.3 keV)	Successful test of the prototype
IMP 7/8 / EPE [c]	Broom magnet only for electrons	SSD (20 -100 keV)	Unambiguous HENA detection
ISEE 1 / MEPI [d]	No	SSD (~50 keV)	First HENA image of the storm-time ring current
Voyager 1 / LECP [e]	No	SSD (40 -140 keV)	Possible detection of HENAs from the Saturnian and Jovian magnetospheres
Ulysses / GAS [f]	Electrostatic	Conversion of LENAs into secondary ions on a LiF surface (30 - 80 eV)	Observation of the interstellar neutrals
CRRES / IMS-HI [g]	Broom magnet	SSD (40 -150 keV)	HENA detection at low altitudes (600 km)
Geotail / HET-LD [h]	Electrostatic	SSD + TOF section (10 -100 keV)	ENA detection at the front side magnetopause and near the moon in the downstream solar wind
Astrid / PIPPI	Electrostatic	SSD (13 -140 keV) Conversion of LENAs into secondary ions on a graphite surface (0.1 - 70 keV)	ENA images of ion injections to the ring current at low altitudes

[a] *Bernstein et al.*, 1969; *Wax et al.*, 1970
[b] *Moore and Opal*, 1975
[c] *Roelof et al*, 1985
[d] *Williams et al.*, 1978; *Roelof*, 1987
[e] *Kirsch et al.*, 1981a; 1981b
[f] *Witte et al.*, 1992
[g] *Voss et al.*, 1993
[h] *Wilken et al.*, 1995

Another approach uses a low work function surface (monocrystalline tungsten coated with a thin layer of Cs) to convert LENAs to negative ions. The LENAs emerging from the electrostatic deflector-collimator hit the surface at a grazing angle (~20°). The negative ions produced maintain the same energy and angular distribution and can be analysed with an electrostatic analyzer followed by a TOF section [*Ghielmetti et al.*, 1994]. The proposed instrument utilizing this technique will be able to detect LENA in the energy range 10 eV - 300 eV.

A totally new approach in the LENA detection technique was suggested by *Gruntman* [1991]. As we mentioned, the main problem to be overcome in the LENA instrumentation is an effective suppression of the UV radiation. Traditionally, this is done by removing the LENAs from the UV flux by means of different conversion techniques. Instead of that, it has been suggested to remove the UV radiation from the LENA flux with a submicron transmission grating. A filtering structure with a typical 200 nm period (100 nm bars and 100 nm slits) substantially reduces and polarizes the UV light in the range 30 nm - 150 nm. The second structure placed in the beam with its axis of polarization oriented at a right angle to the first one attenuates the UV light significantly, although both structures allow about 1% LENA to pass. The expected Lyman-α line attenuation in such a system is 10^8 [*Scime et al.*, 1994]. LENAs thus filtered out can be analysed either directly by a MCP or converted to ions by one of the techniques mentioned above.

The Astrid Mission

Very small satellites with a total mass less than 50 kg, i.e., microsatellites, have been used for technology tests and amateur radio for almost two decades. They have not, in general, been considered useful for space science research. However, the Swedish Space Corporation (SSC) proposed to the Swedish space science community to fill the time gap between "major" flight opportunities by trying microsatellites dedicated to scientific objectives. In this way the Astrid project was launched.

The Astrid microsatellite [*Grahn and Rathsman*, 1995] was built quickly and at low cost ($1.4 M including launch) at SSC with the "small team approach" first used in the Freja project [*Grahn*, 1993]. It was launched into a 1000 km polar orbit on January 24, 1995 from the Russian cosmodrom Plesetsk as a piggyback passenger on a Kosmos-3M rocket. Astrid carried an ENA imager PIPPI, an electron spectrometer EMIL and two UV photometers MIO-1,2 (Figure 16). The total mass of the payload is 4.08 kg.

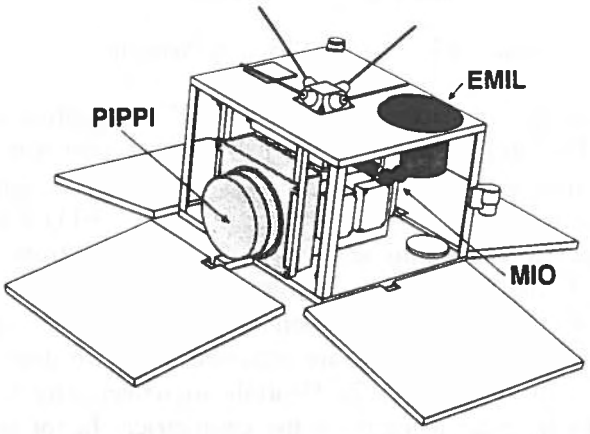

Figure 16. *The microsatellite Astrid with the payload*

Astrid is a 10 times scaled-down version of the Swedish satellite Freja which was launched on October 6, 1992 and is still operational. Astrid weights 27 kg. In the launch configuration

the dimensions of the satellite are approximately 0.45 × 0.45 × 0.29 m. The satellite is spin-stabilized with the spin axis pointing towards the Sun. A typical spin period is 3 - 4 s. The power is delivered by four solar panels which can provide up to 45 W while the total power consumption is only 22 W.

There are two downlinks; an S-band with 128 kbps and 400/450 MHz with 8 kbps. The former is received at the Freja control center at the Swedish Space Corporation's ground station ESRANGE (68°N 21°E). The latter is received at a small secondary ground station. This specially designed station uses standard amateur satellite equipment and is capable of automatic unattended reception and storage of telemetry as well as automatic transmission of commands prepared in advance. Commanding via the 4800 kbps uplink can be done from both stations. 8 MB onboard memory is available to store and play back the scientific data.

General Concept of the ENA Imager PIPPI

The PIPPI development, design and manufacturing were conducted under strong pressure from four factors; shortage of time, shortage of manpower, shortage of funds and very limited spacecraft resources. To illustrate our timetable we recall that the first pieces of hardware related to the neutral particle imager (NPI) of the ASPERA-C experiment for the Mars 96 mission were installed in vacuum on April 27, 1993. That was a check of the coating for the LENA sensor head. On August 28, 1993 the Swedish Space Corporation first proposed the ASTRID project to the scientific community and asked for a suitable payload which could meet the microsatellite requirements and still produce interesting scientific data. That was the birth of PIPPI. On September 23, 1994 the instrument was delivered to the Swedish Space Corporation. Thus the instrument design and manufacturing took only 13 months!

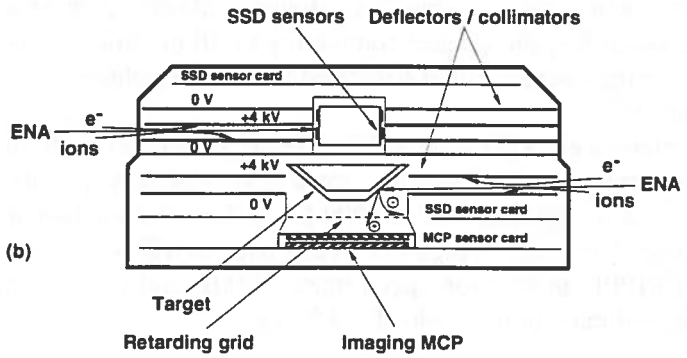

Figure 17. *The PIPPI sensor head schematics.*

First of all we describe the main principles of the PIPPI operation and then discuss in detail the particular units. The PIPPI ENA imager consists of two sensor heads, PIPPI-SSD, PIPPI-MCP, and an electronics block. The former is dedicated to measuring HENAs in the energy range 13 - 140 keV using SSDs. The latter measures ~ 0.1 - 70 keV LENAs by means of the conversion of primary neutrals into secondary particles (electrons and ions) followed by detection with a MCP. Mechanically the instrument is one unit. The schematics of the sensor head is given in Figure 17 and the cross section of the instrument in Figure 18.

In the PIPPI-SSD charged particles are removed by a two deck electrostatic deflection system consisting of 4 disks (Figure 17). Neutrals are detected by 14 Si solid state detectors located on two decks in order to increase the geometrical factor of each sensor. 8 plastic spokes between each pair of the disks divide the 2π field of view into 8 collimators with an aperture 5° × 30° each. The upper and lower levels of the sensors are turned with respect to each other by 22.5° to provide an angular resolution of ≈25°. For one 180° turn around an axis in the plane of the instrument, in practice for half a satellite spin period, almost the entire 4π

space is covered by all sensors. The elevation angular resolution depends on the spacecraft spin rate and accumulation time. It is 3.8° for 20 rpm and 31.25 ms. Two sensors pointing towards the Sun are obscured to avoid direct solar light from reaching them. One of these detectors is completely blocked and is used to estimate the electronics noise. The other is shielded by an aluminium foil to detect only particles with energies above 140 keV. It has a separate counter and monitors the energetic particles which can pass the deflector system. The 16 detectors are sampled simultaneously. Each pulse from 15 SSD detectors (except the background sensor with a foil) is discriminated in 8 levels to give the energy spectrum. The direction is given by the sensor number. The direction - energy matrix of 15 × 8 elements are accumulated during 31.25 ms. When the HV for the electrostatic deflector is off, the PIPPI-SSD measures ions and electrons as an ordinary energetic particle detector.

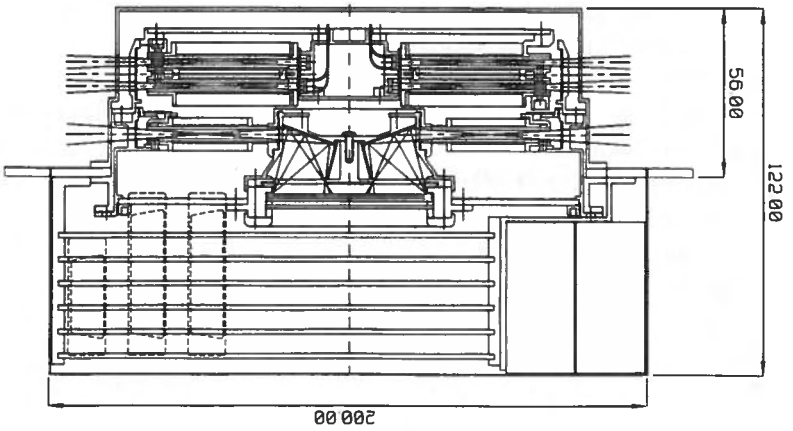

Figure 18. *The PIPPI instrument cross section .*

The PIPPI-MCP deflection system includes only one level and due to the higher gap between the deflector plates removes charged particles only up to 70 keV. The space between the disks is divided into 32 sectors by plastic spokes forming 32 collimators with an aperture of 9°× 18° each. The sector pointing towards the Sun is blocked. Neutrals passing through the deflection system hit a 32 sided cone target with an angle of incidence of ≈70° and produce secondary particles, both electrons and ions. These particles are detected by a MCP with 32 anodes. The signal from the MCP gives the direction of the primary incoming neutral. By varying the potential applied to a grid in front of the MCP one may select particle species or separate the secondary particles by energy. The MCP can also operate in either electron mode with positive bias or in ion mode with negative bias. In order to improve the angular resolution and collimate the secondary particles, 32 separating walls are attached to the target forming a star-like structure. Like the PIPPI-SSD, the PIPPI-MCP covers almost 4π in half a satellite spin period and produces an image of the LENA distribution in the form of azimuth × elevation matrix. The direction vector of 32 elements is read out once per 31.25 ms. A summary of the instrument characteristics is given in Table 9.

The experiment does not have a DPU. Data accumulation, command decoding and execution, high voltage control, mode switching (2 modes), and monitoring the analog channels are performed by hardware. The digital logic is built around a programmable logic circuits ACTEL. The absence of a DPU makes the instrument much simpler, lighter, and smaller. The development time becomes substantially reduced. Moreover, the high bit rate downlink of 128 kbps permits handling of the data dump without a DPU.

Besides PIPPI, there are two supporting instruments onboard ASTRID. Those are the electron spectrometer EMIL and the UV photometers MIO-1 and MIO-2. The former performs electron measurements in the energy range 0.1 - 40 keV from 6 directions approximately in the plane of the magnetic field lines, i.e., over all pitch-angles. It supports the ENA measurements in terms of evaluating of the local plasma conditions.

Table 9. The PIPPI ENA Imager Characteristics

PIPPI-SSD	
Energy range (neutrals)	13 - 140 keV
Energy resolution	8 steps
Angular resolution (FWHM) [1]	2.5° × 25°
Aperture per sensor	5° × 30°
Full field of view	5° × 322°
Azimuthal sectors	16
	(2 background sectors)
Geometrical factor	3.5×10^{-2} cm^{2}sr
Geometrical factor per sector	2.5×10^{-3} cm^{2}sr
PIPPI-MCP	
Energy range	~0.1 - 70 keV
Energy resolution	No
Angular resolution (FWHM) [1]	4.6° × 11.5°
Aperture per sensor	9° × 18°
Full field of view	9° × 344°
Azimuthal sectors	32
	(1 background sector)
Geometrical factor	7.8×10^{-2} cm^{2}sr
Geometrical factor per sector	2.5×10^{-3} cm^{2}sr
TM budget	78 kbps (high mode)
	4.9 kbps (low mode)
Power	4.0 W
Mass	3.13 kg

[1] elevation angular resolution also depends of the spacecraft spin rate and sampling time. It is 3.8° @ 20 rpm and 31.25 ms.

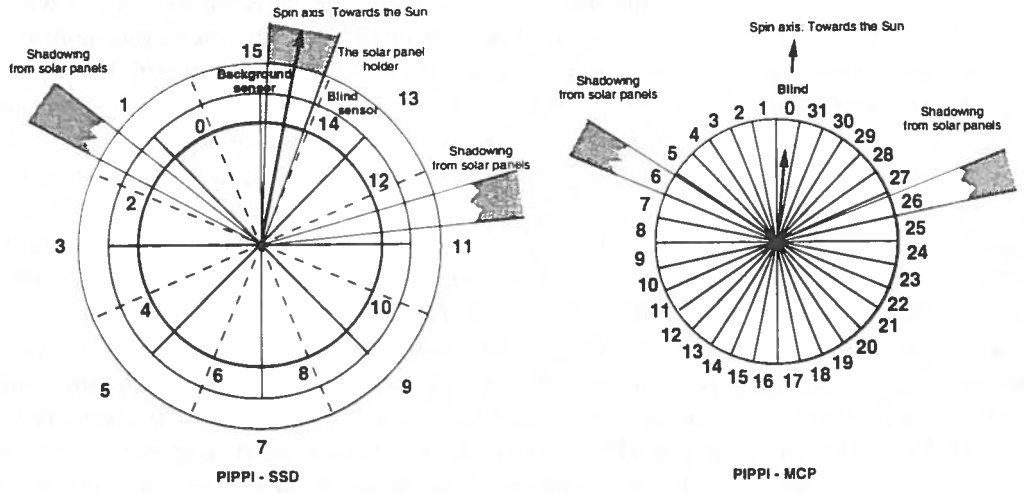

Figure 19. *Numbering of the PIPPI-SSD and PIPPI-MCP sectors.*

The spin-scanning UV photometer MIO-1 measures the Lyman-α line intensity to provide the global UV background important for evaluation of the PIPPI-MCP measurements. MIO-2 with a 130 - 160 nm pass band detects the UV emissions from the auroral region (for more details,

see *Norberg et al.*, 1995]. The positions of all three instruments on the spacecraft platform are shown in Figure 16. All electrical interfaces for EMIL and MIO are made via PIPPI.

It is impossible to avoid blocking the PIPPI field of view by the Astrid solar panels. In order to minimize this effect, the solar panels are tilted 10° from the plane perpendicular to the spin axis. That results in a 10° shadowing of the SSD sectors 1, 2, 11, and 12. The sector numbering, the solar panel shadowing and the position of the background sectors are given in Figure 19. The outward deck SSD sectors are marked by solid lines and the inward deck sectors by dashed lines.

The mechanical design was done in such a way as to prevent any blocking of the MCP field of view by the spacecraft surface at the corners. The instrument extends out to its very maximum, but the margin was still only 1 mm. Since the spacecraft is covered by a multilayer insulation (MLI), MLI swelling in vacuum could result in a small shadowing of the PIPPI-MCP field of view in sectors 11, 12, 20, and 21.

Operation of the ENA Imager PIPPI

The microsatellite ASTRID was launched on January 24, 1995 at 03:54:22UT from the Russian cosmodrom Plesetsk, using a piggyback arrangement on a Kosmos-3M rocket. The orbit was almost circular (966 km × 1027 km) with an 83° inclination and 105 min period. Initially, the orbit was located in the dawn - dusk sectors with no eclipses. The payload was operational until March 1, 1995, when the onboard DC / DC converter powering PIPPI and, hence, EMIL and MIO ceased to work. Due to limited spacecraft resources and the technological character of the mission, there were no redundant systems and the malfunction was fatal for the payload.

Data taking was performed mainly from ESRANGE and in real time. However, during the later phases of the mission some data (24 min) were collected in eclipse at low latitudes. The PIPPI instrument was operational from January 24, 1995 to February 28, 1995 on 57 orbits and produced 358 MB of data (10 hours 10 min). During the first week of the mission the high voltages were off to enable satellite outgassing and the PIPPI-SSD head measured both HENA and ions. These data will be used for calibration purposes and for the analysis of 3D energetic charged particle distributions in the auroral zone. Note that over the polar part of the Astrid orbit, for magnetic latitudes greater than 70°, the charged particle background is very low and data collected there can be used to image ENAs even if the deflection system is off. Altogether approximately 8 hours (78%) of the PIPPI-SSD and 5 hours (49%) of the PIPPI-MCP data were obtained with the deflection system operating. Real time data covered approximately 50° to 90° magnetic latitudes in the dusk sector between 15 - 18 hours MLT.

The PIPPI sensor heads are an almost exact replica of the Neutral Particle Imager for the ASPERA-C experiment in the Mars-96 project. In order to decrease the energy threshold for the HENA measurements in the Martian environment the SSD sensors do not have any protective coverings like foils or metal deposits. This makes the PIPPI-SSD rather sensitive to photons. The instrument was designed to operate at solar angles less than a few degrees to avoid direct light from coming into the apertures, but during the Astrid mission the solar angle was never less than 6° and ranged, basically, between 10° - 25°. This resulted in a contamination of the SSD sensors by photons reflected from the microsatellite structures (the solar panels and the PIPPI mounting surface). However, the contamination is very limited over elevation and easily recognised. Photons coming from the Earth's surface or reflected by clouds in the atmosphere caused strong disturbances in certain directions, but they occupied a solid angle which can be easily identified from pure geometrical considerations.

The MCP deflection system did not work stably at high (> 2.5 kV) voltages. In order to avoid discharges the working level was set to 2.0 kV instead of 4 kV. The PIPPI-SSD deflector was set to 3.2 kV instead of 4 kV. We did not have time to increase it to the nominal values before the malfunctioning of the DC/DC converter. The 3.2 kV deflection system voltage

corresponds to a 110 keV cut-off energy. Due to the short period of operation only very limited in-flight instrumental tests were carried out with the PIPPI-MCP. For the entire mission it operated in ion mode with a bias of -2.6 kV. The MCP retarding grid was grounded. Another unfortunate malfunction of the PIPPI-MCP was a failure of one of 4 preamplifiers (8 channels). This resulted in the loss of almost the entire anti-sunward direction. The problem seems to be related to poor quality of these chips.

The HENA sensor head operated rather well and we are quite pleased with the PIPPI results. So far a very limited part of the data set has been analysed but it has already revealed very interesting and unusual features of the ENAs and ENA imaging at low altitudes in the regions of the energetic particle precipitation. Moreover, the main objective of the ASTRID mission was a technological demonstration that microsatellites may be useful to provide "good science" at a modest price. This was clearly achieved. We have tested under space flight conditions several important components to be used in our next-generation ENA instruments and, most importantly, we have obtained a unique experience in development, design, and flight operation of an ENA instrument.

HENA Sensor Head. PIPPI-SSD

Now that we have described the general concept of the PIPPI instrument, we focus on individual components of the two sensor heads. The PIPPI-SSD consists of an electrostatic deflection system, SSDs, and sensor electronics. The digital TM electronics and high voltage supply control will not be discussed.

Deflection System

Particle detectors (SSDs, MCPs, CEMs) do not distinguish between ENAs and charged particles. Thus if the local charged particle environment represents a significant contamination to ENA flux measurements, it should be removed or greatly reduced. The purpose of the deflection system (deflector) is to remove charged particles from the flux coming into the ENA instrument and, hence, a deflector is a necessary component of any ENA instrument. Considering the usually rather low ENA flux constituents of space plasmas, an effective rejection is essential to reduce the background for ENA measurements. In developing the PIPPI instrument, we discovered that design and calibrations of the deflection system are quite challenging and not at all straightforward as it might seem at first glance.

The electrostatic deflector is an entirely new element and we lacked experience in designing such a system. Moreover, very limited literature on this subject is available. To our knowledge, only one experimental study of an electrostatic deflector has been published [*Keath et al.*, 1989]. *McEntire and Mitchell* [1989] gave some general ideas about charged particle rejection in ENA instruments. *Gruntman* [1994a] suggested a new type of deflector, an annular collimator, but gave, however, only theoretical estimations for the field of view and cut-off energy.

The simplest electrostatic deflector is a pair of parallel plates of length L, separation distance D, and having a voltage V between the plates. Such a system rejects all particles of charge q with energy less then the cut-off energy, E_c, which is given by the simple formula

$$E_c = q\,V\left(1+\left(\frac{L}{4D}\right)^2\right) \qquad (3)$$

The cut-off energy is proportional to $(1 + (L/D)^2)$. Thus it is desirable to have the ratio L/D as high as possible to get higher E_c. On the other hand, if the deflector determines the field of view of the instrument and, hence, its geometrical factor, the ratio L/D should be kept low,

because the geometrical factor is roughly proportional to D^2 / L for a fixed field of view in one direction. A compromise has to be found.

The PIPPI deflector plates are disks but the above formula with L equal to the difference between the outer and inner radii is still valid to give the minimum cut-off energy. Optimizing the PIPPI-SSD deflector design we have chosen L = 47 mm and D = 2 mm, i.e., the deflector factor, $DF = 1 + (L / (4D))^2$ is 35.5. Since in the PIPPI design the deflector collimates the incoming beam in both azimuth and elevation, plastic spokes are introduced into the gap between the disks. The field of view for one PIPPI-SSD sector is shown in Figure 20 in a section along the disks. The spokes and serrations on the internal disk surface that minimize forward scattering can be seen.

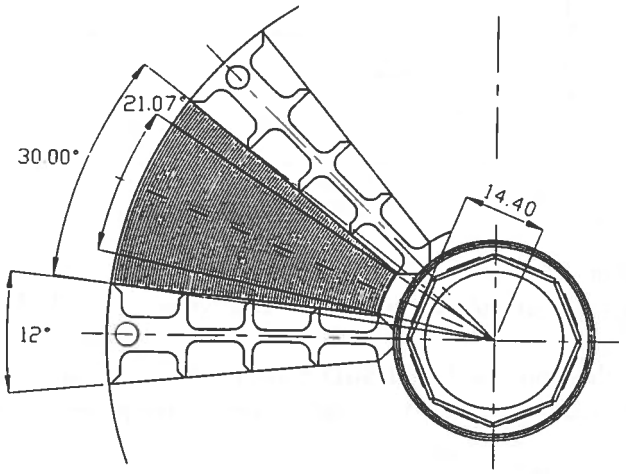

Figure 20. *The field of view for one PIPPI-SSD sector in a section along the disks. The spokes and serrations on the internal disk surfaces can be seen.*

The spoke material must satisfy several rather stringent conditions such as low outgassing, high dielectric strength and low opacity in a 2 mm thickness. It must be easily machined because the spokes have a very complicated shape. Finally, it must be reasonably priced (that is why we rejected Vespel). A plastic material used in Russian industry was selected and turned out to satisfy all requirements. To reduce forward scattering of the particles inside the deflector, the serrations are machined in the inner disk surfaces according to the design by *Keath et al.* [1989]. In addition the deflector surface is blackened by copper sulphide. The 2 mm gap (or 3 mm along the plastic spoke due to a special mechanical design) is very close to the critical limit for the 4 kV nominal potential difference. However, stable operation has been achieved for 4.3 kV during ground tests.

We have experimentally checked the formula (3) with the deflector in the flight configuration but with a CEM as a particle detector. The charge particle flux was simulated by an electron beam produced by the IRF electron source. For each beam energy, the dependence of the CEM response on the potential between the plates was obtained. The CEM response was given by integral counts for the +7° / -6° sweep through the beam. The potential V varied from 0 to 2000 V. The first potential when the CEM signal did not drop any further with increasing V was taken as the deflector potential providing the cut-off for the given beam energy. Figure 21 presents the dependence of the cut-off energy on the deflector potentials. There is a reasonable agreement with the theoretical dependence $E_C = DF \cdot V = 35.5\ V$.

Another important characteristic of the deflection system is the transmittance. We define the transmittance for the potential V as the ratio of the detector response for the potential V between the deflector plates to the detector response for zero potential difference. Determining

the transmittance for an ion beam is a rather complicated task, because any ion beam contains a certain percentage of ENAs from the CE process with the residual gas in the ion source chamber (see the section below). However, electron beams are free from this effect and the transmittance can be determined more easily.

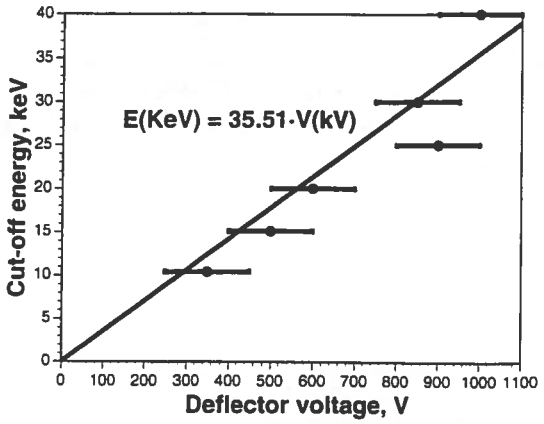

Figure 21. *Dependence of the cut-off energy on the PIPPI-SSD deflector potential. A reasonable agreement with the theoretical dependence $E_c = 35.5V$ can be found.*

During pre-flight calibrations the PIPPI-SSD deflector transmittance was found to be 4×10^{-4} for a 72 keV electron beam with 3.8 kV potential between the plates (Figure 22).

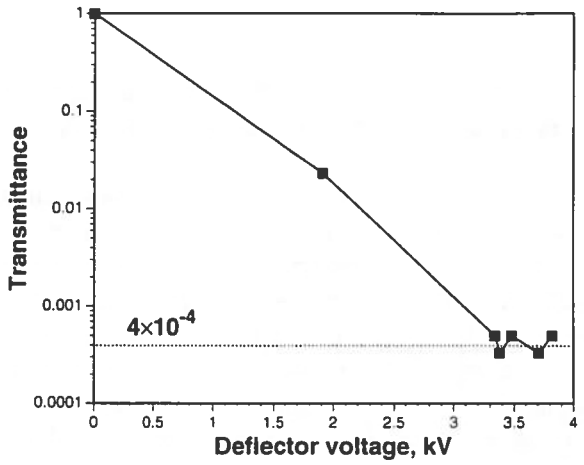

Figure 22. *The PIPPI-SSD deflector transmittance as a function of the potential between the deflector plates for 72 keV electrons.*

Let us compare this result with the transmittance for the similar deflection system of *Keath et al.* [1989]. Since there is a small difference in the geometry between the two deflection systems one has to compare the transmittances at different voltages between the plates but for the same charged particle beam energy. Obviously, $V_k = (DF_p / DF_k)\, V_p$ where V_p and V_k are the potential differences between the plates for the PIPPI-SSD and the design by *Keath et al.* [1989], and DF_p and DF_k are the corresponding deflector factors. *Keath et al.* [1989] measured a transmittance of 5×10^{-4} for a 75 keV electron beam with 8.7 kV potential between the plates corresponding to the 3.8 kV for the PIPPI instrument. The two transmittances are very close, confirming our calibrations.

Since the basic PIPPI design could not be drastically changed to lower the transmittance, we tried to improve this characteristic by introducing broom magnets in the PIPPI-SSD deflector. Several configurations, presented in Figure 23, were checked.

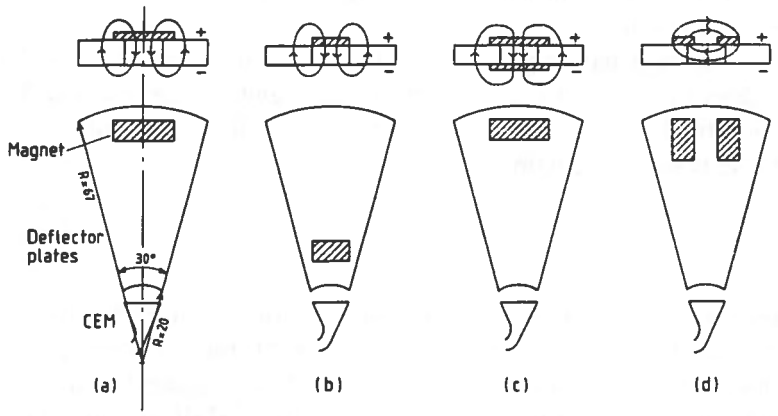

Figure 23. *Different configurations with broom magnets to improve the transmittance.*

Samarium-cobalt magnets with a magnetic field of 200 - 400 G were used. All transmittance tests were performed against electron beams in the energy range 10 keV - 50 keV, corresponding to electron Larmour radii of 1 - 2 cm in these magnetic field geometries. This is comparable with the typical size of the PIPPI-SSD deflector. Surprisingly, all configurations showed worse transmittances than the deflector without magnets. The best magnet position (Figure 23*b*) gave some 15 - 20 times higher transmittance than the basic configuration over the entire energy range. The reason for such a behaviour is not quite clear. One possible explanation is that the electron trajectories are bent into the plastic spokes by the magnetic field, causing charging effects. This results in an electric field redistribution inside the deflector leading to a higher transmittance. On the basis of these tests we decided not to introduce broom magnets into the PIPPI-SSD deflection system.

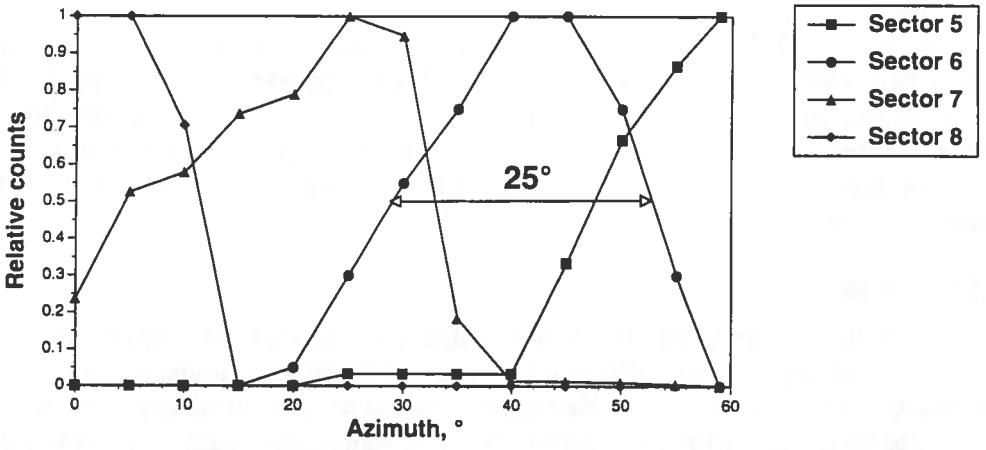

Figure 24. *PIPPI-SSD azimuthal response for sectors 5, 6, 7, and 8 according to Figure 19.*

During the PIPPI-SSD deflector calibrations with an electron beam of more than ten keV an interesting effect was noticed, a so-called electron "leakage". An intense flux of electrons with energy up to 50 eV "leaks" from the deflector while a beam of energetic electrons was on (ion beams were not checked) . This effect was found using a CEM as a particle detector with a retarding grid introduced between the deflector and the CEM funnel. A possible reason for

the electron leakage could be scattering of the primary beam inside the deflector and the production of secondary electrons from the plate surfaces by the energetic electrons of the beam. Due to the low energies involved the leakage is not of importance for the PIPPI-SSD and PIPPI-MCP performance but it has to be taken into account in the design of instruments for very low energy neutrals.

The angular responses have been checked in the elevation and azimuthal directions. The experimentally determined FWHM is 2.5° for elevation and 25° for azimuth. This corresponds well to the theoretical values calculated from the collimator geometry. The PIPPI-SSD azimuthal response is given in Figure 24.

SSDs

Partially depleted and ion implanted silicon detectors are used for the SSDs. A typical depletion depth is 300 μm and the front dead layer is 50 nm. Theoretical calculations give energy losses for such a dead layer of Si as 2 - 8 keV for incident protons of 4 - 100 keV [*Johansen*, 1990]. 300 μm of Si is a projected range for 6 MeV protons, 20 MeV He^{++} and 250 keV electrons. The total sensitive area is a trapezoid of 12 mm^2. The working area is 10.9 mm^2, slightly less than the sensitive area because the collimator design was changed after the SSDs had been manufactured. A nominal noise level at 20° C is 2.2 keV for the detector capacity of 5 pF. The detectors were manufactured by CANBERRA Semiconductor, Belgium.

The HUGIN circuit is utilised for preamplification. This is a VLSI chip containing ten charge sensitive preamplifiers. The chip is developed by the Center for Industrial Research in Oslo specifically for space applications. The noise level is 7 keV for a 20 pF detector at 20° C and should be even less for the 5 pF detector. Both the preamplifier and the detectors give a rather low noise at room temperatures. However, the noise level of the final assembly turned out to be 13 keV, caused by the stray capacitance, disturbances in the bias voltage, and imperfect shielding of the detector and preamplifier housing. This noise depends very weakly on temperature and is found to drop only by 9% for a temperature change from +20° C to -40° C. In view of this, we modified the initial PIPPI design and removed the passive radiator for cooling the SSDs. The temperature of the SSD housing and the HUGIN preamplifiers was -2° C ....+ 3° C during flight.

To compare the PIPPI-SSD noise level with other sensors we mention the result of *Johansen* [1990] who achieved a noise level of 5 keV with a FWHM of 2.5 keV. However, in this case a specifically designed detector and component housing, the AMPTEC 250 one channel preamplifier (the state-of-the art in low noise), and the 2 GΩ bias resistors (0.11 GΩ in our case) were used. Unfortunately, it was impossible to implement this design in the PIPPI-SSD sensor head with 16 detectors.

Sensor Electronics

In order to make the signal from the detector output acceptable for pulse height analysis, it is amplified in three stages by one NPN transistor and two operational amplifies. Since we did not have enough room to accommodate the required amount of operational amplifiers, the SSD electronics was designed as follows (Figure 25). The signal from each individual SSD is amplified by a charge-sensitive preamplifier, then by an NPN transistor stage followed by the first operational amplifier. At this point the signals from all 15 sensors (except the background sensor) are summed up and the sum goes to the final operational amplifier, being subsequently discriminated in 8 levels. In order to suppress noise, which would be rather high due to pile-up if the sum of signals were routed directly to the last operational amplifier, 14 switchers were introduced to open and lock the next to last amplifier outputs. The logical (+5 V) signal controlling the switchers is produced by each detector. When there is a pulse from a detector, the corresponding switcher is opened for < 0.5 μsec and the analog signal goes to the last

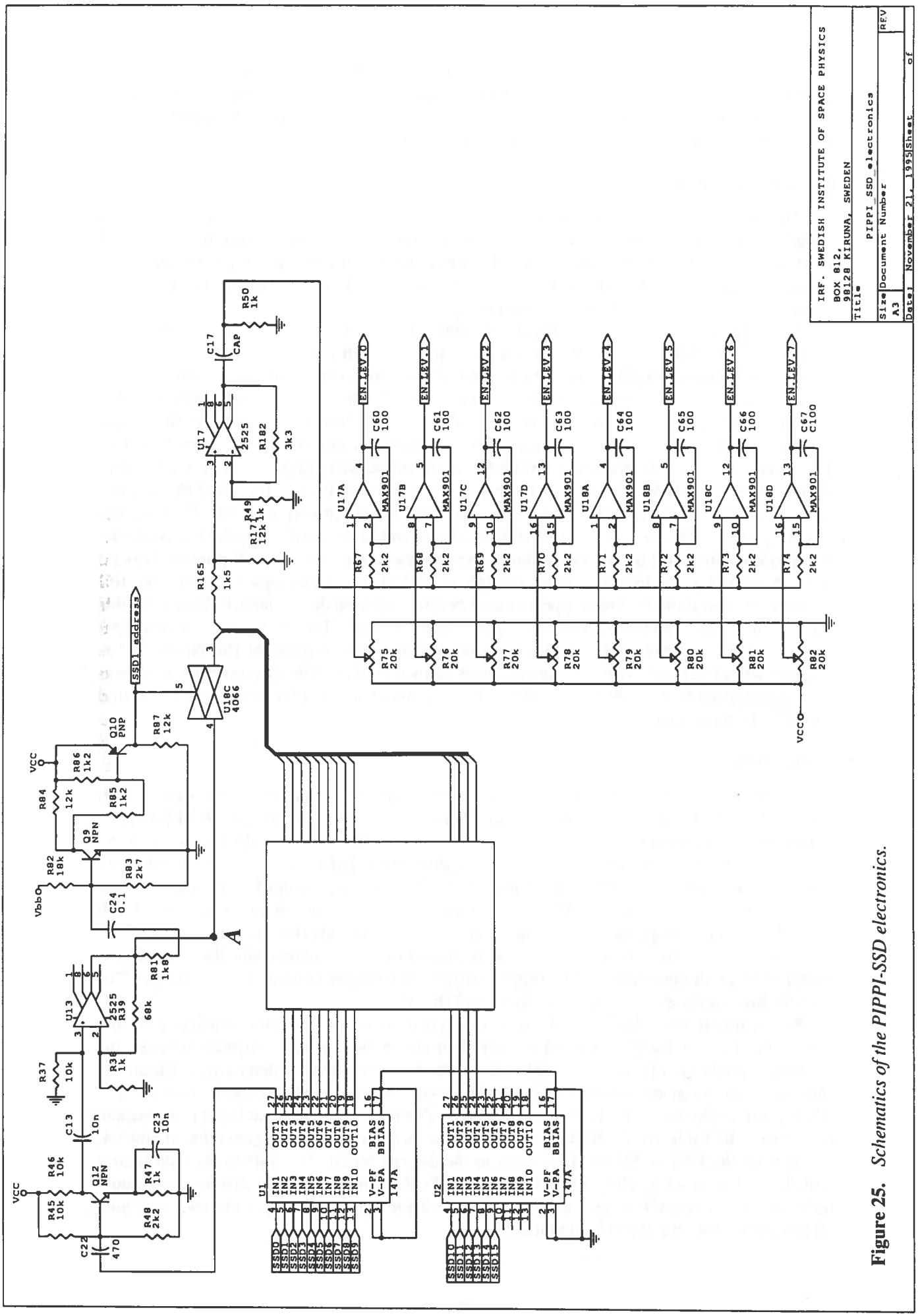

Figure 25. *Schematics of the PIPPI-SSD electronics.*

amplifier input. The controlling pulse is also used to define the address of the specific detector activated at that moment. After passing the last amplifier the signal is discriminated over 8 levels. Each pulse is counted and stored as a unit in the 15 × 8 (detector number × energy level) matrix which is accumulated in the 16 bit memory for 31.25 ms.

Background Sensors

Two sensors have been dedicated to monitor the background. Sensor 14 (Figure 19), a so-called blind sector, is identical with all others in terms of signal processing but is blocked mechanically by 3.5 mm of aluminium. The aperture for this sensor was simply not cut out in all mechanical parts within its field of view. This sensor is used to estimate the electronics noise level and background from very energetic particles.

The purpose of the so-called background sensor (sensor 15, Figure 19) is to monitor the background of particles (neutrals and charged particles) with energy > 140 keV. This is of importance because these particles can pass through the deflection system and contribute to the background signal. The aperture of sensor 15 is covered by an aluminium foil mounted on the cylinder wheel 2.5 mm in front of the SSD. We used the following criteria to define the thickness of this foil. First of all, it should be light-tight, because the sensor aperture is only 11° away from the solar direction. Secondly, it should be transparent for all particles with energy above 140 keV. The chosen thickness is the projected range for 140 keV protons, because protons have the lowest range for the same energy among all ions. To make the shielding light-tight two layers of the 0.6 μm aluminium foil are used. According to *Andersen and Ziegler* [1977], 1.2 μm of aluminium is the projected range for 140 keV protons. Ground tests showed that the two layers are enough to protect the sensor against light. The foil survived the vibration test but it appears that it became ruptured during launch. Data from this sensor show very intense spikes twice per spacecraft spin. This is typical for sun light contamination. Electronically, the background sensor is independent of the others. It has separate amplifiers, only one discriminator and its own counter. The discriminator level was set just above the noise level to pass all pulses from this sensor. In this sense, the background sensor is the most sensitive one.

Calibrations

To deliver the instrument in time we had to limit calibrations and tests to the most crucial ones and to do them in the simplest way. Thus we did not calibrate the PIPPI-SSD to determine its geometrical factor but used the values obtained by calculations with an assumption of 100% efficiency. The tests and calibrations of the deflector / collimator were mainly carried out using CEMs, rather than SSDs. We have also simplified the energy level calibrations by using a monoenergetic (conversion) electron source with an activity of 100 μCi. The source is prepared by evaporation of the Ba-133 nuclide (half-life 10.5 y) as a 5.08 mm spot on very thin Mylar. The spot is protected by acryl coating and the assembly is stretched in an aluminium ring. The supplier is Isotope Products Laboratory, Inc. (USA). The electron lines of the Ba-133 source are given in Table 10.

By means of pulse height analysis of the signals from the detector stimulated by the source, the Ba-133 energy lines can be identified and in such a way a relation between the incident particle energy and the amplitude of the detector signal is determined. Figure 26 illustrates the linear dependence of the signal level (channel number) taken from point *A* (Figure 25) on the energy of the incident electrons. The lines used in the calibration are marked by asterisks in Table 10. By feeding adjustable pulses from a test pulse generator to point *A*, one can set the PIPPI-SSD discriminators to the desired levels. To confirm the calibrations with Ba-133 we used another radioactive nuclide Tc-99. This provides an electron continuum up to 293 keV and can thus give another reference point. It is showed by a rhombus in Figure 26 and agrees with the Ba-133 calibrations.

Table 10. Electron lines of the Ba-133 source

Energy, keV	Intensity, % per decay
0 - 6	≈ 150
17.1	11.0
25 - 35	≈15
43.3	3.7
45.0	44.0
47.5	1.3
52.0	0.4
73.6	0.55
75.3*	6.8
78.0	0.12
79.8	1.7
124.6*	0.15
154.9*	0.02
187.24*	0.04
240.4*	0.34
266.9*	0.68
271.0*	0.62
275.2	0.2
297.2*	0.1
320.0*	1.3
347.9*	0.15
350.3	0.22
378.2	0.02

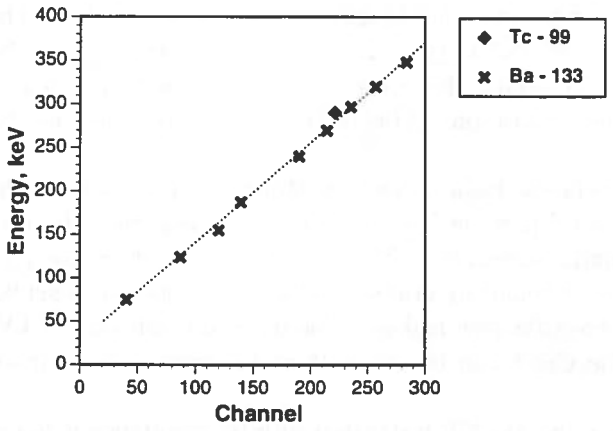

Figure 26. *Dependence of the SSD signal (channel number) taken from point A (Figure 25) on the energy of the incident electrons from the Ba-133 source. The solid rhombus shows a point obtained from Tc-99 calibrations.*

Theoretical energy levels are chosen to keep the energy resolution $\Delta E/E$ = 30% constant over all channels. They correspond to the electron energy levels because the electron energy loss in the SSD dead layer is very small (< 3%) for energies above 15 keV [*Johansen*, 1990].

The proton energy levels are recalculated knowing the proton losses in the dead layer. Table 11 gives the PIPPI-SSD energy channels.

Table 11. The PIPPI-SSD energy channels

Channel	Electrons, keV	Protons, keV
0	≈ 13 - 21	≈13 - 26
1	21 - 31	26 - 37
2	31 - 44	37 - 52
3	44 - 63	52 - 71
4	63 - 89	71 - 97
5	89 - 140	97 - 147
6	140 - 300	147 - 306
7	> 300	> 306

Neutral Component in Ion Beams

When carrying out calibrations of the PIPPI-SSD deflector with ions in the energy range 1 keV - 20 keV, it was noted that the transmittance never dropped below a few percent. It turned out that the reason for this is a neutral component which is ever-present in ion beams generated in any calibration facility. These neutrals result from charge - exchange between the beam ions and atoms from the residual gas. We used the Ar^+ ion beam because it is the one most readily produced, but the same is true for any ion species. One can easily see that for the energy range in question the ion beam always contains 1% - 5% of neutrals. A typical CE cross section for this energy range is > 10^{-15} cm^2 (we did not manage to find publications on CE cross section for Ar^+ on N_2 and O_2), the working pressure in the ion chamber was in our case of the order of 10^{-6} mbar, corresponding to a neutral density of 2.7×10^{11} cm^{-3}. Almost all ion beam facilities include long collimating drift tubes with a characteristic length of several meters. In the IRF ion beam system the beam path length is approximately 2 m. Thus the flux of neutrals amounts to, at least, $10^{-15}\times2.7\times10^{10}\times2\times10^{2} \approx 0.5\%$ of the total ion beam intensity. A typical transmittance of electrostatic deflectors is < 0.01%, which is much lower than the above percentage. Accurate calibrations of the deflection systems using ion beams become, therefore, quite tricky.

In order to evaluate the basic properties of this component we have carried out a dedicated study. A simple neutral particle "tester" (NP-tester) was built (Figure 27). This consists of a two plate electrostatic deflector with deflector factor DF = 26, followed by a CEM with counting electronics. A retarding grid with adjustable potential is set between the deflector and the CEM nose to avoid electron leakage. The deflector voltage is 2 kV, i.e., the cut-off energy equals 52 keV. The CEM can be run both in electron mode (positive bias) and ion mode (negative bias).

In order to check that the NP-tester deflector transmittance is lower than the percentage of neutrals in the ion beam, we have installed a predeflector before the entrance aperture of the tester. The predeflector is a conductive plate with a size of 45 × 85 mm which can be biased positively up to 5 kV. If the transmittance of the main deflector is sufficiently low, the CEM response should not depend on the predeflector bias. That was, indeed, observed. The percentage of neutrals in the ion beam, η, for $\eta << 1$ can be determined as a ratio of the CEM count rate with the biased deflector to the CEM count rate with grounded deflector . For high neutral particle fluxes (η > 10%), independent measurements of the beam intensity with a

Faraday cup were used. In this case the absolute neutral flux value was calculated on the basis of the NP - tester geometrical factor and then normalised to the measured ion flux.

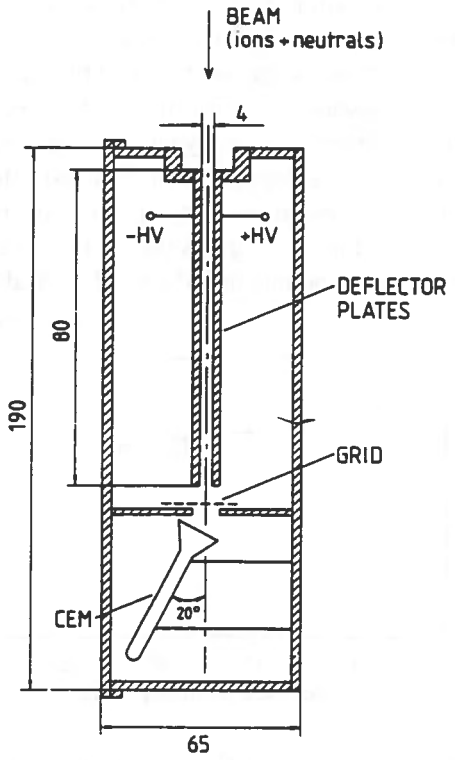

Figure 27. *Neutral particle tester for studying the neutral component in the ion beams.*

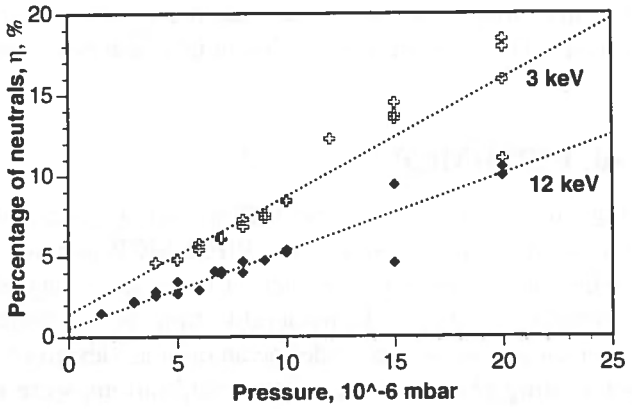

Figure 28. *The percentage of the neutrals in the Ar^+ beam for two different beam energies, 3 keV and 12 keV, as a function of the residual gas pressure.*

Since $\eta \sim \sigma(E)\, N\, L$ for $\eta << 1$, η is proportional to the residual gas pressure and should drop with the beam energy because of the energy dependence of σ. Figure 28 gives the measured dependence of η on the pressure in the chamber for two energies, 3 keV and 12 keV, of the Ar^+ beam . A nice linearity for $\eta < 10\%$ and a drop with energy are observed. The change in slope results from the energy dependence of the CE cross section.

Besides the neutrals generated in the ion beam, another neutral component exists in the test tank. The latter is related to the duoplasmatron, the primary ion source in the IRF ion beam facility. The working pressure inside the duoplasmatron is 10^{-2} mbar and the gas is constantly

leaking to the main chamber, maintaining a rather high pressure over the ion path towards the E × B filter, making this part of the ion beam facility a powerful neutral source. A 90° electrostatics analyzer introduced after the E × B filter should, theoretically, absorb all neutrals. Since the transmittance of the analyzer is not zero, a fraction of the neutrals manages to pass the system, forming a broad scattered beam. This component can be seen in the following test. Maintaining constant conditions in the ion beam generating section (duoplasmatron, E × B filter, electrostatics analyzer) one can change the beam intensity by varying the potential on the beam spreading grid installed just after the electrostatic analyzer. Ideally, η should not depend on the beam intensity in this case but, in practice, η decreases with increasing the beam intensity. Figure 29 gives the results for a 6 keV Ar^+ beam. For these conditions the spreading component amounts to 25% of all neutrals entering the tester.

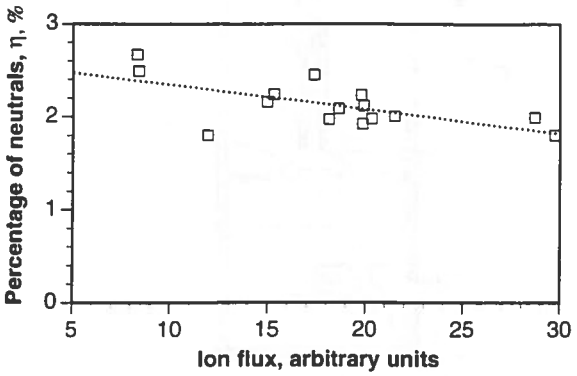

Figure 29. *Dependence of the percentage of the neutrals in the 6 keV Ar^+ beam on the ion flux.*

In conclusion we point out that the presence of a neutral component in ion beams makes it possible to test LENA instruments in ion beam facilities without introducing specially designed charge-exchangers. The absolute neutral flux in this case can be obtained through the ion flux measurements.

LENA Sensor Head. PIPPI-MCP

While some heritage was available for the PIPPI-SSD in terms of basic design and calibrations (except for the deflection system), the PIPPI-MCP part was a completely new development, though following the generic approach of using secondary emitting surfaces for the LENA detection [*Witte et al.*, 1993]. Considerable time was expended on selecting an appropriate sensor and sensor configuration, to define an optimal design of the target block and to determine the target coating characteristics. Some calibrations were performed with the integrated instrument. Because of the strong time pressure we tried to solve problems in the fastest way. For example, we ran rather simple calibrations against the UV background. In order to limit the length of this section within reasonable limits we give a very brief presentation of our results.

Deflection System

Having checked that the basic deflector formula (Formula 3) is valid for the disk configuration in the PIPPI-SSD deflector calibrations, we omitted these tests for the PIPPI-MCP head.

Due to the presence of a significant amount of neutrals in the ion beam for the energy range of interest (1 keV - 20 keV), the transmittance calibrations became rather complicated

and it was possible to obtain only an upper limit for this parameter. To estimate the deflector transmittance we attached a predeflector to the instrument and checked the PIPPI-MCP response in different combinations of the PIPPI deflector and the predeflector being on or off. The tests were conducted for 6 keV Ar^+ beams. The responses for different combinations did not differ from each other by more than 1% and were caused by the neutral component in the ion beam. This means that the PIPPI-MCP deflector transmittance is less than 1% for this energy range.

The azimuthal and elevation responses have been checked in a similar manner to PIPPI-SSD. The measured azimuthal response is shown in Figure 30. The wings on the curve for sector 28 are due to particles leaking from neighboring sectors. In the ASPERA-C instrument the mechanical design was changed to fix this problem but it was impossible to do so for PIPPI. The measured angular width corresponds to the theoretical one for elevation, but is slightly wider for azimuth, 11.5° instead of 9°.

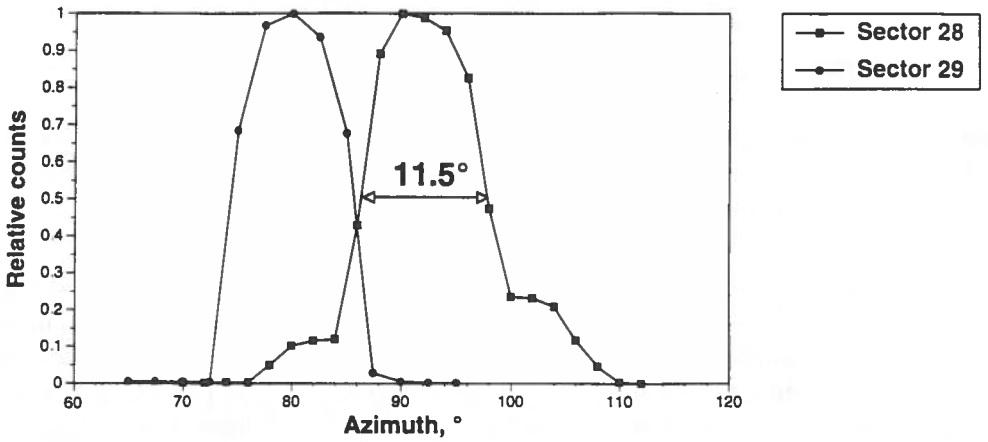

Figure 30. *The PIPPI-MCP azimuthal response of sectors 28 and 29. Sectors neighboring sector 29 were blocked for this test.*

Target Block

The purpose of the target block is to convert, as efficiently as possible, the primary particles (neutrals) into secondaries and reduce, as much as possible, the flux of UV photons reaching the sensors. Besides, it should not worsen the angular resolution, which is determined by the deflector / collimator, i.e., spreading the secondaries should be minimised between the neighboring channels. One of the basic problems we had to solve when designing the target block was to determine the optimal angle of incidence of the neutral beam emerging from the deflector. A grazing incidence (60° - 70° angle to the surface normal) and close to normal incidence (20° - 30°) were considered. Several factors have been taken into account - simplicity of the target block design, light reflection properties, particle reflection properties, conservation of the directional information, working area per sector, and secondary particle yields (since it is a function of the incident angle, see review by *Benazeth* [1982]). The grazing configuration with the 70° incident angle was found to be the most appropriate for the PIPPI-MCP concept. Having chosen the angle of incidence we carried out several tests to understand the particle reflection properties for such configurations. The main conclusion was that collimating walls to prevent scattered / sputtered particles from stimulating neighboring sectors were needed. Thus we came to a star-like design shown in Figure 31. Moreover, the star-like target block improves the conversion of the primary beam to secondaries because the particles undergo multiple collisions with the walls within one sector.

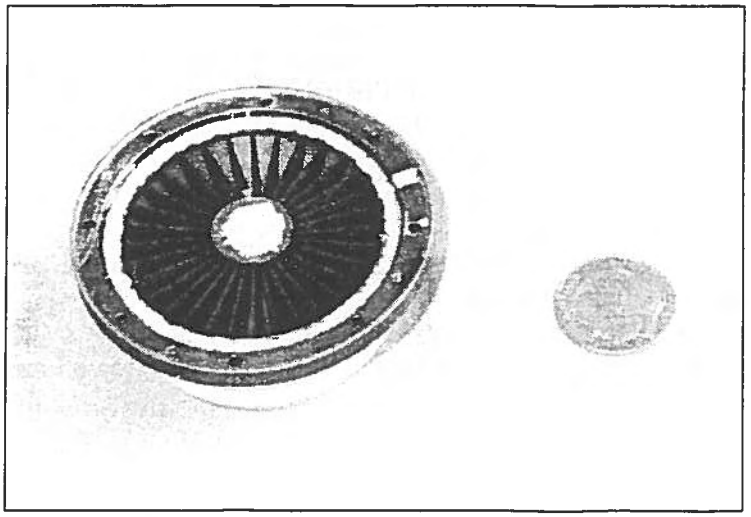

Figure 31. *The PIPPI-MCP target block shown from the back side.*

Altogether 6 different configurations of the target block were tested and an optimal wall length was chosen.

Coating

One of the most important issues in the PIPPI-MCP development was the choice of a UV absorbing coating for the target. This must satisfy the following conditions listed in order of significance. (1) A combination of the coating and substrate must effectively absorb UV photons. (2) The coating should be readily available and simple to apply. (3) It is desirable to have comparatively high secondary ion and electron yields. We have ruled out LiF coating used by *Witte et al.* [1992] due to the complicated mechanical design of our target block and difficulties in maintaining the quality of such surfaces (nitrogen-atmosphere throughout handling / storage, restoration of the surface in flight). We chose DAG 213, a resin-base graphite dispersion, an analogue for Aquadag which is a graphite dispersion in water. The DAG 213 photoelectric properties are rather close to those of Aquadag (T. Harley, private communication) and only slightly worse than for LiF. For example, the total photoelectron current from a surface coated by Aquadag and irradiated by the Sun is only 15% higher than that from LiF surfaces [*Grard*, 1973]. DAG 213 is used as a paint for satellite-borne Langmuir probes and has flight heritage. However, DAG 213, as any graphite compound, has relatively low secondary electron (kinetic) yield. That is the main disadvantage of this material. Moreover, some concerns have been expressed that contamination of the sensor by sputtered graphite atoms will result in a gain drop of the detector.

To investigate the properties of the DAG 213 coating a simple set-up shown in Figure 32 was made. The electron-emitting filament is used to stimulate the CEM with a high count rate for some time until a stable gain is reached (so-called electron scrubbing). With this set-up we performed tests of the sensor contamination by graphite, checked the stability of the DAG 213 coating, defined the optimal technique of the paint application, and performed some preliminary tests to estimate secondary particle yields.

For the contamination test a Mullard 955 CEM was used as a sensor. After 27 hours of electron scrubbing the gain dropped by a factor of 55 and finally stabilized at a constant level. The CEM was biased negatively and the 15 keV Ar^+ widely scattered beam was turned on. The measured PHD of signals from the CEM had a double - peaked shape. One peak originates from more energetic sputtered ions (neutrals) and the second one results from the less energetic secondary ions. This gives an estimate of the number of secondary ions produced.

The test was run for 8 hours. The count rate was 7 - 9 kHz and 2-3 kHz. However, only 70 % of the counts came from secondary ions. Thus the number of accumulated counts was 1.17×10^8. During the test the PHD was taken once or twice per hour. The position of the peaks in the PHD was very stable and, hence, the graphite contamination was negligible .

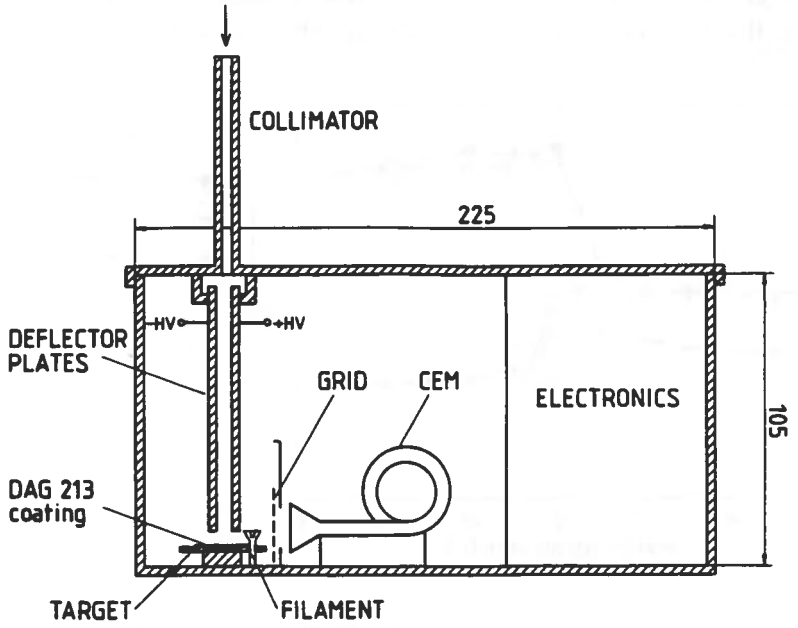

Figure 32. *Set-up used for studying the DAG 213 properties*

The coating stability test was run to confirm that the DAG 213 did not change its properties after accumulation of a certain amount of particles. The set-up pictured in Figure 32 was utilized again but retarding potential spectra of the secondary particles were taken to evaluate the DAG 213 properties. The coating was exposed to a 12 keV Ar^+ beam of a flux of $(1\text{-}2)\times10^7$ $cm^{-2}s^{-1}$ for 7 hours 45 minutes. That corresponds approximately to 4×10^{11} accumulated particles. Figure 33 shows the retarding potential particle spectra before and after exposure. The spectra were taken in both electron and ion mode of the CEM. No significant difference was observed except for a small shift of the secondary ion peak towards lower energies.

An accurate determination of secondary particle yields from coating materials is hardly possible with a set-up similar to ours. The basic problem is that it is not known what fraction of the secondary particles reaches the detector. For secondary electrons, the problem can be solved, at least partially, by setting a high (60V - 100V) potential on the retarding grid. Due to low inertia the electrons follow the electric field lines between the target surface and the grid and almost all of them arrive at the CEM. However, the situation with the secondary ions is much more complicated. Setting a high negative potential on the retarding grid causes acceleration of the secondary ions, but due to their higher mass the ions do not move exactly along the electric field lines and can easily miss the CEM funnel. That is the reason for the drop in the CEM count rate with decreasing retarding potential (Figure 33). In principle, the grid and CEM funnel could be placed parallel to the target surface to improve the electric field geometry [*Bleszynski,* 1985] but in this case scattered primary particles and sputtered atoms contribute to the CEM response as well. Indeed, after interaction with a coating the primary ions (neutrals) leave the surface, mainly, as neutrals, because a charge-state equilibrium is established very quickly during the interaction (on a depth of few Å). The target atoms obtain energy in the interaction process and can leave the material as neutrals as well. A fraction of the primary ions (neutrals) is back-scattered by the surface atoms. Figure 34 illustrates this aspect. Scattered and sputtered neutrals (and the scattered ions for the keV ion beams as well)

can reach the CEM in any mode of operation for the parallel geometry and contaminate the measurements. Effectively, this results in an overestimate of the real yield. Much more sophisticated equipment is needed for accurate absolute measurements (see review by *Honig* [1976]). We should note, however, that in the PIPPI design the integral flux of all particles leaving the target surface exposed by a fixed neutral beam contributes to the instrument response. From this point of view, the exact yield is only of academic importance.

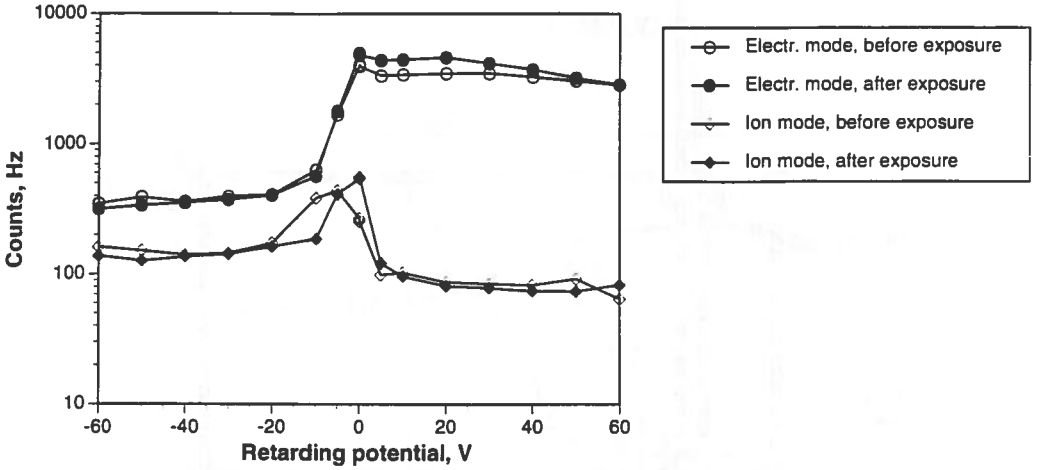

Figure 33. *Retarding potential spectra from the DAG 213 coating before and after exposure to a 12 keV Ar^+ beam of the (1-2)×10^7 $cm^{-2}s^{-1}$ for 7 hours 45 minutes. No significant difference is observed.*

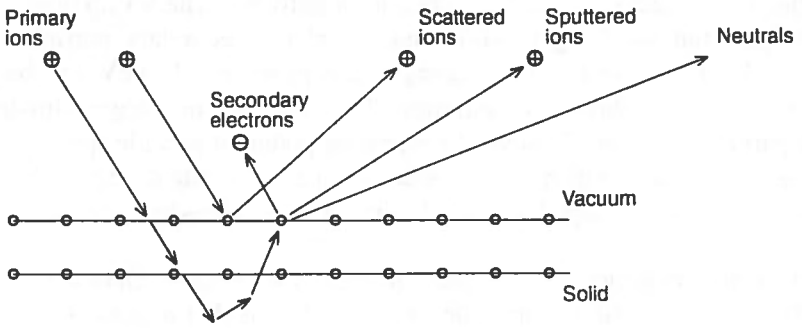

Figure 34. *Schematic of various processes resulting from the interaction of a keV beam with a solid surface.*

Using the set-up shown in Figure 32 it is possibly to get a general dependence of the secondary electron and ion yields on the primary particle energy. We used the Ar^+ beam because it is the most simply generated. Although the secondary electron yield depends on the primary particle mass, the secondary ion yield does not depend strongly on this parameter [*Benninghoven et al.*, 1974]. Figure 35 presents our measurements for two different thicknesses of the DAG 213 coating. The yield for the secondary electrons and ions is given in relative units. An approximately linear dependence on $\sqrt{E}$ is correct because the yields are linear functions of the primary particle velocity for the energy range in question [*Krebs*, 1983; *Benninghoven et al.*, 1974].

The electron and ion yields were normalized to the same number and the ratio between them is correct as well. For one layer coating the ratio is 15.0±3.0 which seems a rather realistic value. If we had known one of the yields from independent measurements, we could

deduce the other one. For example, taking typical secondary electron yields for 1 keV and 10 keV as 2.5 and 8 [*Krebs*, 1983] one can estimate the secondary ion yields of the one layer DAG 213 coating on Al to ~20% and ~50% respectively. For comparison, the secondary ion yields for C and Al are 36% and 100% for the 0.5 keV Ar^+ beam (Commonwealth Scientific Corporation's tabulation) .

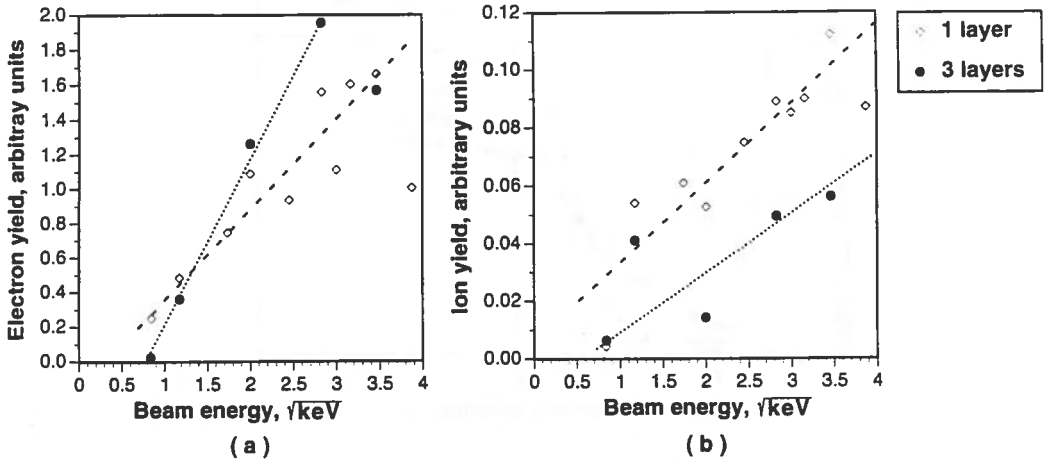

Figure 35. *Energy dependence of the secondary electron (a) and ion (b) yields for the DAG 213 coating applied in one and three layers.*

We did not measure the absolute thickness of the coating and used more useful practical criteria, the number of layers applied. DAG 213 was applied either in one layer or in three layers. Despite the fact that measurements give a lower secondary ion yield for the thicker coating, we used this application because a one layer coating provides worse UV absorption.

Retarding Grid

A retarding grid introduced between the back of the target block and the front of the MCP plays a double role. Being positively (up to + 27 V) or negatively (up to -100 V) biased it improves the transport of secondary particles, either electrons or ions, from the target block to the MCP assembly. Being biased slightly negatively the grid is supposed to make a separation between the photoelectrons and kinetic secondary electrons produced by particles. Such a separation is based on the fact that the photoelectrons are slightly less energetic than the secondary electrons. A lot of concerns have been expressed on the earlier stage of the ASPERA-C design (Grzedzielski and Zarnowiecki, private communication) over the use of the technique for the UV suppression. Since one of the main objectives of the PIPPI experiment was a technological test, we did foresee the possibility of precise (~ 0.1 V) commandable settings of the grid potential within the range -10 V to +15 V. Unfortunately, due to the short time PIPPI was operated, we were not able to check this technique in flight. Hopefully, it will be possible to do so with the ASPERA-C instrument for the Mars 96 mission.

During pre-flight tests of the PIPPI-MCP we made an experimental comparison between retarding potential spectra of photoelectrons and secondary electrons. The V.03 Cathodeon deuterium lamp was used as UV source (see section Calibrations) to simulate UV background. The intensity of the light beam was much higher than the expected UV flux in space from the geocorona (7.95×10^9 $cm^{-2}s^{-1}sr^{-1}$) even after a 1/610 neutral reducing filter. This results in a much higher residual UV photon flux arriving at the sensors in the calibrations. The 6 keV Ar^+ beam used to simulate the ENA flux was also more intense than the expected LENA fluxes. Figure 36 shows typical retarding potential spectra of the photoelectrons and secondary electrons obtained in tests with PIPPI-MCP in flight configuration. The instrument response

for each potential is normalized to the 7.95×10^9 $cm^{-2}s^{-1}sr^{-1}$ UV flux for photoelectrons and the 2×10^6 $cm^{-2}s^{-1}sr^{-1}$ particle flux for secondary electrons. The difference in spectra indicates that the -4.6 V retarding potential could in principle suppress the photoelectrons and one can thus operate the instrument in the electron mode.

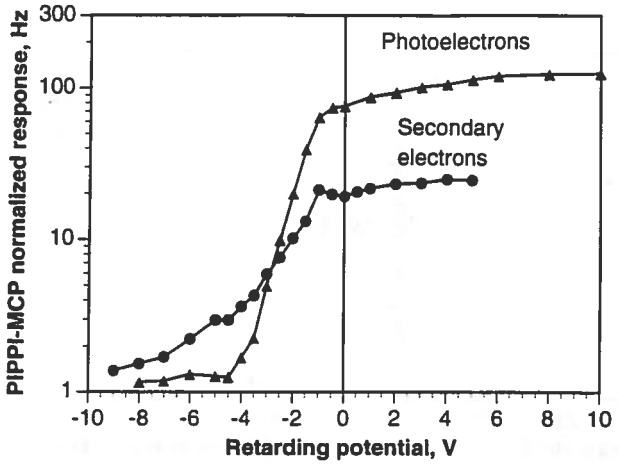

Figure 36. *The retarding potential spectra of the photoelectrons and secondary electrons. The V.03 Cathodeon UV deuterium lamp with the 1/610 neutral filter was used. The beam is 6 kV Ar^+ ions. The instrument response for each potential is normalized to the 7.9×10^9 $cm^{-2}s^{-1}sr^{-1}$ UV flux for photoelectrons and the 2×10^6 $cm^{-2}s^{-1}sr^{-1}$ particle flux for secondary electrons.*

Note, that since the instrument is sensitive to both the secondary electrons and scattered particles which reach the sensor, the instrument response is constant for retarding potentials higher than -9 V ... -10 V and up to -100 V. This also indicates that the scattered particles are mainly neutrals. That was confirmed by direct calibrations for the ions and neutrals.

Sensors

In the initial design of the LENA sensor head a ceramic channel electron multiplier (CCEM) was supposed to be used. The CCEM is a ceramic disk with 32 (initially 64) spiral channels which are covered inside by a secondary emitting glass. The funnels of the channels are along the inner opening and exits emerge along the outer edge. The CCEM was designed and manufactured by Mr. Hans Lauche (Max-Planck-Institut für Aeronomie, Germany). Originally, CCEMs were designed to manage extremely high count rates in the MHz range and the channel impedance was very low, about 80 MΩ per channel. In order to increase the impedance and decrease the power consumption the surface was baked in a hydrogen atmosphere. Intensive tests of the final product revealed the following problems. (1) The oxidation process worsened the semiconductive glass properties. This results in a low gain and unacceptable PHD of the output signals. (2) The spread in the gain between channels is up to a factor 16. (3) There is cross talk between channels. (4) With an maximum achieved impedance of 300 MΩ per channel, the CCEM power consumption is 1W which is still not acceptable for the severe Astrid power budget. Since it was impossible to fix all these problems within the time frame of the Astrid project, a decision was taken to use MCPs as detectors. A compromise between the large diameter required and limited funds available resulted in the choice of the 56 mm diameter MCPs manufactured in Russia. Excellent results have been previously achieved in laboratory tests with a Z-stack assembly from these plates [*Gruntman et al.*, 1987]. They managed to obtain a gain up to 8×10^8 and amplitude resolution down to 20%. We have conducted our own intensive testing of these MCPs [*Barabash and Olsen*, 1995e]. The main conclusions are the following. (1) A spread in the MCP resistance from 30 MΩ to

900 MΩ requires a careful sampling of the plates to be used in chevrons or Z-assemblies. (2) The gain (up to 2×10^8 in the Z assembly with no spacers) and the amplitude resolution are good enough to match the preamplifiers used in the PIPPI-MCP. (3) The spread in the gain over the MCP surface is up to 12% (for a chevron). (4) The gain stability, voltage dependence, and count rate dependence are satisfactory. Thus the MCPs can be utilised in the PIPPI experiment.

Trying to optimise the MCP stack in terms of the higher gain, lower noise, mechanical simplicity, and stability in operation, we tested altogether 6 different configurations (chevron, chevrons with 20, 88 and 500 μm spacers, Z-assembly, Z-assembly with 22 μm spacer). A classical Z - assembly was found to be the best. A 32 channel anode completes the MCP stack.

Sensor Electronics

Due to the limited compartment available for the MCP and its 32 channel electronics (one PC board, diameter 155 mm) we were forced to use a hybrid solution for the charge sensitive preamplifier, discriminator, and digital pulse conditioner. A MOCAD (Monolithic Octal Charge Amplifier/Pulse Discriminator) chip was used. Since the chip is under development in IMEC vzw, Belgium, for the MAREMF instrument on the Mars 96 mission, we had to use a raw product. 4 chips with 8 channels each provide 32 required channels. During the PIPPI-MCP development a rather poor quality of the individual chips was discovered. Only every second had a reasonable performance. Since the electronic design could not be changed, we had to take a risk. Unfortunately, one of the 4 preamplifiers failed and the most important antisunward direction within +/- 40° was lost.

Efficiency

The efficiency for particle detection in the ion mode of the MCP operation was checked against the 6 keV Ar beam with the retarding grid biased at -100 V. The basic idea is to obtain the instrument response for a variable flux of the incoming particles and compare it with that calculated from pure geometrical considerations. According to Figure 3 [*Barabash et al.*, 1995a] a flux of 7×10^3 $cm^{-2}s^{-1}sr^{-1}$ results in the response 0.1 s^{-1}. The geometrical factor is 2.5×10^{-3} $cm^{-2}s^{-1}$ and, hence, the efficiency is $0.1 / (2.5\times10^{-3}\times7\times10^3) = 0.6$ %. As expected, this is less than the secondary yield from DAG 213. In a similar manner, we can define the efficiency in electron mode with the retarding grid biased to +5 V. According to Figure 36 a flux of 2×10^6 $cm^{-2}s^{-1}sr^{-1}$ results in the response 2.5×10^1 s^{-1}. Thus we arrive at an efficiency $2.5\times10^1 / (2.5\times10^{-3}\times2\times10^6) = 0.5\%$, which is similar to that in the ion mode. Since the LENA sensor head does not have energy resolution, particles with all energies contribute to the instrument response and the real efficiency is higher by, at least, a factor of 3 - 5. For comparison we can cite the comparable efficiency of 3.5% - 7% for the energy range 0.8 - 10 keV theoretically estimated by *McComas et al.* [1992] for a much larger and much more sophisticated hypothetical LENA instrument based on ultra-thin conversion foils.

The above defined efficiency should be included in the PIPPI-MCP geometrical factor.

UV Suppression

In order to check the instrument immunity against UV radiation we have performed a number of tests with the V.03 deuterium lamp with a magnesium fluoride window (Cathodeon, Ltd.). The UV spectrum produced by the lamp is given in Figure 37. The absolute integral radiance was not known and we built a simple metal cathode detector to calibrate the source [*Samson*, 1967]. Figure 38 shows the used set-up. A gold plate 10.8 mm × 10.5 mm was utilized as a cathode. The dependence of the photocurrent versus the collector voltage for the lamp current 250 mA is given in Figure 39. The full photocurrent from the ~1 cm^2 gold plate is 1.13×10^{-8} A.

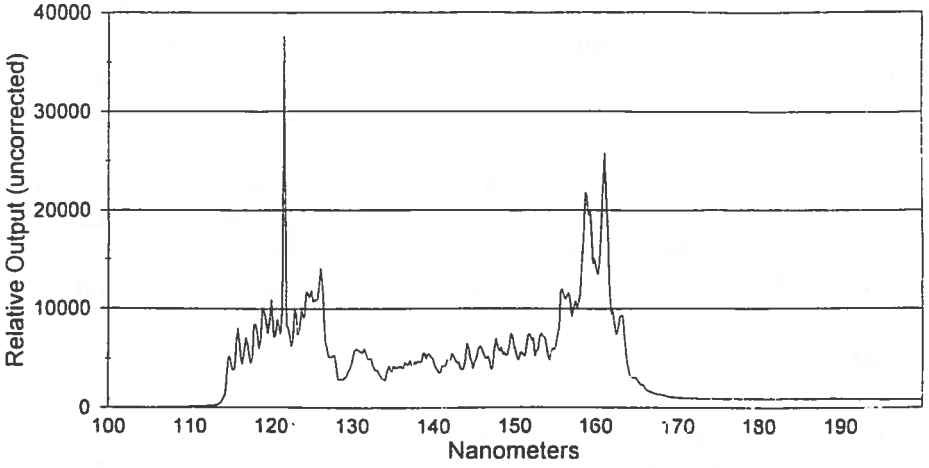

Figure 37. *UV spectrum from the V.03 deuterium lamp.*

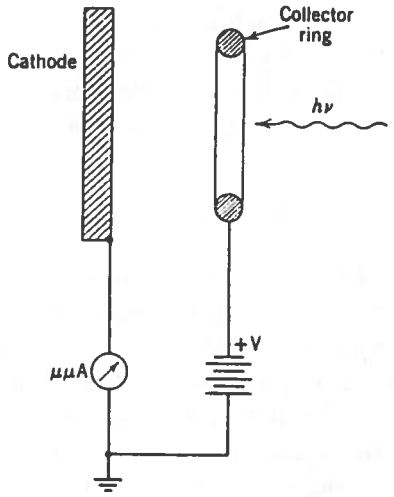

Figure 38. *UV detector with a simple metal cathode.*

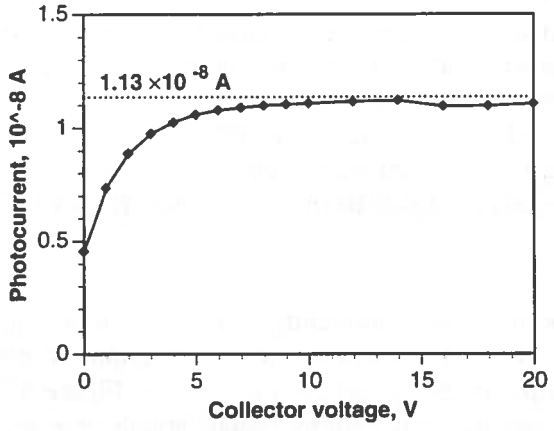

Figure 39. *The photocurrent from the cathode versus the collector voltage.*

Having integrated the spectrum in Figure 37 weighted by the gold photoelectron yield and knowing the set-up geometry, we came to the absolute integrated radiance 1.04×10^{16} photons

$cm^{-2}s^{-1}sr^{-1}nm^{-1}$. Such a high photon flux requires a substantial reduction with neutral filters. Multilayer stacks of the metallic grids were found to be appropriate filters. The instrument response for even lower UV intensities was extrapolated.

The UV background for the 7.95×10^{9} $cm^{-2}s^{-1}sr^{-1}$ UV flux was found to be 0.6 s^{-1} in the ion mode (Figure 3, *Barabash et al.*, 1995a) and 1.2 s^{-1} in the electron mode of the PIPPI-MCP operation (Figure 36). These values are rather close; the excess in the electron mode is due to either photoelectrons generated below the retarding grid or from photoionisation of the residual gas trapped inside the target block. Taking a geometrical factor 2.5×10^{-3} $cm^{2}sr^{-1}$ and averaging the UV background to 1 s^{-1} we come to an integral UV efficiency of $1 / (2.5\times10^{-3}\times 7.95\times10^{9}) = 5\times10^{-8}$. The MCP UV efficiency is 1% and, hence, the target UV suppression is 2×10^{5}. That is a rather high value for such a simple system.

Review of the PIPPI Results

The PIPPI data analysis has just begun and here we briefly report some preliminary results. In the initial stage of the analysis only the data from the HENA sensor head were considered, since they are simpler for interpretation. As pointed out, the SSDs within the sunward hemisphere were contaminated by reflected photons, so we are only concerned about imaging in the antisunward hemisphere. Furthermore, over the polar part of the Astrid orbit, up to 70° magnetic latitude, the energetic particle background is low and detection of the ENAs may be performed rather safely even when the deflection system has no voltage.

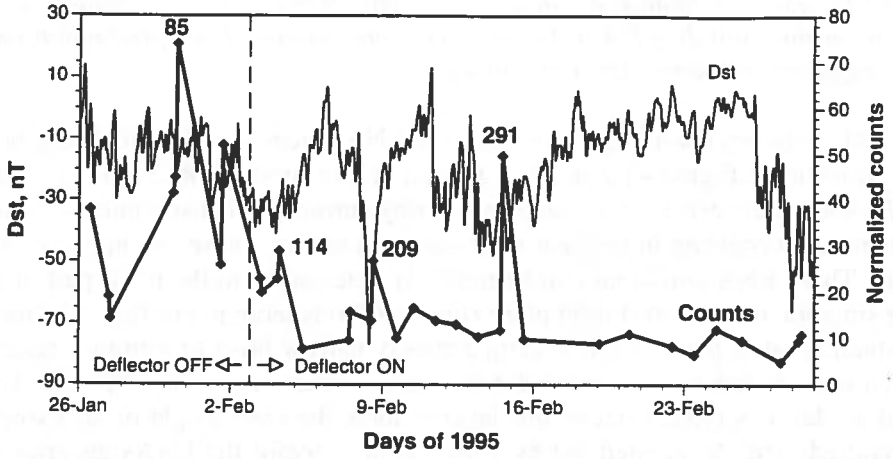

Figure 40. *Normalized accumulated counts from sensor 8 (Figure 19) for energy channels 1 and 2 from the polar part of the Astrid orbit (thick line). The D_{st} index for the same period is also shown by the thin line (courtesy of WDC-C2, Kyoto, Japan). It is assumed that the counts recorded resulted from ENAs generated in the subauroral / auroral region. The peaks corresponds to orbits 85, 114, 209, 291.*

In order to identify orbits with the highest ENA activity, we chose a sector in the antisolar direction and accumulated its response for a time until the spacecraft was in the polar part of the orbit. It is natural to assume that the majority of the counts recorded resulted from ENAs generated in the subauroral / auroral region which is the most intense source of the ENAs due to the neutral density being highest there. Figure 40 presents the accumulated counts from sensor 8 (Figure 19) for all available orbits. The counts are normalized to the same time interval. The thin line in Figure 40 gives the D_{st} index for the same period. We also show the data for the initial phase of the mission when the deflection system had no voltage. Four well-pronounced events with increased counts rates are identified. As will be seen later, the

morphology of the structures in all four images is the same and this indicates that the peaks corresponding to orbits 85, 114, 209, 291 are, indeed, caused by ENAs. The observed increases in the ENA emissions correlate with decreases in the D_{st} index (which characterizes the amount of particles in the ring current and, hence, the amount of the ENAs generated within the inner magnetosphere). Before showing the images recorded we would like to discuss some general features of ENA imaging at low altitudes.

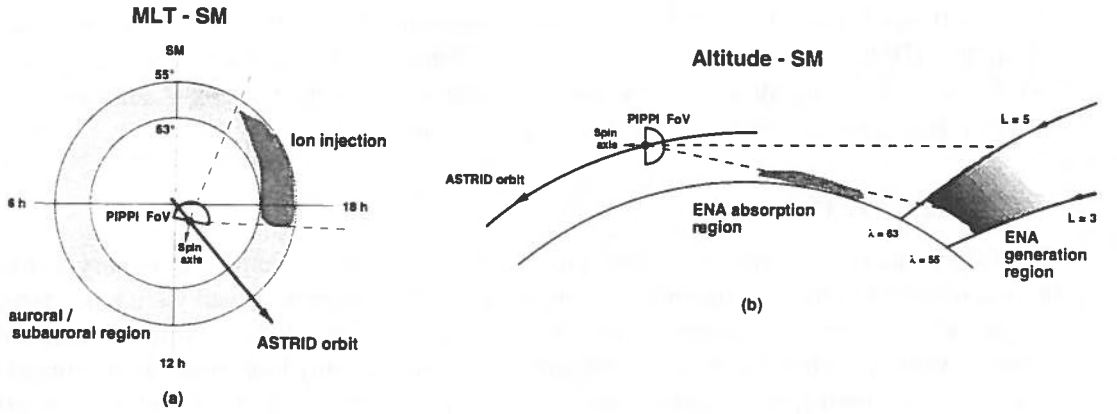

Figure 41. *General schematics of ENA detection from the Astrid orbit. (a) is a typical Astrid orbit in MLT - SM coordinates. A range of L - shells between 3 - 5 is shadowed. (b) is the Astrid orbit in the altitude - SM projection. The most intense ENA production takes place within a comparatively narrow layer of altitudes.*

Figure 41 describes the general schematics of ENA detection from the Astrid orbit in two different projections. Figure 41*a* shows a typical Astrid orbit in *MLT - SM* coordinates. A range of *L* - shells between 3 - 5 is shadowed. A ring current ion density intensification, due to e.g., an injection, occurring in the near dusk sector as shown, causes an increase in the ENA production. These ENA emissions can be remotely detected from the polar part of the Astrid orbit. The situation in the Astrid orbit plane (Figure 41*b*) is more interesting. The most intense ENA production takes place within a comparatively narrow layer of altitudes because of the exponential dependence of the neutral density (in a similar way to the depletion layer in the solar wind at Mars). A typical size of this layer is about the scale height of the exosphere, i.e., several hundreds km. As pointed out by *Chase et al.* [1995b] the ENAs generated at lower altitudes must pass through even lower altitudes to be detected by the instrument. The neutral density there is much higher and the process of ENA flux attenuation due to electron stripping starts to play a role. This effect decreases even more the thickness of the visible ENA generation region. On the other hand, this also implies that the numerical simulation of expected ENA images becomes a complicated task involving solving full ENA transport equations as described by *Roelof* [1995]. Thus, in a 3D presentation of the antisunward hemisphere, the regions of the ENA generation should look like a comparatively narrow band from dusk to dawn. If an MLT asymmetry in ion distribution takes place as shown in Figure 41*a*, the band is asymmetric as well. The asymmetry may also be caused by an attenuation of ENA fluxes coming from the dawn - midnight sector because these atoms travel at very low altitudes at certain parts of the trajectories and can be stripped into ions.

The ENA images corresponding to the four identified events are presented in the fish-eye projection in Plate 1. In these polar coordinates, the radius is given by the polar angle of each sensor in the frame related to the spacecraft spin axis, and the azimuth angle is the satellite spin angle. The blue line at the bottom part of the images is the Earth's limb. The line in the limb area is the terminator. The increase in the count rate in pixels on the left side of the

images for orbits 114 and 209 is due to photon contamination and should be disregarded. The images correspond to the four identified events shown in Figure 40. The sensor numbering corresponds to Figure 19. The energy window is 26 - 37 keV (channel 1). The general structure of the images is as one expects from geometrical considerations, a dawn - dusk elongated asymmetrical narrow band at low altitudes. However, there are clear differences in details of the morphology. The most pronounced feature is the different altitude of the ENA emitting regions, and that has not yet been quite understood.

Due to the high neutral density at low altitudes, ENA emissions are strongly dependent on the properties of this component. As found out by *Chase et al.* [1995b], computer simulations using only a Chamberlain atomic hydrogen exosphere could not reproduce the observed thickness of the ENA emitting region. This implies that additional exospheric components like O or He with much smaller scale heights (≈ 100 km) must be present to provide the observed features. The modified simulations including additional exospheric components and using the solar and geomagnetic indices for orbit 291 turned out to be in agreement with the observations. Such a consideration illustrates that the morphology of ENA images at low altitudes is very sensitive to the neutral density profiles determining the ENA production. This suggests that low-altitude ENA imaging may offer a tool for remote diagnostics of exospheric parameters in regions of energetic particle precipitation *Chase et al.* [1995b].

So far, four unambiguous ENA images of the ion population at low altitudes in the precipitation region have been identified in the PIPPI-SSD data (Plate 1). Thorough analysis of the magnetospheric conditions and temporal evolution of the ENA emissions for time intervals preceding and following orbits 209 and 291 has revealed that these episodes seem to correspond to different magnetospheric events; a substorm ring current intensification and an isolated ion injection [*Cson Brandt et al.*, 1995; *Chase et al.*, 1995b]. The studies of these two events complement each other and illustrate what ENA imaging can provide for ring current morphology evaluation.

Besides localized events like isolated ion injections, trapped particles of the ring current approaching low altitudes at mid-latitudes are a constant source of ENAs. In certain directions in the vicinity of this generation region the ENA flux integrated along the line-of-sight can reach 10% of the local ion flux in the energy range 20 - 30 keV [*Barabash et al.*, 1995d]. Thus an electrostatic deflection system with a transmittance less than 1%, as on PIPPI, may provide a diagnostic of the ENAs even in the presence of charged particles. Moreover, the ENAs in the subauroral region are characterised by (1) a strong azimuthal anisotropy, (2) differences in the energy spectra slopes between neutral atoms and charged particles, and (3) a typical width of the pitch-angle distribution of 40° - 50°. The features (1) and (3) have been observed by *Søraas and Aarsnes* [1995] at altitudes of 450 km by a rocket-borne SSD experiment. The above circumstances can be used to separate the ENAs from the residual charged particles leaking through the deflection system. Operation of the deflection system in the sweeping voltage mode improves the identification of the ENAs. Such an analysis of the PIPPI data has identified a situation when the instrument response did not depend on the deflector voltage and the particles recorded were characterized by the features (1) and (3). The fluxes of these particles were found to be up to 10^4 $cm^{-2}s^{-1}sr^{-1}keV^{-1}$ in the energy range 20 - 40 keV. Further detailed studies are required to clarify this subject. However, if the above consideration is correct, it suggests that the high energy plasma of trapped particles at low altitudes (~1000 km) and mid-latitudes contains a significant (up to 10%) admixture of ENAs, i.e., several components are present simultaneously, namely electrons, ions, and HENAs immersed in the neutral background. An injection into the ring current increases the ion intensity at low altitudes and changes the pitch-angle distribution. This increases the production of ENA above that under average conditions, making it possible to image the injection region remotely as was shown above [*Cson Brandt et al.*, 1995; *Chase et al.* 1995b].

Plate 1. *The ENA images presented in the fish-eye projection. In these polar coordinates, the radius is given by the polar angle of each sensor in the frame related to the spacecraft spin axis, and the azimuth angle is the satellite spin angle. The blue line at the bottom part of the images is the Earth's limb. The line in the limb area is the terminator. The increase in the count rate in pixels on the left side of the images for the orbits 114 and 209 is due to photon contamination and should be disregarded. The images correspond to the four identified events shown in Figure 40. The sensor numbering corresponds to Figure 19. The energy window is 26 - 37 keV (channel 1).*

ENA images from the polar cap
Astrid / PIPPI - SSD

Anti-Sunward Hemisphere

Sensors 7 8 9 10, 26 - 37 keV

Orbit 85

Jan 30, 1995 1221:31-1222:40

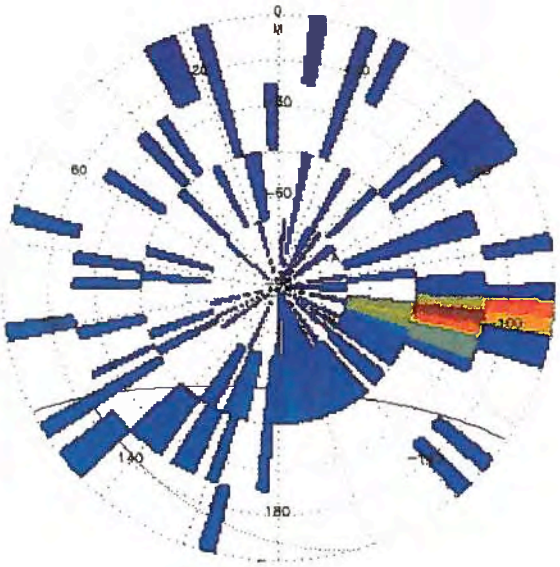

Orbit 114

Feb 1, 1995 1508:46-1509:49

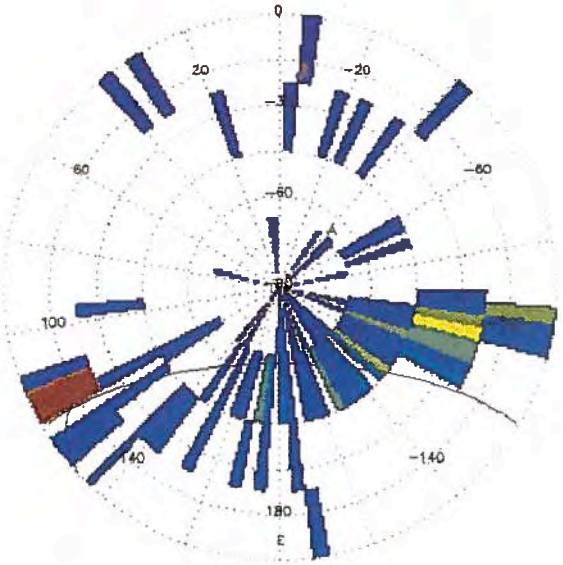

Orbit 209

Feb 8, 1995 1331:42-1333:21

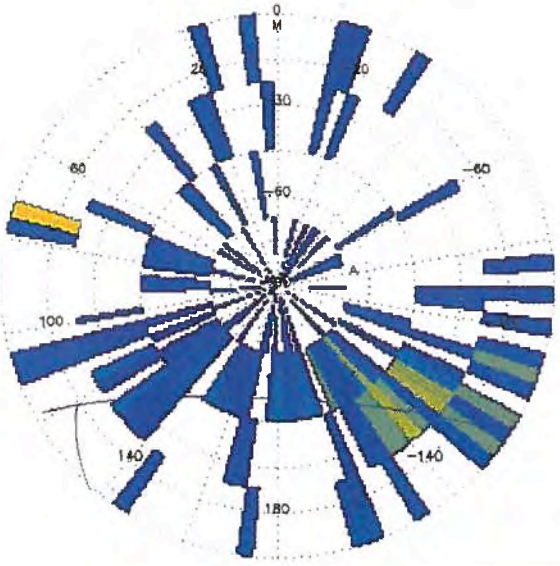

Orbit 291

Feb 14, 1995 1308:03-1309:43

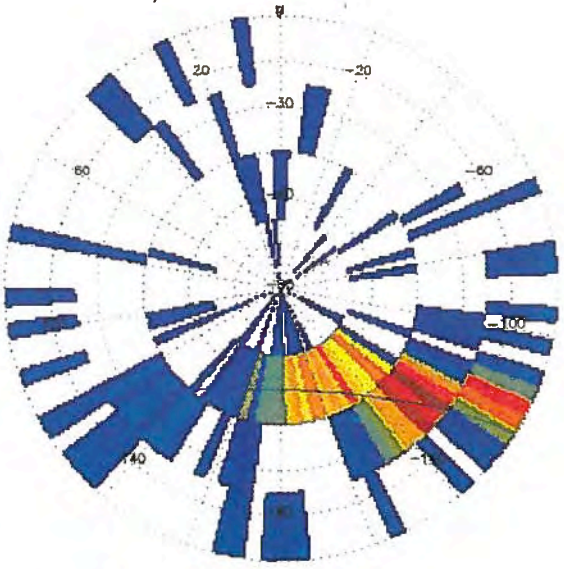

Summary and Future Prospects

The dissertation deals with studies of the plasma - neutral interaction effects near Mars and the Earth and development of instrumentation to measure the ENA component which such a coupling frequently results in.

In *Introductory part,* we have, first of all, reviewed the basic phenomena resulting from the collisionless interaction between the solar wind plasma and the exosphere of Mars and / or the gas / dust torus along the orbit of the Martian satellite Phobos. Measurements performed by the ASPERA mass spectrometer on the Martian probe Phobos were the basis for the analysis of specific effects (Papers I - VII). A general conclusion deduced from this consideration is that the Martian exosphere plays an important role in the solar wind - planet interaction due to a strong coupling between plasma and neutral gas. One way to study this coupling experimentally is to measure the ENAs which result from the CE process between the ion and neutral components. ENA measurements also represent a universal technique of remote imaging of space plasmas. Moreover, ENAs play a role in the plasma dynamics and transport for some parts of the planetary magnetosphere and cometary environments and, thus, need to be studied to understand the physical processes there. Generally speaking, ENAs can be considered as a specific component in the space plasma - neutral system because they possess a number of unique properties distinguishing them from electrons, ions, and cold neutrals. To make adequate measurements of this component a new type of instrumentation is required. The second part *Measurements techniques* provides a description of the experimental work related to the development of the ENA imager PIPPI which has been designed, built and flown on the microsatellite Astrid in low altitude polar orbit at the Earth. The following has been achieved in this first ever satellite-borne ENA experiment .

(1) Unambiguous ENA images of the ring current structures at low altitudes have been obtained. It was also shown that ENA imaging at low altitudes may be used as a tool not only for remote plasma diagnostics but for evaluation of basic exospheric parameters such as the exobase density and temperature.

(2) Several important components of ENA instrumentation such as a deflection system, target block and UV suppressing coating have been developed and tested in flight.

(3) Experience in building and calibrating ENA instruments has been gained.

(4) In developing the PIPPI experiment, several promising technological aspects which could be used in future LENA imagers have been found.

(5) The PIPPI experiment was a part of the Astrid mission which was focused on technological demonstration that microsatellites can be used in performing highly innovative, risky experiments. This demonstration was achieved.

The successful realisation of the first ever scientific microsatellite mission Astrid encouraged us to continue working out this concept and the next microsatellite-based project AKKA is now under discussion. This is a follow-on of Astrid both scientifically and technically. A similar platform is suggested to carry three instruments: LENA and HENA imagers, and UV telescopes for the He^+ (30.4 nm) and O^+ (83.4 nm) lines. Such a spacecraft launched on a highly elliptical orbit will be able to perform truly global imaging of the inner magnetosphere as suggested by *Williams et al.* [1992].

PIPPI, with its rather modest sensitivity, is the first step (that is why it is Prelude!) and marks the beginning of experimental adventures in ENA imaging. More sensitive instruments need to be flown to get a better view of the Earth's magnetosphere and plasmas in other planetary environments, and such more powerful (and much more expensive) missions for global magnetospheric imaging have been proposed by the American groups. MIM, IMAP, MI, and HI-LITE constitute splendid proposals, but these have not yet been approved because the idea of global imaging is still too innovative and is not generally accepted. But we hope

that the PIPPI-inspired findings will help to turn the opinion of the broader scientific community towards this novel and exciting area of ENA imaging.

Finally, a summary of each paper included in the dissertation is presented. We have also added an assessment of the importance of these publications for the chosen field of research. It should be noted, however, that such assessments are inherently subjective.

Paper I "Picked-up protons near Mars: PHOBOS observations" presents observations of the pickup protons originating from ionization of the Martian hydrogen corona in the solar wind. The protons appear as a second weak peak in the energy spectra observed by the ASPERA mass spectrometer from the sunward direction when the Phobos spacecraft was in the upstream region of the Martian bow shock. The most pronounced measurements were made on February 11, 1989 when the spacecraft was out of the ion foreshock and the influence of particles reflected from the bow shock was minimized. The number density of the pickup protons increased with approach to the planet and reached 0.05 cm^{-3} near the bow shock surface. The cyclotron instability of the beams of these new-born particles results in magnetic field fluctuations near the proton gyro-frequency in the satellite frame of reference. These waves lead to a pitch-angle diffusion of the pickup particles and broadening of the distribution function, which is initially of a ring-like shape. The broadening may be evaluated quantitatively from the conditions of visibility, i.e., the conditions when the narrow field-of-view of the instrument can "see" the pickup protons. The spreading turned out to be 20° - 30°, which is not unexpected because there is no room at Mars for the instability to develop. Comparing the pickup proton flux with the one calculated from the hydrogen profile obtained from the Lyman α measurements on Mariner 6 and 7, one may estimate the fraction of the protons measured by the instrument. Having found this coefficient (~20%) the absolute pickup proton flux can be evaluated. The dependence of the pickup proton flux on altitude does not agree well with the calculated one. The reason for this seems to be related to the difference in exospheric temperature and exobase density for the Phobos and Mariner 6 and 7 epochs. The new hydrogen profile is obtained by forward-modelling.

The paper reports direct measurements of the pickup protons responsible for a new planetary phenomenon, upstream waves at the proton gyro-frequency [*Russell et al.*, 1990]. The obtained estimation of the pitch-angle diffusion of the new-born protons is important for better understanding the plasma - neutral interaction effects. The paper shows also similarities in processes taking place at Mars and comets in their interaction with the solar-wind. The direct detection of the exospheric protons also demonstrates the importance and broad possibilities of the plasma measurements in studying phenomena traditionally related to planetology. For the time being, the issue on the upstream pickup protons is more or less sorted out. The planetary ions He^+ and O^+ have not been discovered in the upstream region in the ASPERA data. However, it would be interesting to investigate again the magnetic field data in terms of a search for turbulence at the corresponding gyro-frequencies.

Paper II "Reflected ions near Mars: PHOBOS-2 observations" discusses the ASPERA mass spectrometer measurements made when the spacecraft was in the ion foreshock of the Martian bow shock. The detected particles result from gyrating specularly reflected ions and field aligned beams propagating upstream from the bow shock. Comparison with a simple model of the specular reflection explains the observations outside the bow shock foot rather well. High proton fluxes recorded inside the foot do not agree with this model and seem to result from kinetic processes predicted for the compact Martian bow shock [*Moses et al.*, 1988] where typical sizes are close to the proton gyro-radius. The density of the back-streaming ions at the Martian bow shock reached 0.4 cm^{-3}, which is 30% of the solar wind density. The planetary upstream region is not deep, resulting in a shortage of space for different instabilities to develop similar to the pickup proton situation. That is why no reflected beam disruption is observed and only beam-like distributions were recorded.

The paper presents the first ever observations of reflected ions at the Martian bow shock, which is a more complicated structure than the well-investigated terrestrial bow shock. The paper confirms qualitative theoretical predictions concerning the importance of kinetic effects in the Martian bow shock formation and provides an experimental input for more quantitative consideration. Another important contribution of this paper is the measurement of the number density of back-streaming protons in the Martian upstream region.

Paper III "Upstream regions at Mars" reviews the ASPERA observations in the Martian ion foreshock, electron foreshock and outside these regions. It is shown there that back-streaming protons propagating upstream in the ion foreshock region could account for the 60 km/s deceleration of the solar wind, while the pickup protons dominate outside this region and can take away about 2 km/s. Thus the reflected particles seem to play a much more important role in the planet - solar wind interaction at Mars than they do at the Earth. The Martian electron foreshock demonstrates features similar to all planetary bow shocks. Intense fluxes of upstream propagating electrons in the electron foreshock region result in the generation of Langmuir oscillations. A good correlation between such electron streams and wave activity near the plasma frequency is observed.

Basically, the paper states the previously unknown importance of the back-streaming protons for the solar wind deceleration at Mars. Indeed, at the Earth the back-streaming ions provide $< 8\%$ deceleration [*Bonifazi et al.*, 1980] while at Mars it is 60%.

The problems addressed in Papers II and III should be, in the first order, further investigated together with plasma wave measurements made on the Phobos spacecraft. Some results on the wave activity in the upstream region have already been published [*Russell et al.*, 1990; *Grard et al.*, 1991; *Skalsky et al.*, 1992] but no particle measurements were used in these analyses. The next Martian missions of the Russian Mars 96 and the Japanese Planet-B to be sent to Mars in 1996 and 1998 must address this issue by performing plasma measurements within the bow region with as high time resolution as possible.

Paper IV "Indirect detection of the Martian helium corona" presents the first ever *in situ* observations of the helium ions originating from the Martian exosphere. These were detected by the ASPERA mass spectrometer as particles with $M/q = 4$ in the vicinity of Mars. A significant difference between the measured particle velocity and the solar wind velocity proves that these ions are He^+ of planetary origin. Two observed populations with significantly different typical energies correspond to ions picked up by the solar wind and to ions extracted from the upper ionosphere by an electric field. The observed density of the pickup He^+ ions was 0.02 - 0.1 cm^{-3} and the He^+ density in the plasmasheet was 0.2 - 0.7 cm^{-3}.

Paper V "Measurements of nonthermal helium escape from Mars" deals with the determination of the total helium outflow from Mars due to interaction with the solar wind. A new algorithm has been developed to calculate this value from Phobos measurements along circular orbits. A search through all available data has identified 12 orbits suitable for analysis and the averaged nonthermal helium escape was found to be 1.2×10^{24} particles/s. This is a conservative estimate and the escape may range up to a factor of 2 more than this. Assuming that the helium ions originating in the exosphere outside the obstacle contribute the most to this outflow, the theoretical value for the escape can be calculated. Then by comparing these two numbers one can scale the helium profile to obtain an agreement with measurements. However, the observations of the weak EUV emissions (108 photons) from the Martian He I [*Krasnopolsky et al.*, 1994] give an abundance that is 19 times lower than that deduced from the ASPERA measurements. There are several reasons which could account for the difference. The solar conditions are quite different for the time periods of the Phobos mission and EUV measurements. There might be a higher uncertainty than thought in the number of detected photons due to absorption in the Earth's upper atmosphere or the helium escape mechanism may need to be reconsidered. The observed high helium outflow may suggest a much higher production rate than assumed. This can be related to a higher abundance of U than expected or

with other crust characteristics than those used in models. Furthermore, the helium may be delivered on Mars by the solar wind as it is, for instance, on Mercury.

The discovered discrepancy is not yet understood and much better *in situ* measurements of both the He^+ ions and the helium neutral profile are required to clarify the subject. A new improved data set will, hopefully, be obtained with the new Martian missions. An UV photometer to be flown onboard the Mars 96 mission is planned to measure the exospheric emissions from O I (130.4 nm), He I (58.4 nm) and O II (83.4 nm). The satellite will also carry a variety of hot plasma instruments. Planet-B will include an EUV 30.4-nm He^+ imager and a hot plasma mass spectrometer. Meanwhile, a detailed study of the solar wind α particle distribution at Mars is planned to be made using the ASPERA data. This could give a key to understanding the possible process of helium delivery from the solar wind.

Papers IV and V are of discovery type. They report the first detection of helium at Mars and describe its outflow characteristics. The crucial importance of these papers is that they both are interdisciplinary studies and emphasise the significance of plasma phenomena in planetological investigations. Thus they are also an attempt to introduce a broader view on the problem of solar-wind interaction with planets.

Papers VI "Indirect evidences for a gas/dust torus along the Phobos orbit" reports magnetic field and plasma peculiarities which are supposed to be related to the Phobos torus. Increases in the electron density correlating with a decrease in the magnetic field have been observed when the satellite approached the Phobos orbit both in the solar wind and in the Martian magnetosphere. Weak disturbances in the proton density and velocity have been also observed. Some features possibly related to the shadowing of the tailward moving plasma in the Martian magnetotail have also been detected. All these observations, so-called "Phobos events" may be interpreted as indications of the solar wind interaction with the Phobos gas / dust torus predicted theoretically. The characteristic transverse dimensions of the structures are in the range 100 - 1000 km.

The main objective of the paper was to present observational facts rather than to give a theory of the phenomenon. Later on, this paper has initiated more than ten deeper theoretical studies and numerical simulations dealing with the subject. New findings in the data from the ASPERA instrument and from the magnetic field and wave experiments have been published as well. However, the problem is still far from being solved. Much more comprehensive plasma and dust measurements accompanied by the UV, IR and visible observations of Phobos and its environment are needed. Unfortunately, neither of the next Martian missions (Mars 96 and Planet-B) will have suitable orbits to perform such studies, but there are proposals to try to observe this hypothetical torus with the Hubble telescope. The Planet - B spacecraft will carry a dust detector which may be able to see the dust halo, a remote part of the Phobos dust disk consisting of the smallest grains which are spread out by electromagnetic forces [*Horanyi et al.*, 1990].

Paper VII "On a possible dust-plasma interaction at Mars" continues the consideration of the Phobos dust torus but deals, mainly, with dynamics of the dust grains orbiting Mars along trajectories close to the Phobos orbits. These particles are moving through various plasma domains of the Martian magnetosphere and may undergo electrostatic disruption there, producing very fine motes in the range 0.005 - 0.1 μm which can stay positively charged for a time comparable with their orbital period. A negatively charged spacecraft will attract such particles and an ion spectrometer with wide enough mass range (1 - 10^8 amu/Q, where Q is the particle charge) can detect these grains. This model may explain the signals detected inside the Martian magnetosphere in channels 10^3 - 10^7 amu of the ASPERA mass spectrometer. The key point of the paper is the consideration of dust grain evolution with the use of the diagram representing particle potential vs. particle size. The diagram gives a clear qualitative picture of the interaction of dust with plasma and of the electrostatic disruption of grains which may take place in the Martian magnetosheath region.

Electrostatic disruption has been observed under laboratory conditions [*Svestka et al.*, 1993] but only two observations in space have been reported so far [*Fechtig et al.*, 1979; *Fomenkova and Mendis,* 1992]. The particle potential - particle size diagram introduced in the paper is a universal tool and can be used to consider the grain evolution in any dusty plasma. Another aspect that this paper brings to attention the detection of massive (10^3 - 10^7 amu) particles by conventional plasma mass spectrometers. Particles with masses up to ~500 amu have been detected in the terrestrial atmosphere with a rocket-borne quadrupole mass spectrometer [*Schulte and Arnold,* 1992] while detection limits for CEM and MCP detectors are much higher and, in fact, are not known. Extra experimental studies of the dependence of sensitivity for different types of detectors on projected masses are, indeed, needed to clarify the subject.

Paper VIII "Diagnostic of energetic neutral particles at Mars by the ASPERA-C instrument for the Mars 96 mission" gives estimations of the ENA fluxes generated at Mars and discusses the feasibility of ENA measurements with the ASPERA-C experiment for the Mars 96 spacecraft. The highest ENA flux results from the solar wind flowing through the huge Martian hydrogen corona. However, detection of these ENAs is quite difficult because they are superimposed on the solar UV flux. ENAs coming from the shocked solar wind within the Martian magnetosheath are the most attractive for observation due to their high fluxes. These ENAs can also provide information about the shape of the boundary separating the solar wind and the Martian magnetosphere. The fluxes of ENAs in the energy range 10 - 30 keV are very low and result in a count rate of 0.1 s^{-1}. Thus their detection is rather difficult.

The paper is the first ever addressing the problem of ENA generation and ENA imaging at Mars. It presents basic ideas concerning what could be achieved by the ENA imaging technique in investigations of the solar-wind planet interaction and was initiated, basically, by the experimental requirements to estimate the ENA fluxes expected at Mars. We hope that this paper will launch much more comprehensive numerical simulations of ENA imaging at Mars, which are strongly needed both for interpretation of the Mars 96 results and for the development of instruments for future Martian missions.

References

Anderson, D. E., Mariner 6, 7, and 9 ultraviolet spectrometer: Analysis of hydrogen Lyman alpha data, *J. Geophys. Res., 79,* 1513-1518, 1974.

Anderson, D. E., and C. W. Hord, Mariner 6 and 7 ultraviolet spectrometer experiment analysis of hydrogen Lyman alpha data, *J. Geophys. Res., 76,* 6666-6673, 1971.

Afonin, V., S. McKenna-Lawlor, K. Gringauz, K. Kecskemety, E. Keppler, E. Kirsch, A. Richter, D. O'Sullivan, A. Somogyi, A. Thompson, A. Varga, and M. Witte, Energetic ions in the close environment of Mars and particle shadowing by the planet, *Nature, 341,* 616-618 1989.

Afonin, V., et al., Low energy charged particles in near Martian space from the SLED and LET experiments aboard the PHOBOS-2 spacecraft, *Planet. Space. Sci., 39,* 153-166, 1991.

Amsif A., J. Dandouras, and E. C. Roelof, Modelling the production of energetic neutral atoms in Titan's exosphere, to be submitted to *J. Geophys. Res.,* 1995.

Andersen, H. H., and J. F. Ziegler, *Hydrogen. Stopping powers and ranges in all elements,* The stopping and ranges of ions in matter , 3, Pergamon Press, 1977.

Banaszkiewicz, M., and W.-H. Ip, A statistical study of impact ejecta distribution around Phobos and Deimos, *Icarus, 90,* 237-253, 1991.

Barabash, S., E. Dubinin, N. Pissarenko, R. Lundin, and C. Russell, Picked up protons near Mars: PHOBOS observations, *Geophys. Res. Lett., 18,* 1805-1808, 1991.

Barabash, S., R. Lundin, and O. Norberg, Upstream regions at Mars, in *Plasma environments of non-magnetized planets,* edited by T. I. Gombosi, pp. 285-290, Pergamon Press, Oxford, 1993.

Barabash, S., and R. Lundin, Reflected ions near Mars: PHOBOS-2 observations, *Geophys. Res. Lett., 20,* 787-790, 1993.

Barabash, S., and R. Lundin, On a possible dust-plasma interaction at Mars, *IEEE Trans. on plasma science, 22,* 173-178, 1994.

Barabash, S., and O. Norberg, Indirect detection of the Martian helium corona, *Geophys. Res. Lett., 21,* 1547-1550, 1994.

Barabash, S., R. Lundin, T. Zarnowiecki, and S. Gredzielski, Diagnostic of energetic neutral particles at Mars by the ASPERA-C instrument for the Mars 96 mission, *Adv. Space Res., 16,* (4)81-(4)86, 1995a.

Barabash, S., E. Kallio, R. Lundin, and H. Koskinen, Measurements of nonthermal helium escape from Mars, *J. Geophys. Res., 100,* 21,307-21,316, 1995b.

Barabash, S., and Kallio E., Global dynamics of the solar wind protons at Mars as observed by the ASPERA experiment, in preparation, 1995c.

Barabash, S., P Cson Brandt, O Norberg, R. Lundin, C. J. Chase, B. H. Mauk, and E. C. Roelof, Astrid observations of the ENA emissions in the vicinity of the generation region (abstract), *Eos Trans. AGU, 76,* 488, 1995d.

Barabash, S., and S. Olsen, Functional tests of 56 mm diameter microchannel plates distributed by Science Brothers, Inc., in preparation, 1995e.

Barbosa, D., and A. Eviatar, Planetary fast neutral emission and effects on the solar wind: a cometary exospheric analog, *Astrophys. J., 310,* 927-936, 1986.

Benazeth, N., Review on kinetic ion-electron emission from solid metallic targets, *Nucl. Instr. and Meth., 194,* 405-413, 1982.

Benninghoven, A., C. Plog, and N. Treitz, Measurements of relative secondary ion yields from oxidized tungsten (100) under bombardment by ions with different masses and energies, *Int. J. of Mass Spectroscopy and Ion Phys., 13,* 415-424, 1974.

Bernstein, W., R. L. Wax, N. L. Sanders, and G. T. Inouye, An energy spectrometer for energetic (1-25 keV) neutral hydrogen atoms, in *Small Rocket Instrumentation Techniques,* 224-231, North-Holland Publ. Comp., Amsterdam, 1969.

Bleszynski, S., Measurements of secondary ion, electron and photon yields of Pb-glass and LiF surfaces upon impact of He-atoms in the energy range of 23 to 3000 eV, *Tech. Rep. MPAE-T-77-85-26,* Max-Planck-Institut für Aeronomie, Katlenburg-Lindau, Germany, 1985.

Bogdanov, A. V., Mars satellite Deimos interaction with the solar wind and its influence on flow around Mars, *J. Geophys. Res., 86,* 6926-6932, 1981.

Bonifazi, C., G. Moreno, A. J. Lazarus, and J. D. Sullivan, Deceleration of the solar wind in the Earth's foreshock region: Isee 2 and Imp 8 observations, *J. Geophys. Res., 85,* 6031-6038, 1980.

Butenko, V. D., O. R. Grigoryan, S. N. Kuznetsov, G. S. Malkiel, and V. G. Stolpovskii, Proton currents with Ep < 70 keV at low altitudes in the equatorial region, *Kosmicheskie Issledovaniya 13,* 508-512, 1975.

Brecht, S. H., and J. R. Ferrante, Global hybrid simulation of unmagnetized planets: Comparison of Venus and Mars, *J. Geophys. Res., 96,* 11,209-11,220, 1991.

Breus, T. K., A. M. Krymskii, R. Lundin, E. M. Dubinin, J. G. Luhmann, Ye. G. Yeroshenko, S. V. Barabash, V. Ya. Mitnitskii, N. F. Pissarenko, and V. A. Styashkin, The solar wind interaction with Mars: Phobos 2 mission observations of an ion composition boundary on the dayside, *J. Geophys. Res., 96,* 11,165-11,174, 1991.

Chamberlain, J. W., Planetary coronae and atmospheric evaporation, *Planet. Space Sci., 11*, 901 - 960, 1963.

Chase, C. J., B. H. Mauk, E. C. Roelof, R. A. Wolf, and R. W. Spiro, Energetic neutral atom images of H^+ and O^+ magnetospheric ion distributions simulated from Astrid 1000 km polar orbit (abstract), *Eos Trans. AGU, 75,* 546, 1995a.

Chase, C. J., E. C. Roelof, B. H. Mauk, G. Crowley, S. Barabash, O. Norberg, R. Lundin, P. Cson Brandt, Energetic neutral atom images from Astrid: Interaction of an ion injection event with the exosphere (abstract), *Eos Trans. AGU, 76,* 501, 1995b.

Cheng, A. F., Energetic neutral particles from Jupiter and Saturn, *J. Geophys. Res., 91,* 4524-4530, 1986.

Cheng, A. F., E. P. Keath, S. M. Krimigis, B. H. Mauk, R. W. McEntire, D. G. Mitchell, E. C. Roelof, and D. J. Williams, Imaging Neutral Particle Detector, *Remote Sensing Review, 8,* 101-145, 1993.

Cson Brandt, P., S. Barabash, O. Norberg, R. Lundin, C. J. Chase, B. H. Mauk, E. C. Roelof, ENA imaging of ions at low altitudes from the Swedish microsatellite Astrid during enchanced *Dst* (abstract), *Eos Trans. AGU, 76,* 501, 1995.

Dessler, A. J., and E. N. Parker, Hydromagnetic theory of geomagnetic storms, *J. Geophys. Res., 64,* 2239-2252, 1959.

Doke, T. et al., The energetic particle spectrometer HEP onboard the GEOTAIL spacecraft, *J. Geomag. Geoelectr., 46*, 713-733, 1994.

Dostovalov, S. B., and S. D. Chuvahin, Distribution of neutral hydrogen in the Martian upper atmosphere, *Cosmic. res., 11,* Engl. Transl., 767, 1973.

Dubinin, E., R. Lundin, N. Pissarenko, S. Barabash, A. Zakharov, H. Koskinen, K. Schwingenschuh, and Ye. Yeroshenko, Indirect evidences for a gas/dust torus along the Phobos orbit, *Geophys. Res. Lett., 17,* 861 - 864, 1990.

Dubinin, E. M., N. Pissarenko, S. V. Barabash, A. V. Zacharov, R. Lundin, R. Pellinen, K. Schwingenschuh, Ye. G. Yeroshenko, Plasma and magnetic field effects associated with Phobos and Deimos tori, *Planet. Space Sci., 39,* 113-121, 1991a.

Dubinin, E. M., N. Pissarenko, S. V. Barabash, A. V. Zacharov, R. Lundin, H. Koskinen, K. Schwingenschuh, Ye. G. Yeroshenko, Tails of Phobos and Deimos in the solar wind and in the Martian magnetosphere, *Planet. Space Sci., 39,* 123-130, 1991b.

Dubinin, E., R. Lundin, H. Koskinen, and O. Norberg, Cold ions at the Martian bow shock: Phobos observations, *J. Geophys. Res., 98,* 5617-5623, 1993.

Dubinin, E., D. Obod, A. Pedersen, and R. Grard, Mass-loading asymmetry in upstream region near Mars, *Geophys. Res. Lett., 21,* 2769-2772, 1994.

Fanale, F. P., and J. R. Salvail, Loss of water from Phobos, *Geophys. Res. Lett., 16,* 287-290, 1989.

Farmer, C. B., D. W. Davies, A. L. Holland, D. D. LaPorte, and P. E. Downs, Mars: Water vapour observations from the Viking orbiters, *J. Geophys. Res., 82,* 4225-4248, 1977.

Fechtig, H. E. Grün, and G. Morfill, Micrometeoroids within ten Earth radii, *Planet. Space Sci., 27,* 511-531, 1979.

Fomenkova, M. N., and D. A. Mendis, A note on the very small grains (VSGs) observed at Halley's comet, *Astrophysics and Space Science, 189*, 327-331, 1992.

Funsten, H. O., D. J. McComas, and B. L: Barraclough, Application of thin foils in low energy neutral atom detection, in *Instrumentation for Magnetospheric Imagery, Proc. SPIE Int. Soc. Opt. Eng.*, vol. 1744, 62-69, 1992.

Goldstein, B. E., S. T. Suess, R. J. Walker, Mercury: Magnetospheric processes and the atmospheric supply and loss rate, *J. Geophys. Res., 86,* 5485-5499, 1981.

Goldstein, R., D. T. Young, H. Balsiger, F. Buehler, B. E. Goldstein, M. Neugebauer, H. Rosenbauer, R. Schwenn, and E. G. Shelley, Hot ions observed by the Giotto mass spectrometer at the comet P/Halley contact surface, *Astron. Astrophys., 187,* 220-224, 1987.

Ghielmetti, A. G. E. G. Shelley, S. A. Fuselier, P. Wurz, P. Bochsler, F. A. Herrero, M. F. Smith, T. S. Stephen, Mass spectrograph for imaging low-energy neutral atoms, *Optical Engineering, 33,* 362-370, 1994.

Grard, R. J. L., Properties of the satellite photoelectron sheath derived from photoemission laboratory measurements, *J. Geophys. Res., 78,* 2885-2906, 1973.

Grard, R., C. Nairn, A. Pedersen, S. Klimov, S. Savin, and A. Skalsky, Plasma and waves around Mars, *Planet. Space Sci., 39,* 89-98, 1991.

Grahn, S., The Freja magnetospheric research satellite, design and flight, *Proc. the 9th Annual AIAA/USU Conf. on Small Satellites,* Logan, Utah, September 13-16, 1993.

Grahn, S., and A. Rathsman, ASTRID: An attempt to make the microsatellite a useful tool for space science, *Proc. the 11th Annual AIAA/USU Conf. on Small Satellites,* Logan, Utah, September, 1995.

Gruntman, M. A., A. A. Kozochkina, and V. B. Leonas, Three MCP assembly for two-dimension imaging. Design and characteristics (in Russian), Preprint 1270, Space Research Institute, Moscow, 1987 .

Gruntman, M. A., Submicron structures: promising filters in EUV: a review, *Proc. SPIE, 1549,* 385-394, 1991.

Gruntman, M., Anisotropy of the ENA flux in the helioshere, *Planet. Space Sci., 40,* 439-445, 1992.

Gruntman, M., A new collimator design for energetic neutral atom instruments, *Rev. Sci. Instrum., 65,* 758-759, 1994a.

Gruntman, M., Neutral solar wind properties: Advance warning of major geomagnetic storms, *J. Geophys. Res., 99,* 19213-19227, 1994b.

Herbert, F., Solar wind interaction with asteroids, *Adv. Space Res., 13,* (10)249-(10)258, 1993.

Hesse, M., M. F. Smith, F. Herrero, A. G. Ghielmetti, E. G. Shelley, P. Wurz, P. Bochsler, D. L. Gallagher, T. E. Moore, T. S. Stephen, Imaging ion outflow in the high-latitude magnetosphere using low-energy neutral atoms, *Optical Engineering, 32,* 3153-3160, 1993.

Holzer, T. E., Neutral hydrogen in interplanetary space, *Rev. Geophys. Space Phys., 15,* 467-490, 1977.

Honig, R. E., Analysis of surfaces and thin films by mass spectrometry, in *Advances in Mass Spectrometry,* vol. 6, edited by A. R. West, pp. 337-362, Institute of Petroleum, London, 1976.

Hovestadt, D., B. Hausler, and M. Scholer, Observation of energetic particles at very low altitudes near the geomagnetic equator, *Phys. Rev. Lett., 28,* 1340-1344, 1972.

Hovestadt, D., and M. Scholer, Radiation belt-produced energetic hydrogen in interplanetary space, *J. Geophys. Res., 81*, 5039-5042, 1976.

Horanyi, M., J. Burns, M. Tatrallyay, and J. Luhmann, Toward understanding the rate of dust lost from the Martian satellites, *Geophys. Res. Lett., 17,* 853-856, 1990.

Hsieh, K. C., and C. C. Curtis, The different approaches and their problems in the detection of energetic neutrals, *Proc. of 4th International workshop on Interaction of neutral gases with plasma in Space,* edited by M. Bzowski, J. Ziemkiewicz, T. Zarnowiecki, Warsaw, 1988a.

Hsieh, K. C., and C. C. Curtis, A model for the spatial and energy distributions of energetic neutral atoms produced within the Saturn / Titan plasma system, *Geophys. Res. Lett., 15,* 772-775, 1988b.

Hsieh, K. C., K. L. Shih, D. J. McComas, S. T. Wu, and C. C. Wu, Forecasting the arrival of fast coronal mass ejecta at Earth by detection of 2 - 20 keV neutral atoms, in *Instrumentation for Magnetospheric Imagery*, *Proc. SPIE Int. Soc. Opt. Eng.*, vol. 1744, 72-78, 1992.

Ishimoto, M., M. R. Torr, P. G. Richards, and D. G. Torr, The role of energetic O+ precipitation in a mid-latitude aurora, *J. Geophys. Res., 91,* 5793-5802, 1986.

Ishimoto, M., and M. R. Torr, Energetic He^+ precipitation in a mid-latitude aurora, *J. Geophys. Res., 92,* 3284-3292, 1987.

Ishimoto, M., G. J. Romick, and C.-I. Meng, Energy distribution of energetic O^+ precipitation into the atmosphere, *J. Geophys. Res., 97,* 8619-8629, 1992a.

Ishimoto, M., G. J. Romick, and C.-I. Meng, Model calculation of the N_2^+ first negative intensity and vibrational enhancement from energetic incident O^+ energy spectra, *J. Geophys. Res., 97,* 8653-8660, 1992b.

Ip, W.-H., On the oxygen corona of Mars, *Icarus, 76,* 135-145, 1988a.

Ip, W.-H., Source mechanisms of magnetospheric suprathermal and energetic neutrals, *Proc. of 4th International workshop on Interaction of neutral gases with plasma in Space,* edited by M. Bzowski, J. Ziemkiewicz, T. Zarnowiecki, Warsaw, 1988b.

Ip, W.-H, The fast atomic oxygen corona extent of Mars, *Geophys. Res. Lett., 17,* 2289-2292, 1990.

Ip, W.-H. and M. Banaszkiewicz, On the dust/gas tori of Phobos and Deimos, *Geophys. Res. Lett., 17,* 857 - 860, 1990.

Ip, W.-H., Neutral particle environment of Mars: the exosphere-plasma interaction effects, *Adv. Space Res., 12,* (9)295-(9)211, 1992.

Ip, W-H., T. K. Breus, and T. Zarnowiecki, Termination of the solar wind proton flow due to charge exchange effect near Mars, in *Plasma environments of non-magnetized planets,* edited by T. I. Gombosi, pp. 291-294, Pergamon Press, Oxford, 1993.

Johansen, G. A., Development and analysis of silicon based detectors for low energy nuclear radiation, Ph. D. Thesis, University of Bergen, Bergen, Norway, November, 1990.

Juhasz, A., M. Tatrallyay, G. Gevai, and M. Horanyi, On the density of the dust halo around Mars, *J. Geophys. Res., 98,* 1205-1211, 1993.

Juhasz, A., and M. Horanyi, Dust torus around Mars, *J. Geophys. Res., 100,* 3277-3284, 1995.

Kiraly, P., R. Loch, K. Szegö, I. Szemerey, I. Szucs, M. Tatrallyay, N. Shutte, A. Dyachkov, K. Gringauz, S. Sheronova, M. Verigin, T. Cravens, T. Gombosi, A. Nagy, and W. Sharp, The HARP plasma experiment on board the PHOBOS-2 spacecraft: Preliminary results, *Planet. Space Sci., 39,* 139-145, 1991.

Krebs, K. H., Recent advances in the field of ion-induced kinetic electron emission from solids, *Vacuum, 33,* 555-563, 1983.

Kirsch, E., S. M. Krimigis, J. W. Kohl, E. P. Keath, Upper limits for X-ray and energetic neutral particle emission from Jupiter: Voyager-1 results, *Geophys. Res. Lett., 8,* 169-172, 1981a.

Kirsch, E., S. M. Krimigis, W. H. Ip, and G. Gloeckler, X-ray and energetic neutral particle emission from Saturn's magnetosphere, *Nature, 292,* 718-721, 1981b.

Krasnopolsky, V. A., S. Bowyer, S. Chakrabarti, G. R. Gladstone, and J. S. McDonald, First measurement of helium on Mars: Implications for the problem of radiogenic gases on the terrestrial planets, *Icarus, 109,* 337-351, 1994.

Krimigis, S. M., J. W. Kohl, and T. P. Armstrong, The magnetospheric contribution to the quiet-tome low energy nucleon spectrum in the vicinity of the earth, *Geophys. Res. Lett., 2,* 457-460, 1975.

Krymskii, A., T. Breus, M. Dougherty, D. Southwood, and W. Axford, The electromagnetic effects of the solar wind interaction with the Phobos neutral gas halo and dust torus, *Planet. Space Sci., 40,* 1033-1041, 1992.

Luhmann J. G. , A model of the ion wake of Mars, *Geoph. Res. Lett., 17,* 869-872, 1990.

Luhmann J. G. , and K. Schwingenschuh, A model of the energetic ion environment of Mars, *J. Geoph. Res., 95,* 939-945, 1990.

Luhmann, J. G., and J. U. Kozyra, Dayside pickup oxygen ion precipitation at Venus and Mars: spatial distributions, energy deposition and consequences, *J. Geophys. Res., 96,* 5457-5467, 1991.

Luhmann, J. G., R. E. Johnson, M. H. G. Zhang, Evolutionary impact of sputtering of the Martian atmosphere by O^+ pickup ions, *Geophys. Res. Lett., 19,* 2151-2154, 1992.

Lundin, R., A. Zakharov, R. Pellinen, H. Borg, B. Hultqvist, N. Pissarenko, E. M. Dubinin, S. W. Barabash, I. Liede, and H. Koskinen, First measurements of the ionospheric plasma escape from Mars, *Nature, 341*, 609-612, 1989a.

Lundin, R., B. Hultqvist, S. Olsen, A. Zakharov, N. Pissarenko, E. Dubinin, R. Pellinen, and I. Liede, The ASPERA experiment on the Soviet PHOBOS spacecraft, in *Solar System Plasma Physics, Geophys. Monogr. Ser.*, vol. 54, edited by J. H. Waite Jr., J. L. Burch, and T. E. Moore, pp. 417-424, AGU, Washington, D. C., 1989b.

Lundin, R., A. Zakharov, R. Pellinen, H. Borg, B. Hultqvist, N. Pissarenko, E. M. Dubinin, S. V. Barabash, I. Liede, and H. Koskinen, Plasma composition measurements of the Martian magnetosphere morphology, *Geophys. Res. Lett., 17,* 877-880, 1990.

Lundin, R., E. Dubinin, S. Barabash, and O. Norberg, ASPERA observations of Martian magnetospheric boundaries, in *Plasma environments of non-magnetized planets* , edited by T. I. Gombosi, pp. 311-320, Pergamon Press, Oxford, 1993.

Meier, R. R., and C. S. Weller, Observations of equatorial EUV bands: evidence for low-altitude precipitation of ring current helium, *J. Geophys. Res., 80,* 2813-2818, 1975.

Meinel, A. B., Doppler-shifted auroral hydrogen emission, *Astrophys. J., 113,* 50-54, 1951

McComas, D. J., H. O. Funsten, J. T. Gosling, K. R. Moore, and M. F. Thomsen, Low energy atom imaging, in *Instrumentation for Magnetospheric Imagery, Proc. SPIE Int. Soc. Opt. Eng.*, vol. 1744, 41-50, 1992.

McComas, D. J., H. O. Funsten, K. R. Moore, Detection of cold gas releases in space via low energetic neutral imaging, in *Surveillance Technologies and Imaging Components, Proc. SPIE Int. Soc. Opt. Eng.*, vol. 1952, 192-202, 1993.

McComas, D. J., H. O. Funsten, J. T. Gosling, K. R. Moore, E. E. Scime, M. F. Thomsen, Fundamentals of low-energy neutral atom imaging, *Optical Engineering, 33,* 335-341, 1994.

McEntire, R. W., and D. G. Mitchell, Instrumentation for global magnetospheric imaging via energetic neutral atoms, in *Solar System plasma physics, Geophys. Monogr. Ser.*, vol. 54, edited by J. H. Waite Jr., J. L. Burch, and T. E. Moore, pp. 69-80, AGU, Washington, D. C., 1989.

McKenna-Lawlor, S. M. P., V. Afonin, Ye. Yeroshenko, E. Keppler, E. Kirsch, and K. Schwingenschuh, First identification in energetic particles of characteristic plasma boundaries at Mars and account of various energetic particle populations close to the planet, *Planet. Space. Sci., 41,* 373-380, 1993.

Miah, M. A., K. Nagata, T. Kohno, H. Murakami, A. Nakamoto, N. Hasebe, J. Kikuchi, and T. Doke, Spatial and temporal features of 0.64-35 MeV protons in the space station environment: EXOS-C observations, *J. Geomag. Geolectr. 44,* 591-610, 1992.

Mitchell, D. G., A. F. Cheng, S. M. Krimigis, E. P. Keath, S. E. Jaskulek, B. H. Mauk, R. W. McEntire, E. C. Roelof, D. J. Williams, K. C. Hsieh, V. A. Drake, INCA: the ion neutral camera for energetic atom imaging of the Saturnian magnetosphere, *Optical Engineering, 32,* 3096-3101, 1993.

Mizera, P. F., and J. B. Blake, Observations of ring current protons at low altitudes, *J. Geophys. Res., 78,* 1058-1062, 1973.

Moore, J. H., and C. B. Opal, A slotted disk velocity selector for the detection of energetic atoms above the atmosphere, *Space Sci. Instrum, 1,* 377-386, 1975.

Moore, K. R., D. J. McComas, H. O. Funsten, M. F. Thomsen, Low energy neutral atoms in the Earth's magnetosphere: modelling, in *Instrumentation for Magnetospheric Imagery, Proc. SPIE Int. Soc. Opt. Eng.*, vol. 1744, 51-61, 1992.

Moore, K. R., H. O. Funsten, D. J. McComas, E. E. Scime, M. F. Thomsen, Terrestrial Magnetospheric imaging: Numerical modelling of low energy neutral atoms, in *Instrumentation for Magnetospheric imagery II, Proc. SPIE Int. Soc. Opt. Eng.*, vol. 2008, 190-201, 1993.

Moore, K. R., E. E. Scime, H. O. Funsten, D. J. McComas, M. F. Thomsen, Low-energy neutral atom emission from the Earth magnetosphere, *Optical Engineering, 33,* 342-348, 1994.

Moritz, J., Energetic protons at low altitudes: a newly discovered radiation belt phenomenon and its explanation, *Z. Geophys. 38,* 701, 1972.

Moroz, V. I., V. V. Kerzhanovich, and V. A. Krasnopolsky, An engineering model of the atmosphere of Mars for the Mars-94 project , *Cosmic Res.*, Engl. Transl., *29,* 1-79, 1991.

Moses, S. L., F. V. Coroniti and F. L. Scarf, Expectations for the microphysics of the Mars-solar wind interaction, *Geophys. Res. Lett., 15,* 429-432, 1988

Motschmann, K. Sauer, and T. Roatsch, Simulation of ion acceleration in a charged dust cloud, *Geophys. Res. Lett., 19,* 225-228, 1992.

Neugebauer, M., B. E. Goldstein, H. Balsiger, F. M. Neubauer, R. Schwenn, and E. G. Shelley, The density of cometary protons upstream of comet Halley's bow shock, *J. Geophys. Res., 94,* 1261-1269, 1989.

Norberg, O., S. Barabash, and R. Lundin, Observations of molecular ions in the Martian plasma environment, in *Plasma environments of non-magnetized planets* , edited by T. I. Gombosi, pp. 299-304, Pergamon Press, Oxford, 1993.

Norberg, O., S. Barabash, I. Sandahl, R. Lundin, H. Lauche, H. Koskinen, P. C:son Brandt, E. Roelof, L. Andersson, U. Eklund, H. Borg, J. Gimholt, K. Lundin, J. Rynö, and S. Olsen, The microsatellite ASTRID, *Proceedings 12th ESA Symposium on Rocket and Balloon Programmes and Related Research*, Lillehamer, Norway, 273-277, 1995.

Orsini, S., M. Candidi, M. Maggi, K. C. Hsieh, C. C. Curtis, A. M. Hudor, S. Livi, B. Wilken, I. A. Daglis, E. Flamini, B. Negri, B. A. Tinsley, M. A. Gruntman, Proposal of an Italian experiment for the mission SAC-B. ISENA: Imaging Particle Spectrometer for Energetic Neutral Atoms, in *Instrumentation for Magnetospheric imagery, Proc. SPIE Int. Soc. Opt. Eng.*, vol. 1744, 91-101, 1992.

Orsini, S., I. A. Daglis, M. Candidi, K. C. Hsieh, S. Livi, and B. Wilken, Model calculation of energetic neutral atom precipitation at low altitudes, *J. Geophys. Res., 99,* 13,489-13,498, 1994.

Perez-de-Tejada, H., Solar wind erosion of the Mars early atmosphere, *J. Geophys. Res., 97,* 3159-3167, 1992.

Rairden, R. L., L. A. Frank, and J. D. Craven, Geocoronal imaging with Dynamics Explorer, *J. Geophys. Res., 91,* 13,613-13,630, 1986.

Riedler, W. D. et al., Magnetic field near Mars: First results of the PHOBOS mission, *Nature, 341,* 604-607, 1989.

Roelof, E. C., D. G. Mitchell, and D. J. Williams, Energetic neutral atoms (E ~ 50 keV) from the ring current: IMP 7/8 and ISEE 1, *J. Geophys. Res., 90,* 10,991-11,008, 1985.

Roelof, E. C., Energetic neutral atom image of a storm-time ring current, *Geophys. Res. Lett., 14,* 652-655, 1987.

Roelof, E. C., Remote sensing of the ring current using energetic neutral atoms, *Adv. Space Res., 9,* (12)195-(12)203, 1989.

Roelof, E. C., Imaging heliospheric shocks using energetic neutral atoms, In *Solar Wind Seven,* edited by E. Marsch and R. Schwenn, *Proc. 3rd COSPAR Colloquium*, Pergamon Press, Oxford, 385 - 390, 1992a.

Roelof, E. C., B. H. Mauk, R. R. Meier, Instrument requirements for imaging the magnetosphere in the EUV and ENA derived from computer - simulated images, in *Instrumentation for Magnetospheric Imagery, Proc. SPIE Int. Soc. Opt. Eng.*, vol. 1744, 19-30, 1992b.

Roelof, E. C., B. H. Mauk, R. R. Meier, K. R. Moore, R. A. Wolf, Simulations of EUV and ENA Magnetospheric images based on the Rice Convection Model, in *Instrumentation for Magnetospheric Imagery II, Proc. SPIE Int. Soc. Opt. Eng.*, vol. 2008, 202-213, 1993.

Roelof, E. C., ENA production from low altitudes, in preparation, 1995.

Rosenbauer, H., N. Shutte, I. Apathy, A. Galeev, K. Gringauz, H. Grünwaldt, P. Hemmerich, K. Jockers, P. Kiraly, G. Kotova, S. Livi, E. Marsch, A. Richter, W. Riedler, T. Remizov, R. Schwenn, K. Schwingenschuh, M. Steller, K. Szegö, M. Verigin, and M. Witte, Ions of Martian origin and plasma sheet in the Martian magnetosphere: initial results of the TAUS experiment, *Nature, 341,* 612-614, 1989.

Russell, C. T., T. I. Gombosi, M. Horanyi, T. E. Cravens, and A. F. Nagy, Charge-exchange in the magnetosheaths of Venus and Mars: a comparison, *Geophys. Res. Lett., 10,* 163-164, 1983.

Russell, C. T., Interplanetary magnetic field enhancements: further evidence for an association with asteroid 2201 Oljato, *Geophys. Res. Lett., 14,* 491-494, 1987.

Russell, C. T., J. G. Luhmann, K. Schwingenschuh, W. Riedler, Ye. Yeroshenko, Upstream waves at Mars: Phobos observation, *Geophys. Res. Lett., 17,* 897-900, 1990.

Sagdeev, R. Z., and A. V. Zakharov, Brief history of the Phobos mission, *Nature, 341*, 581-584, 1989.

Samson, J. A. R., *Techniques of vacuum ultraviolet spectroscopy*, 230 pp., John Wiley and Sons, Inc., New York, 1967.

Sauer, K., A. Bogdanov, and K. Baumgärtel, The protonopause-an ion composition boundary in the magnetosheath of comets, Venus, and Mars, *Adv. Space Res., 16,* (4)153-(4)158, 1995.

Skalsky, A., R. Grard, S. Klimov, C. M. C. Nairn, J. G. Trotignon, and K. Schwingenschuh, The Martian bow shock: wave observations in the upstream region, *J. Geophys. Res., 97,* 2927-2933, 1992.

Scarf, F. L., F. V. Coroniti, C. F. Kennel, T. R. Sanderson, K.-P. Wenzel, R. J. Hynds, E. J. Smith, S. J. Bame, and R. D. Zwickl, ICE plasma wave measurements in the ion pick-up region of comet Halley, *Geophys. Res. Lett., 13,* 857-860, 1986.

Scholer, M., D. Hovestadt, and G. Morfill, Energetic He^+ ions from the radiation belt at low altitudes near the geomagnetic equator, *J. Geophys. Res., 80,* 80-85, 1975.

Scime, E. E., H. O. Funsten, K. R. Moore, M. A. Gruntman, Novel low-energy neutral atom imaging technique, *Optical Engineering, 33,* 357-361, 1994.

Schulte, P., and F. Arnold, Detection of upper atmospheric negatively charged microclusters by a rocket-borne mass spectrometer, *Geophys. Res. Lett., 23,* 2297-2300, 1992.

Soter, S., The dust belts of Mars, Center for Radiophysics and Space Research, *CRSR 462,* Cornell University, 1971.

Svestka, J., I. Cermak, and E. Grün, Electric charging and electrostatic fragmentation of dust particles in laboratory, *Adv. in Space Res.*, in press, 1993.

Søraas, F., K. Måseide, P. Torheim, K. Aarsnes, Doppler-shifted auroral H_β emission: a comparison between observations and calculations, *Ann. Geophysicae, 12,* 1052-1064, 1994.

Søraas, F., and K. Aarsnes, ENA observations in an aurora, *Proceedings 12th ESA Symposium on Rocket and Balloon Programmes and Related Research*, Lillehamer, Norway, in press, 1995.

Tinsley, B. A., Energetic neutral atom precipitation during magnetic storm: Optical emission, ionization and energy deposition at low and middle latitudes, *J. Geophys. Res., 84,* 1855-1864, 1979.

Tinsley, B. A., Neutral atom precipitation-a review, *J. Atmos. Terr. Phys., 43,* 617-632, 1981.

Tinsley, B. A., R. P. Rohrbaugh, H. Rassoul, E. S. Barker, A. L. Cochran, W. D. Cochran, B. J. Wills, D. W. Wills, and D. Slater, Spectral characteristics of two types of low latitude aurorae, *Geophys. Res. Lett., 11,* 572-575, 1984.

Tinsley, B. A., R. P. Rohrbaugh, H. Rassoul, Y. Sahai, N. R. Teixeira, and D. Slater, Low altitude aurorae and storm ring current systems, *J. Geophys. Res., 91,* 11,257-11,269, 1986.

Tinsley, B. A., R. P. Rohrbaugh, M. Ishimoto, M. R. Torr, and D. G. Torr, Middle- and low-latitude emissions from energetic neutral atom precipitation seen from ATLAS 1 under quiet magnetic conditions, *J. Geophys. Res., 99,* 19,577-19,584, 1994.

Tsurutani B. T., and E. J. Smith, Hydromagnetic waves and instabilities associated with cometary ion pickup: ICE observations, *Geophys. Res. Lett., 13,* 263-266, 1986.

U.S. Standard Atmosphere, *NOAA document NOAA-S/T 76-1562,* U.S. Government Printing Office, Washington, D.C., 1976.

Vaisberg, O. L., Mars-plasma environment, in *Physics of Solar Planetary Environments,* edited by D. J. Williams, vol. 2, pp. 854-871, AGU, Washington, D. C., 1976.

Vaisberg, O. L., J. G. Luhmann, and C. T. Russell, Plasma observations of the solar wind interaction with Mars, *J. Geophys. Res., 95,* 14,841, 1990.

Verigin, M. I., K. I. Gringauz, G. A. Kotova, N. M. Shutte, H. Rosenbauer, S. Livi, A. K. Richter, W. Riedler, K. Schwingenschuh, and K. Szegö, On the problem of the Martian atmosphere dissipation: PHOBOS 2 TAUS spectrometer results, *J. Geophys. Res.*, *96*, 19,315 - 19,320, 1991a.

Verigin, M. I., N. M. Shutte, A. A. Galeev, K. I. Gringauz, G. A. Kotova, A. P. Remizov, H. Rosenbauer, P. Hemmerich, S. Livi, A. K. Richter, I. Apathy, K. Szegö, W. Riedler, K. Schwingenschuh, M. Steller, Ye. G. Yeroshenko, Ions of planetary origin in the Martian magnetosphere (Phobos 2/ TAUS experiment), *Planet. Space Sci., 39,* 131-137, 1991b.

Voss, H. D., W. L. Imhof, J. Mobilia, E. E. Gaines, and J. B. Reagan, Energetic particles in the night-time middle and low latitude ionosphere, *Adv. Space Res., 5,* (4)175-(4)178, 1984.

Voss, H. D., J. Mobilia, H. L. Collin, and W. L. Imhof, Satellite observations and instrumentation for measuring energetic neutral atoms, *Optical Engineering, 32,* 3083-3089, 1993.

Wax, R. L., W. R. Simpson, and W. Bernstein, Large fluxes of 1-keV atomic hydrogen at 800 km, *J. Geophys. Res., 75,* 6390-6393, 1970.

Wilken, B., I. A. Daglis, S. Orsini, T. Doke, S. Livi, Possible observations of energetic neutral atoms with HEP-LD on board the Japanese spacecraft GEOTAIL (abstract), *Eos Trans. AGU, 76,* 254, 1995.

Williams, D. J., E. Keppler, T. A. Fritz, and B. Wilken, The ISEE 1 and 2 medium energy particle experiment, *IEEE Trans. Geosci. Electron., GE-16,* 3, 270, 1978.

Williams, D. J., Why we need global observations, *Magnetospheric Physics. Achievements and Prospects*, edited by B. Hultqvist and C.-G. Fälthammar, pp. 83-101, Plenum Press, New York, 1990.

Williams, D. J., E. C. Roelof, and D. G. Mitchell, Global magnetospheric imaging, *Rev. Geophys., 30*, 183-208, 1992.

Witte, M., H. Rosenbauer, E. Keppler, H. Fahr, P. Hemmerich, H. Lauche, A. Loidl, and R. Zwickl, The interstellar neutral-gas experiment on ULYSSES, *Astron. Astrophys. Ser. 92,* 333-348, 1992.

Witte M., H. Rosenbauer, M. Banaszkiewicz, and H. Fahr, The ULYSSES neutral gas experiment: determination of the velocity and temperature of the interstellar neutral helium, *Adv. Space Res., 13*, (6)121-(6)130, 1993.

Wu, C. S., and R. C. Davidson, Electromagnetic instabilities produced by neutral particle ionization in interplanetary space, *J. Geophys. Res., 77,* 5399-5406, 1972.

Zhang, M. H. G., J. G. Luhmann, S. W. Bougher, and A. F. Nagy, The ancient oxygen exosphere of Mars: implications for atmospheric evolution, *J. Geophys. Res., 98,* 10,915-10,923, 1993.

Glossary of Acronyms

CCEM	ceramic channel electron multiplier
CE	charge exchange
CEM	channel electron multiplier
CFA	cross field analyser
CME	coronal mass ejecta
DPU	data processing unit
ENA	energetic neutral atom
HENA	high energy neutral atom
LENA	low energy neutral atom
MCP	microchannel plate
MHD	magneto hydrodynamics
MLI	multilayer insulation
PHD	pulse height distribution
SSD	solid state detector
TOF	time of flight

Acknowledgements

Any physically meaningful result in modern experimental physics is the fruit of the hard labours of many - physicists, engineers, programmers. This is particularly true for space physics. Many contribute to materialize the first ideas into hardware, to make from the hardware *an instrument*, to propel the instrument away from the Earth, to support then a weak beating thread of radio contact and, finally, to translate billions and billions of zeros and ones to nice graphs, images, and figures. I wish to thank all who were in the Phobos and Astrid projects along this way and indirectly contributed to this work.

A thesis is a personal work marking a stage in moulding a scientist. From a student to a doctor is the way of learning and a supervisor is a key person in this process. Rickard Lundin was my supervisor and my first personal thanks go to him. I appreciate very much his support in science and in life but most of all the lesson "Not to be afraid of "crazy" ideas, it may evolve into great stuff!". Those short suitable moments when he passed the calibration lab to catch the Kiruna - Umeå flight turned out sometimes into inspiring scientific discussions and I will remember them for long. ENA astronomy, antimatter meters, planetary tori, "crazy" instrumentation and many, many more were discussed. He caught the plane but I was left thinking. But thinking causes learning!

In experimental physics an idea is just a first simplest step. The next one is to put something in vacuum and with that we immediately come to the problem of searching for leaks. Searching for a leak means ethered cotton. This first lesson of practical "physics" and many others, small, but still vitally important in the experimental business, I have learnt from Sven Olsen. My grateful thanks to him.

An essential part of scientific education is mixing with other people. I am very happy that I got the chance to work in the hot plasma group of IRF-Kiruna. Practical help from Ingrid Sandahl, Lars Eliasson, and, in particular, Olle Norberg was of great importance for me and for this work. The arrival of Pontus C:son Brandt to our group was great luck for me. By answering his questions I learnt as much as him! My special thanks to the members of the "spaghetti" club Yamauchi Masatochi, Thomas Leyser, and our guests. We have had real fun talking about highly scientific matters like fractal dimension of beer foam or the plasma physics approach to the reindeer population problem.

The electronic lab headed by Kjell Lundin succeeded with the almost impossible and the PIPPI imager was delivered in time. Enthusiastic, skilful and highly professional work by Joakim Gimholt, Walter Puccio, Jonas Olsen, Herman Andersson, and Hans Borg are gratefully acknowledged.

I also want to thank my colleagues to the East and to the West. Mira Pissarenko and Edik Dubinin at the Space Research Institute, Moscow, helped me a lot at the beginning of my career in space plasma physics. Fruitful and very pleasant personal collaboration with Esa Kallio, Finnish Meteorological Institute, Helsinki, meant very much for me and for the Phobos project. I am extremely happy in having had the opportunity to work with one of the founders of ENA imaging, Edmond C. Roelof, Applied Physics Laboratory, Laurel. His extraordinary high professional level and thoroughness in data analysis help keep me within the frame of nature's laws rather than my fantasy. An astonishing programmer, Chris Chase, Applied Physics Laboratory, Laurel, made a wonderful job in the Astrid project.

The Astrid project was initiated by the Space Science Division at the Swedish Space Corporation, Solna. To build a working satellite in 14 months is not a simple task. But that was done! An excellent job was made by the SSC staff at ESRANGE. My thanks go to all of them. The Phobos project was managed by the technical division of the Space Research Institute, Moscow. I thank all staff for the work they have made despite a tremendous amount of problems.

For the production of the dissertation itself, special thanks to Birgitta Määttä and Torbjörn Lövgren and the administrative staff at IRF.

I would also like to thank the Swedish National Space Board for financial support.

What would a man be without a woman? Who is behind it all? Who is listening, supporting, encouraging? Who is patient and persistent? - thanks to my wife Victoria cannot be expressed by words. To my mother, I apologise for being so far away and for so long. I know how loneliness hurts and how much you sacrificed. How can I repay you?